An Annual Cycle of Atmosphere-Ice-Ocean Interactions using Autonomous Gliders and Moorings

N00014-16-1-2377

Craig M. Lee, Luc Rainville and Jason Gobat
Applied Physics Laboratory, University of Washington
craig@apl.washington.edu

Major Goals

SODA is a major autonomous investigation of the processes that govern upper ocean evolution in the Beaufort Sea, with a particular emphasis on understanding the transfer of atmospheric forcing into the ocean interior and how differences in ice cover impact this communication. Focus areas include:

1. How do differences in sea ice properties, including strength, mobility, open water fraction and bottom roughness, impact the transfer of momentum from atmosphere to ocean?
2. How are buoyancy inputs from processes such as net surface warming/cooling, brine rejection and sea ice melt distributed in the upper ocean, and what role do they play in governing stratification and modulating momentum input?
3. How do the horizontal and vertical scales of oceanic stratification impact the fate of momentum in the upper ocean? How does the air/ice–ocean stress (including Arctic storms) contribute to deepening of the mixed layer, erosion of upper ocean halocline, and generation of internal waves?
4. Can an understanding of these processes be used to model ice-ocean drag over a broad range of spatial and temporal variability?

Our program focused on building an Eulerian system of moorings and gliders, sited in the basin interior where sea ice undergoes large seasonal transitions, that will sample through an entire annual cycle to capture the desired range of ice conditions and atmospheric forcing. The array is designed to quantify the interactions between atmospheric forcing, sea ice properties and upper ocean structure to address questions that include:

- What processes set the vertical and horizontal structure of upper ocean stratification, and how do these evolve with changing ice conditions?
- How do horizontal structures of density and velocity vary on scales from roughly 1 to 400 km over the seasonal cycle?
- How do atmospheric forcing, diverse ice conditions and existing vertical and lateral stratification interact to govern mixed layer deepening (entrainment) and shoaling (restratification).

REPORT DOCUMENTATION PAGE

Form Approved
OMB No. 0704-0188

1. REPORT DATE *(DD-MM-YYYY)* 31-08-2021	**2. REPORT TYPE** Final Technical	**3. DATES COVERED** *(From - To)* 4/1/2016 - 3/31/2021

4. TITLE AND SUBTITLE
An Annual Cycle of Atmosphere-Ice-Ocean Interactions Using Autonomous Gliders and Moorings

5a. CONTRACT NUMBER

5b. GRANT NUMBER
N00014-16-1-2377

5c. PROGRAM ELEMENT NUMBER

6. AUTHOR(S)
Craig Lee, Luc Rainville and Jason Gobat

5d. PROJECT NUMBER

5e. TASK NUMBER

5f. WORK UNIT NUMBER

7. PERFORMING ORGANIZATION NAME(S) AND ADDRESS(ES)
University of Washington – Applied Physics Laboratory
4333 Brooklyn Avenue NE
Seattle, WA 98105-6613

8. PERFORMING ORGANIZATION REPORT NUMBER

9. SPONSORING / MONITORING AGENCY NAME(S) AND ADDRESS(ES)
Office of Naval Research / 322
875 North Randolph Street
Arlington, VA 22203-1995

10. SPONSOR/MONITOR'S ACRONYM(S)
ONR

11. SPONSOR/MONITOR'S REPORT NUMBER(S)

12. DISTRIBUTION / AVAILABILITY STATEMENT:

Distribution Statement A: Approved for public release; distribution is unlimited.

13. SUPPLEMENTARY NOTES

14. ABSTRACT
The 'Stratified Ocean Dynamics of the Arctic' Departmental Research Initiative (SODA DRI), funded by the Office of Naval Research (ONR), was motivated by the need to understand how the changing Arctic sea ice environment impacts ocean stratification and circulation, sea ice evolution, and the marine acoustic environment. SODA is a highly collaborative project involving over 25 principal investigators from more than a dozen institutions (Lee et al., 2016, 2017). The program's science objectives aim to quantify and understand the processes affecting buoyancy, momentum, and heat within the upper-ocean. To do this, the team utilized a series of autonomous instruments to measure key atmospheric, oceanographic and sea ice parameters over an annual cycle. Together, this coordinated array of instrumentation aims to elucidate the impact of changing sea ice properties on momentum and heat transfer from the atmosphere to the upper-ocean.

15. SUBJECT TERMS
Beaufort Sea, atmospheric forcing, sea ice properties, ocean stratification, Eulerian system, moorings, gliders, mix layer cha1racteristics, upper ocean structure, stratification, velocity, wave characteristics.

16. SECURITY CLASSIFICATION OF: a. REPORT	b. ABSTRACT	c. THIS PAGE	**17. LIMITATION OF ABSTRACT**	**18. NUMBER OF PAGES**	**19a. NAME OF RESPONSIBLE PERSON**
Unclassified	Unclassified	Unclassified	UU	126	Craig Lee
					19b. TELEPHONE NUMBER *(include area code)* (206) 543-1300

Standard Form 298 (Rev. 8-98)
Prescribed by ANSI Std. Z39.18

- What combinations of atmospheric forcing, ice properties and mixed layer characteristics allow efficient internal wave generation and propagation?
- What mix of ice properties, upper ocean structure (stratification and velocity) and wave characteristics result in efficient under-ice dissipation of upward propagating internal waves?

Accomplished

Science Plan

The SODA Science plan was written and published as an APL-UW Technical Report. This document articulates SODA science objectives and describes the overarching observational approach. The science plan can be found at: http://www.apl.washington.edu/research/downloads/publications/tr_1601.pdf

SODA Deployment Cruise

SODA moorings, gliders and ice-based assets were deployed from USCGC Healy (Healy 1802). Operations staged out of Dutch Harbor, Alaska, with Healy departing on 14 September and returning 18 October, 2018. Participants included SODA team members from the Applied Physics Laboratory, University of Washington, Naval Postgraduate School, British Antarctic Survey, Woods Hole Oceanographic Institution, Northeastern University, Jet Propulsion Laboratory, Applied Physics Laboratory, Johns Hopkins University and the National Ice Center, with Lee serving as chief scientist. Operations focused on the central Beaufort Sea, ranging to nearly 81°N in search of large floes of multi-year ice to support deployment of ice-based instrument clusters (Fig. 2).

Over the 34-day span, the SODA team successfully deployed:

- Three science moorings, each heavily instrumented for sampling both upper ocean and sea ice (Fig. 3). Each mooring also carried an acoustic navigation source.
- Four acoustic navigation moorings, which, when combined with the science moorings, provided geolocation capability for instruments operating beneath sea ice.
- Three clusters of ice-based instruments, each installed as part of a two-day ice station involving intensive operations on the sea ice.
- Two additional ice-based sites, each with a subset of the complete instrument set.
- Three SGX and two Seagliders, intended to sample the region surrounding the moorings for the one-year span between the 2018 deployment cruise and the 2019 recovery cruise.
- One acoustic recorder mooring, deployed for Dr. Mohsen Baidey at the University of Delaware.

Additional activities included:

- High-resolution surveys of upper ocean evolution and ice formation during freeze-up, conducted using our Underway CTD operated in a novel

configuration that used Healy's crane to allow the probe to sample undisturbed water outside the ship's wake (Fig 4).
- Recovered two moorings, one for researchers at Scripps Institution of Oceanography and a second for colleagues at NOAA's Pacific Marine Environmental Laboratory.

Glider deployments
During the mooring deployment cruise, over 475 dives (950 profiles) were collected during seven Seaglider and SGX missions, including about 15 under ice. Five of these gliders remained in the Arctic after Healy departed, but unfortunately none survived the winter. In September and October 2018, gliders sampled mostly between SODA-A and SODA-B (Figs 5,6). Taken as a whole, the SODA observing array with the mooring array, the instrumented ice clusters, the floats, the gliders, and the cruises, covered a large portion of the Beaufort Sea (Figs. 6,7).

SODA Recovery cruise
The recovery of the SODA instruments took place during the SODA/AMOS/CAATEX joint cruise from USCGC Healy (Healy 1902), with Lee serving as Chief Scientist. Operations staged out of Dutch Harbor, Alaska, with Healy departing on 2 September and returning 16 October, 2019 (Fig. 7). All the SODA science and navigation moorings were recovered, and new instruments, including moorings, gliders, ice-based instruments, were deployed as part of the AMOS program.

Remote Sensing and Situational Awareness System
We continue to collaborate with the National Ice Center (NIC). NIC supports the program during the Intensive Operational Periods (summers 2018 and 2019) by providing analyzed products targeted to the regions where ship or autonomous platforms will operate. In addition, they are providing access to the raw data for all RADARSAT-2 imagery they are collecting to develop their ice edge analysis, which we are saving at APL-UW and making available to ONR investigators. NIC is also collecting additional images over the mooring array and drifting instruments throughout the year, specifically in support to SODA. In parallel, we download and archive all Sentinel-1 SAR images and passive microwave ice concentration product.

A real-time display of images is generated and made available as a kml, which is posted online with a delay of 3-6 hours and part of the situational awareness system setup at APL (Fig. 8). In addition to remote sensing, instrument locations and some model outputs are displayed in Google Earth to guide and facilitate field operations as well as provide context to the observations during the analysis phase. This tool was heavily used by PIs and collaborators.

A manuscript entitled "Improving Situational Awareness in the Arctic Ocean" describing the SODA situational awareness is currently under review at Frontiers of Marine Sciences. The manuscript focuses primarily on how to acquire, manage, transfer, and visualize Earth Observing data (mostly sea ice images) in regions with limited connectivity. We describe the communication system between the U.S.

icebreaker dedicated to conducting science, USCGC *Healy*, supporting agencies including the U.S. National Ice Center, and the scientists involved, both on shore and in the field. It emphasizes the collaborations between funding agencies, ship operators, data centers, and national ice centers in both Europe and North America. The broad partnership described in the paper is reflected by the diversity of the authors' affiliations.

Analysis

Brenner et al. (2021) employs observations collected using the SODA upward-looking NORTEK Signature doppler velocity profilers to assess ice-ocean drag across the broad range of ice conditions experienced in the year-long SODA deployment. Ice-ocean drag coefficients vary seasonally with the growth and melt of ice keels, reaching a maximum in spring and a minimum in fall. Drag parameterizations that incorporate direct measurements of keel geometry successfully capture observed variability, while those based on indirect estimates such as ice concentration do not.

Crews et al. (2021) used high-resolution measurements of the upper ocean collected by ship-based profiling and autonomous vehicles (Seagliders and Wavegliders) and one-dimensional mixed layer models to investigate the role of melt water on freeze-up in the central Beaufort Sea. Meltwater advection can dramatically alter upper ocean structure, shallowing the mixed layer and thus reducing the cooling required to bring mixed layer temperature to freezing. Meltwater advection can also drive mixed layer cooling, which the fall 2019 measurements find to be nearly as large as heat lost to the atmosphere. Comparisons of model results and observations show that sea ice forms in areas impacted by melt water advection several days prior to freeze-up in nearby areas that are uninfluenced by meltwater, pointing to the importance of characterizing small-scale, three-dimensional upper ocean structure when forecasting sea ice evolution.

Current work focuses on quantifying transfer of momentum and heat through the mixed layer and into the stratified waters below, and on capturing the generation and propagation of near-inertial waves.

Interagency Collaboration

Fostered by the Office of Science and Technology Policy of the White House (OSTP), significant effort was also invested in building interagency coordination and collaboration. Results included assignment of a dedicated ice analyst from the National Ice Center to sail with the SODA deployment cruise, dedicated support from the NIC and the National Weather service, researchers from NASA's Jet Propulsion Laboratory joining the Healy cruise to test of a new radiometer for measuring sea surface salinity, Department of Defense supported testing of Arctic RF propagation characteristics during the cruise and the loan of instruments granted to SODA by the Bureau of Ocean Energy Management. Lee briefed the OSTP director on SODA activity and results in June 2019.

Training
Nothing to report

Dissemination
Nothing to report.

Plans
Analysis is ongoing.

Honors
Nothing to report

Tech Transfer
Nothing to report

Participants
Craig Lee

Luc Rainville

Jason Gobat

Geoff Shilling

Ben Jokinen

Students
Sam Brenner started his Ph.D. in the Physical Oceanography program at UW in Sept. 2017, working primarily with Rainville and Jim Thomson. Sam initially worked on MIZ and SeaState data, and recently transitioned to work on SODA (Brenner et al., 2021).

Laura Crews started her Ph.D. in the Physical Oceanography program at UW in Sept. 2018, working primarily with Lee and Rainville. Laura is working primarily on SODA, initially focusing on data collected during the ice formation period at the end of the 2018 Healy cruise (Crews et al., 2021). Her current work is focused on internal wave propagation and water mass modifications using the SODA mooring data.

Products
Craig M. Lee, Sylvia Cole, Martin Doble, John D. Guthrie, Scott Harper, Jennifer MacKinnon, James Morison, Ruth Musgrave, Tom Peacock, Luc Rainville, Tim Stanton, John Toole, Jim Thomson, Jeremy Wilkinson, Matthew Alford, Dale Chayes, Lee Freitag, Steve Jayne, Jae-Hun Park, Harper Simmons, Oliver Sun, Dan Torres, and Lovro Valic, 2016. Stratifed Ocean Dynamics of the Arctic: Science and Experiment Plan , Technical Report APL-UW 1601. Applied Physics Laboratory, University of Washington, Seattle, September 2016, 46 pp.

Rainville, L., J. Wilkinson, M.E.J. Durley, S. Harper, J. DiLeo, M.J. Doble, A. Fleming, D. Forcucci, H. Graber, J.T. Hargrove, J. Haverlack, N. Hughes, B. Hembrough, M. Jeffries., C.M. Lee, B. Mendenall, D. McCormmick, S. Montalvo, A. Stenseth, H. Simmons, J.E. Toomey, and J. Woods, 2020. Improving Situational Awareness in the Arctic Ocean. Submitted to Frontiers of Marine Sciences.

Brenner, S., L. Rainville , J. Thomson, S. Cole, & C. Lee, 2021. Comparing observations and parameterizations of ice-ocean drag through an annual cycle across the Beaufort Sea. Journal of Geophysical Research: Oceans, 126, e2020JC016977. https://doi.org/10.1029/2020JC016977

Crews, L., C.M. Lee, L. Rainville, and J. Thomson, 2021. Meltwater Advection Hastens Autumn Freeze Up. Submitted to Journal of Geophysical Research: Oceans

Figure 1. Clockwise from upper left: (a)The SODA science team, (b) Stablemoor deployment (SODA-A top element), (c) SGX and Seagliders waiting for deployment from USCGC Healy, (d) WHOI Ice Tethered Profiler being deployed at a SODA ice station.

Cruise Track

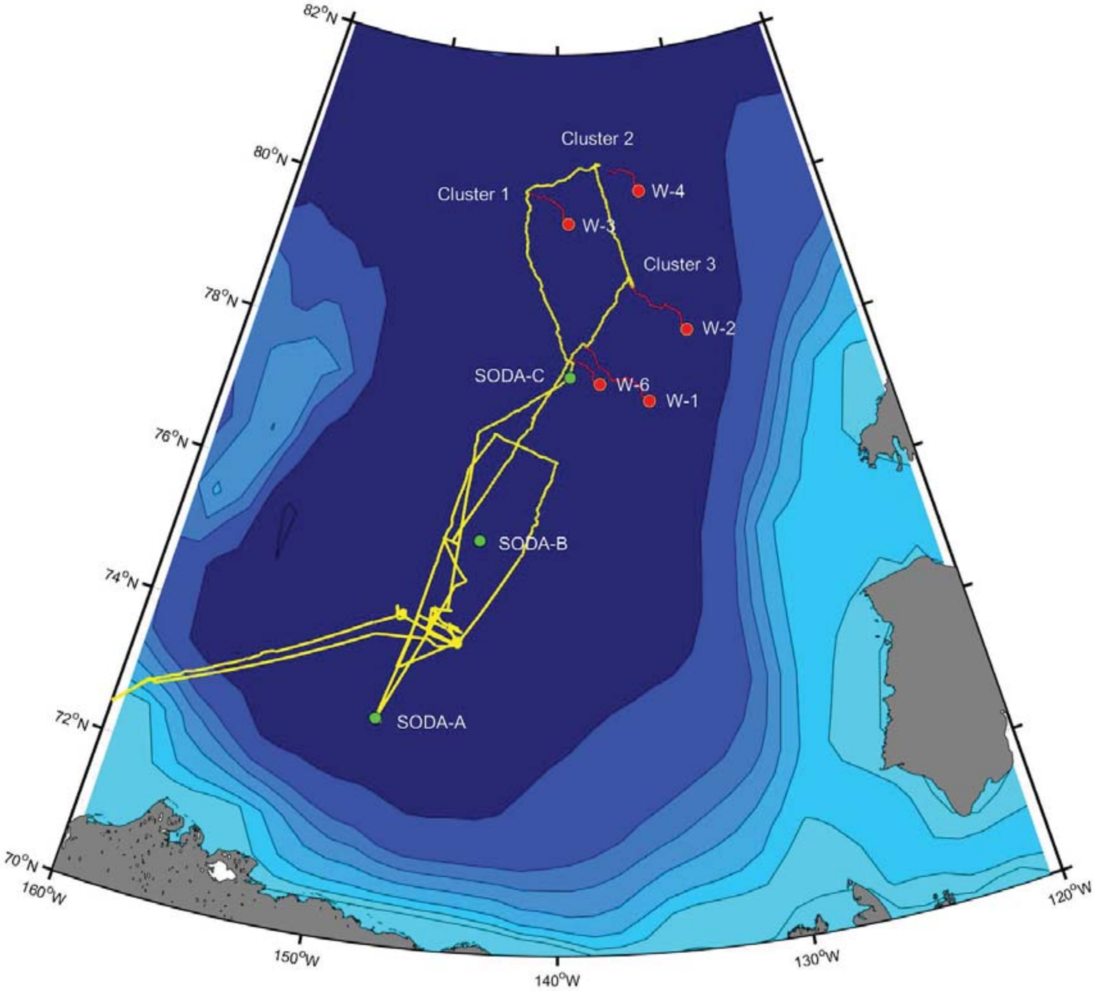

Figure 2. Cruise track for Healy 1802 (yellow line) with locations of the three science moorings (green dots) and the on-ice instrument clusters overlaid on the bathymetry (4000-3000-2000-1000-500-100-0m).

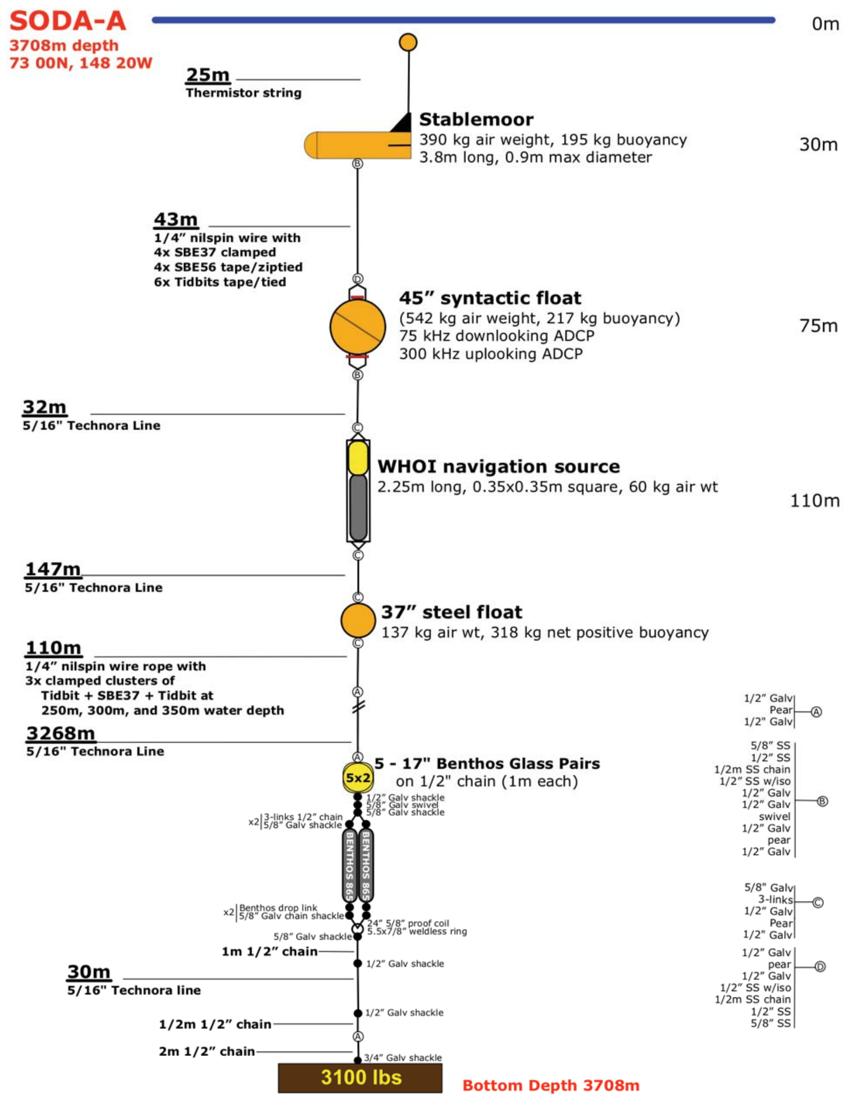

Figure 3. Schematic of the southernmost science mooring (SODA-A).

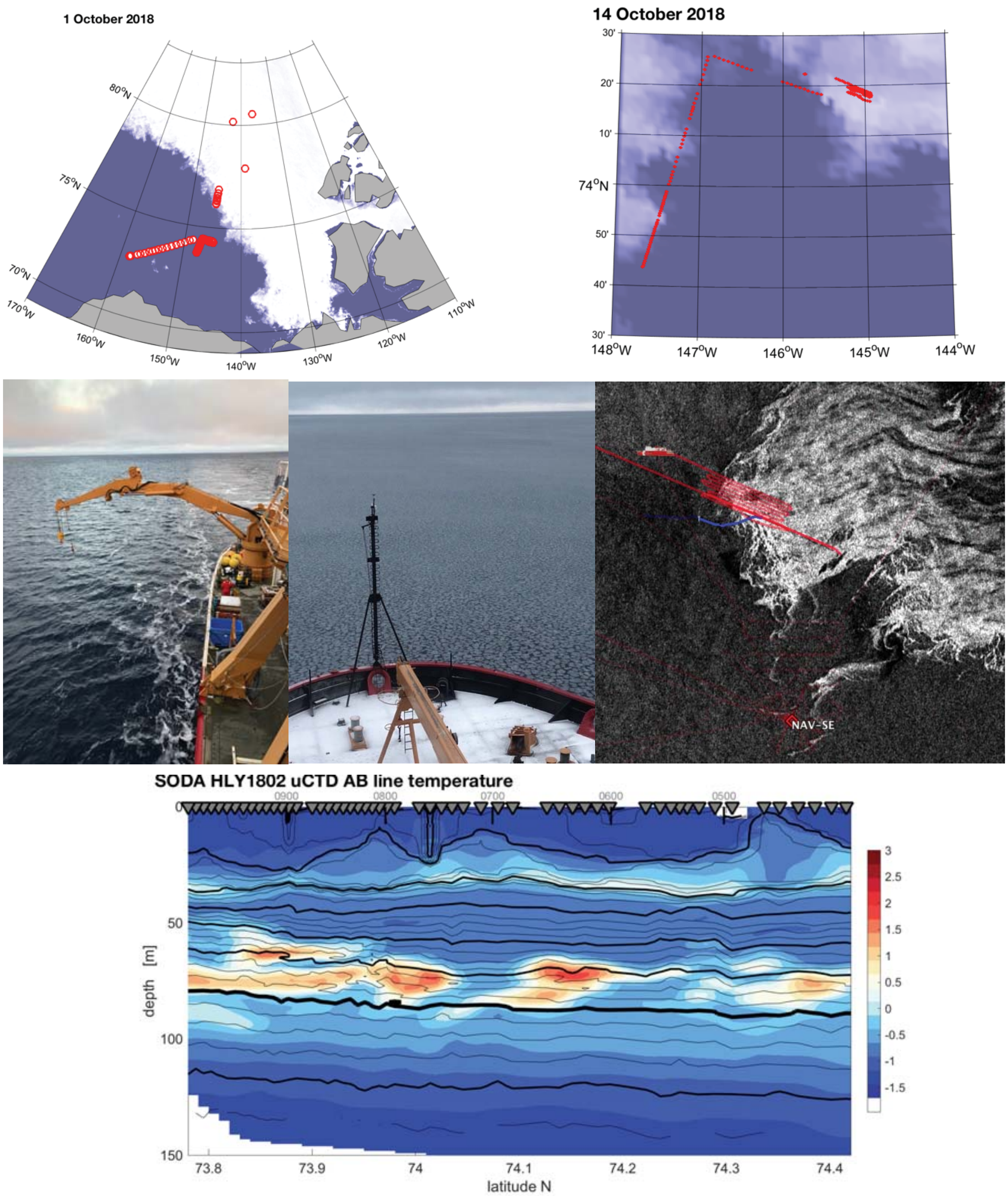

Figure 4: *Top row*: Locations of the 200 uCTD casts collected during HLY1802, overlaid on a map of sea ice concentration on 1 October 2018 (left), and close-up of the sampling location during the freeze-up period, around 14 Oct 2018 (right)

.

Middle row: Photos of the setup to sample outside the wake, and of the pancake ice conditions on 12 Oct from the ship (middle) and from remote sensing (right).
Bottom: Depth-latitude map of temperature along the last long meridional line during the freeze-up period. Gray triangles indicate the cast locations. Black contours are isohalines (intervals of 0.25 in thin, of 1 as thicker contours, and S=31 in bold).

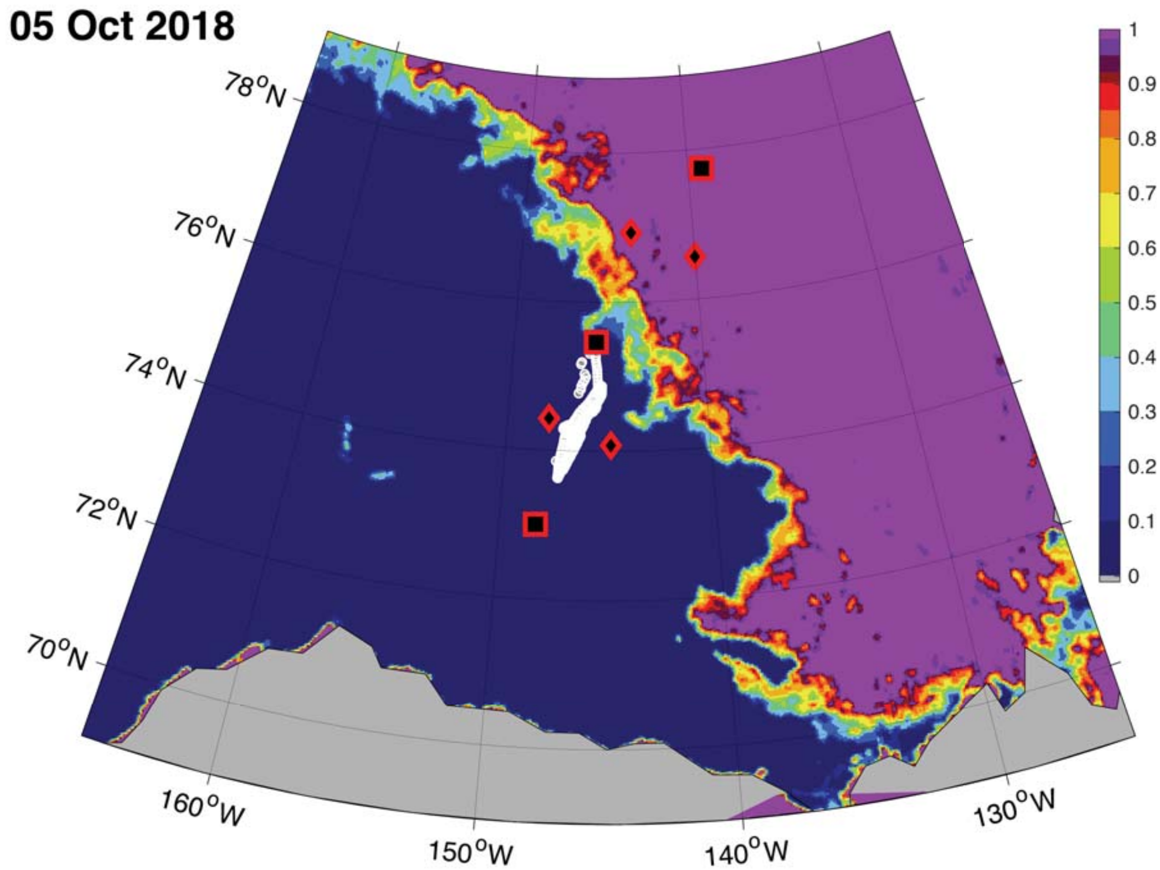

Figure 5. Map of the SODA SGX and Seaglider profile locations (white dots) during September and October 2018. Background colors are sea ice concentration on 05 Oct 2018. Red squares are SODA science moorings, and diamonds are navigation moorings.

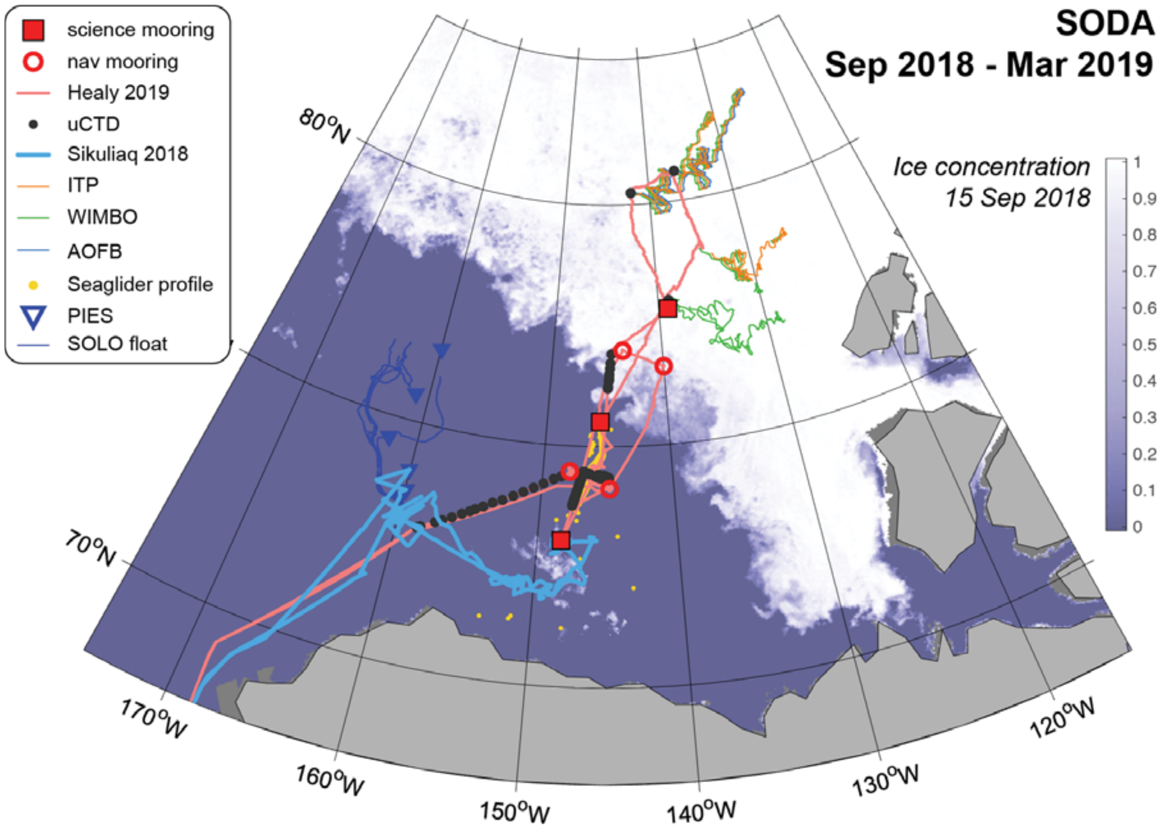

Figure 6. Map of the SODA moored array (red circles and red squares), Seaglider profile locations (yellow dots), and other SODA instruments during period from September 2018 to March 2019. Cruise track of the deployment cruise is shown. Background colors are sea ice concentration on 15 Sep 2018.

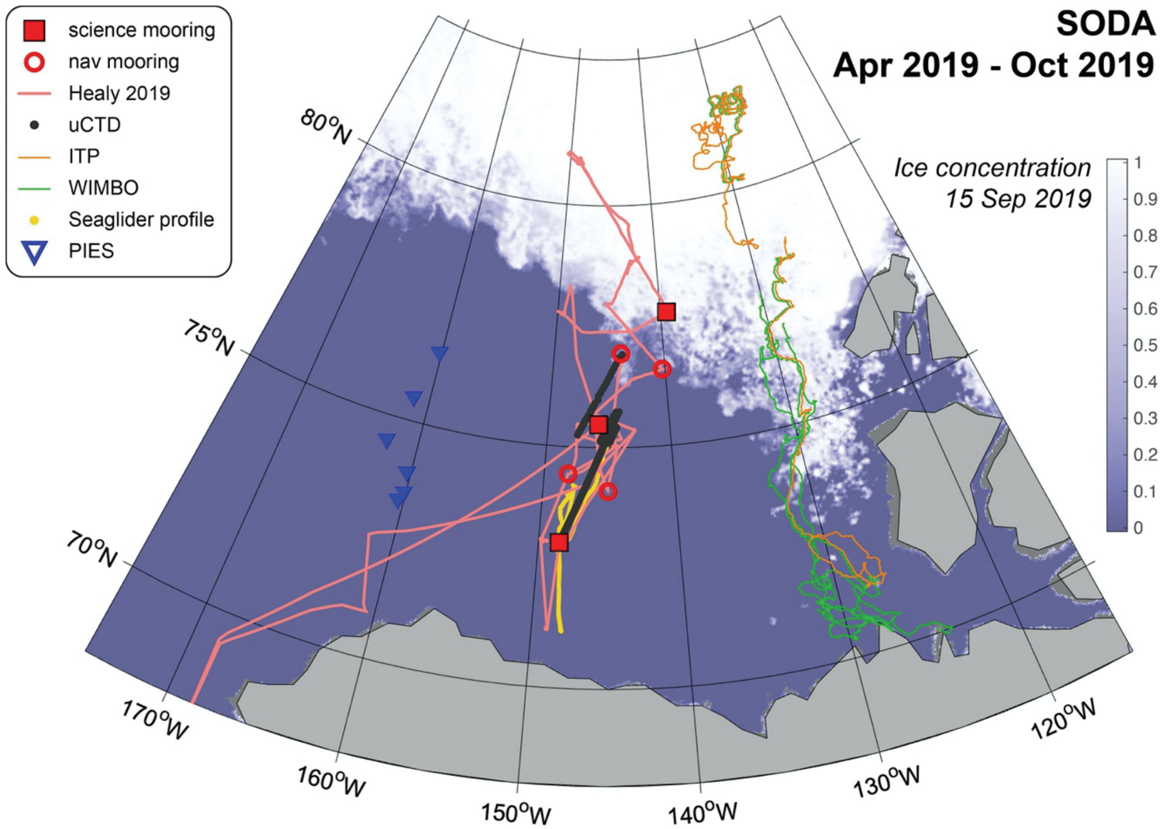

Figure 7. Map of the SODA moored array (red circles and red squares), Seaglider profile locations (yellow dots), and other SODA instruments during period from April to October 2019. Cruise track of the recovery cruise is shown. Background colors are sea ice concentration on 15 Sep 2019.

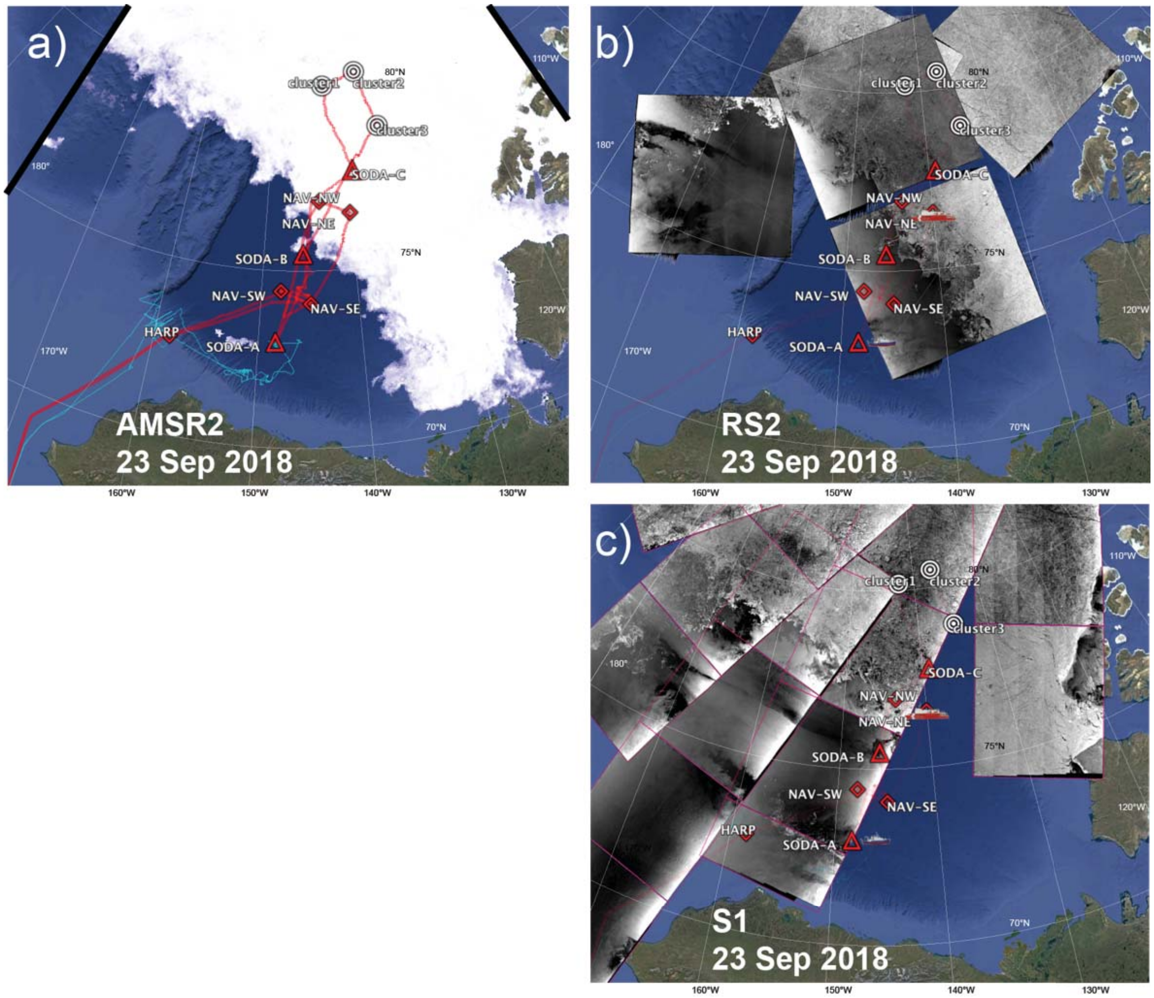

Figure 8. Example of (a) Passive Microwave [AMSR2], displayed only between 170-110°W, (b) Radarsat-2, and (c) Sentinel-1 remote sensing products on 23 Sept 2018. Healy (red) and Sikuliaq (cyan) cruise tracks are shown in (a), and the location of the ships on that day in (b,c). SODA moorings and instrument clusters are also shown.

frontiers in Marine Science

ORIGINAL RESEARCH
published: 25 November 2020
doi: 10.3389/fmars.2020.581139

Improving Situational Awareness in the Arctic Ocean

*Luc Rainville[1]**, Jeremy Wilkinson[2], Mary Ellen J. Durley[3], Scott Harper[4], Julia DiLeo[5], Martin J. Doble[6], Andrew Fleming[2], David Forcucci[3], Hans Graber[5], John T. Hargrove[5], John Haverlack[7], Nick Hughes[8], Brett Hembrough[9,10], Martin O. Jeffries[4,11], Craig M. Lee[1], Brendon Mendenhall[9], David McCormmick[12], Sofia Montalvo[12], Adam Stenseth[3], Geoffrey B. Shilling[1], Harper L. Simmons[7], James E. Toomey IV[3] and John Woods[4,12]*

[1] Applied Physics Laboratory, University of Washington, Seattle, WA, United States, [2] British Antarctic Survey, Cambridge, United Kingdom, [3] United States Coast Guard (USCGC Healy, WAGB (20)), Seattle, WA, United States, [4] Office of Naval Research, Arlington, VA, United States, [5] Center for Southeastern Tropical Advanced Remote Sensing, University of Miami, Miami, FL, United States, [6] Polar Scientific Inc., Appin, United Kingdom, [7] College of Fisheries and Ocean Sciences, University of Alaska, Fairbanks, AK, United States, [8] Norwegian Meteorological Institute, Tromsø, Norway, [9] Scripps Institution of Oceanography, University of California, San Diego, La Jolla, CA, United States, [10] Marine Operations, Oregon State University, Corvallis, OR, United States, [11] Cold Regions Research and Engineering Laboratory, Hanover, NH, United States, [12] United States National Ice Center, Suitland, MD, United States

Edited by:
Gilles Reverdin, Centre National de la Recherche Scientifique (CNRS), France

Reviewed by:
Benjamin Rabe, Alfred Wegener Institute, Helmholtz Centre for Polar and Marine Research (AWI), Germany
Brian Ward, National University of Ireland Galway, Ireland
Sabrina Speich, École Normale Supérieure, France

***Correspondence:**
Luc Rainville
lucrain@uw.edu

Specialty section:
This article was submitted to Ocean Observation, a section of the journal Frontiers in Marine Science

Received: *07 July 2020*
Accepted: *04 November 2020*
Published: *25 November 2020*

Citation:
Rainville L, Wilkinson J, Durley MEJ, Harper S, DiLeo J, Doble MJ, Fleming A, Forcucci D, Graber H, Hargrove JT, Haverlack J, Hughes N, Hembrough B, Jeffries MO, Lee CM, Mendenhall B, McCormmick D, Montalvo S, Stenseth A, Shilling GB, Simmons HL, Toomey JE IV and Woods J (2020) Improving Situational Awareness in the Arctic Ocean. Front. Mar. Sci. 7:581139. doi: 10.3389/fmars.2020.581139

To successfully operate in a harsh environment like the Arctic Ocean, one must be able to understand and predict how that environment will evolve over different spatial and temporal scales. This is particularly challenging given the on-going and significant environmental changes that are occurring in the region. Access to the most recent environmental information provides timely knowledge that enables ship-based operations to proceed efficiently, effectively and safely in this difficult arena. Knowledge of the evolving environmental conditions during a field campaign is critical for effective planning, optimal execution of sampling strategies, and to provide a broader context to data collected at specific times and places. We describe the collaborations and processes that enabled an operational system to be developed to provide a remote field-team, located on USCGC Healy in the Beaufort Sea, with near real-time situational awareness information regarding the weather, sea ice conditions, and oceanographic processes. The developed system included the punctual throughput of near real-time products such as satellite imagery, meteorological forecasts, ice charts, model outputs, and up to date locations of key sea ice and ocean-based assets. Science and operational users, as well as onshore personnel, used this system for real-time practical considerations such as ship navigation, and to time scientific operations to ensure the appropriate sea ice and weather conditions prevailed. By presenting the outputs of the system within the context of case studies our results clearly demonstrate the benefits that improved situational awareness brings to ship-based operations in the Arctic Ocean, both today and in the future.

Keywords: situational awareness, Arctic, SAR, navigation, communication, visualization

INTRODUCTION

Motivations

Our ability to understand the environment around us is very much linked to our ability to accurately predict how this environment will evolve in the future; hours, weeks, seasons, and years. However, when an environment changes beyond what is considered normal, then our predictive capability is substantially diminished. The Arctic Ocean is presently outside these boundaries. For example satellite observations over an extended period of time have clearly shown a reduction in sea ice extent in all seasons (Stroeve et al., 2012; Meier et al., 2014), changes to sea ice motion (Spreen et al., 2011), a dramatic decrease in concentration and extent of multi-year ice (Comiso, 2012), and an expansion of the marginal ice zone (Strong and Rigo, 2013; Bliss et al., 2019). These changes would not have seemed possible only a few decades ago. Understanding these changes and predicting and anticipating their effects are formidable tasks.

Over recent years, political, military, societal and commercial interest in the Arctic has increased significantly. Coinciding with this interest has been an expansion in human activity in Arctic waters, which is set to continue for the foreseeable future. At present, most sea-based operations in the Arctic are concentrated around the summer months. This summer focus is changing as operational experience is gained, infrastructure is enhanced, and the extension of the ice-free season stretches into other seasons (Wilkinson and Stroeve, 2018). Whilst the navigation of vessels through sea ice is generally considered to be more challenging, it is the plethora of environmental scenarios that could play out and the speed in which ice and weather conditions can change that increases the complexity significantly. The combination of natural variability and climate-forced changes in the Arctic marine system bring further difficulties (Wilkinson and Stroeve, 2018; Hwang et al., 2020). Given these challenges it is essential that mariners, scientists and other key personnel operating in the Arctic marine environment have access to the latest situational awareness products, such as sea ice, oceanographic and meteorological information. Arctic observational networks are growing (e.g., Lee et al., 2019; Smith et al., 2019). This information must be in a format that is simple to understand, able to be easily incorporated into the ship's navigation and operational systems, and can be transmitted in a timely fashion within the communication limitations that exist in the high Arctic.

SODA: Stratified Ocean Dynamics of the Arctic

The 'Stratified Ocean Dynamics of the Arctic' Departmental Research Initiative (SODA DRI), funded by the Office of Naval Research (ONR), was motivated by the need to understand how the changing Arctic sea ice environment impacts ocean stratification and circulation, sea ice evolution, and the marine acoustic environment. SODA is a highly collaborative project involving over 25 principal investigators from more than a dozen institutions (Lee et al., 2016, 2017).

The program's science objectives aim to quantify and understand the processes affecting buoyancy, momentum, and heat within the upper-ocean. To do this, the team utilized a series of autonomous instruments to measure key atmospheric, oceanographic and sea ice parameters over an annual cycle. Together, this coordinated array of instrumentation aims to elucidate the impact of changing sea ice properties on momentum and heat transfer from the atmosphere to the upper-ocean.

In order to achieve these aims, two separate research cruises took place in Fall 2018: (Cruise 1) a process study cruise aboard the *R/V Sikuliaq* focused on processes at the shelf break and in the southern portion of the Beaufort Gyre, and (Cruise 2) a cruise on USCGC *Healy* (hereafter *Healy*) to deploy science moorings in 3 locations (to capture ocean and ice properties), autonomous gliders that sample between and around the moorings (guided by signals from an array of navigation moorings), and several ice-based instruments that measure atmospheric, ice, and oceanic properties while drifting with the ice pack (**Figure 1**). These clusters included Ice Tethered Profilers (ITP[1]), Autonomous Ocean Flux Buoys (AOFB; Shaw et al., 2008), and Weather, Waves-Ice Mass Balance-Ocean buoy (WIMBO; Doble et al., 2017). Pressure-Inverted Echosounders (PIES) and Air Launched Autonomous Micro-Observer (ALAMO[2]) profiling floats were also deployed as part of SODA.

As the cruises were operating in both ice-covered and ice-free regions in Fall, the ice conditions were expected to be changeable and the weather tempestuous. Consequently, obtaining high-quality and near-real time knowledge of the weather, ice conditions and ocean properties was a priority for SODA field teams. Scientists aboard *R/V Sikuliaq* focused on capturing key processes at the constantly evolving ice edge, or along dynamic oceanic features, and thus needed a thorough understanding of the local environment along with the ability to constantly adapt their sampling strategy to environmental conditions and to real-time observations. The *Healy* team focused on logistical and scientific operations needed for mooring, glider and buoy deployments; thus, they required advanced knowledge of weather and ice conditions. Beyond the mooring and glider requirements, the team needed to locate thick ice floes away from the ice edge upon which to deploy their ice-based instruments. Co-locating several complementary ice-based platforms on one ice floe greatly increases the value of the collected data set relative to distributing these assets over a wider area. Even though all the on-ice assets float, it is advisable to avoid open-water deployments because instruments deployed into open water will disperse rapidly and have failure rates of $>50\%$ during freeze up, largely due to damage from rafting by newly formed ice. The requirement for co-location of assets combined with our apprehension of not finding thick enough ice to deploy these assets (due to a warming Arctic) motivated us to spend considerable time and energy ensuring we had adequate situational awareness whilst on our scientific cruises.

This paper focuses on the situational awareness products and protocols used by the team on the *Healy* cruises, although similar

[1]https://www.whoi.edu/itp

[2]https://www.mrvsys.com

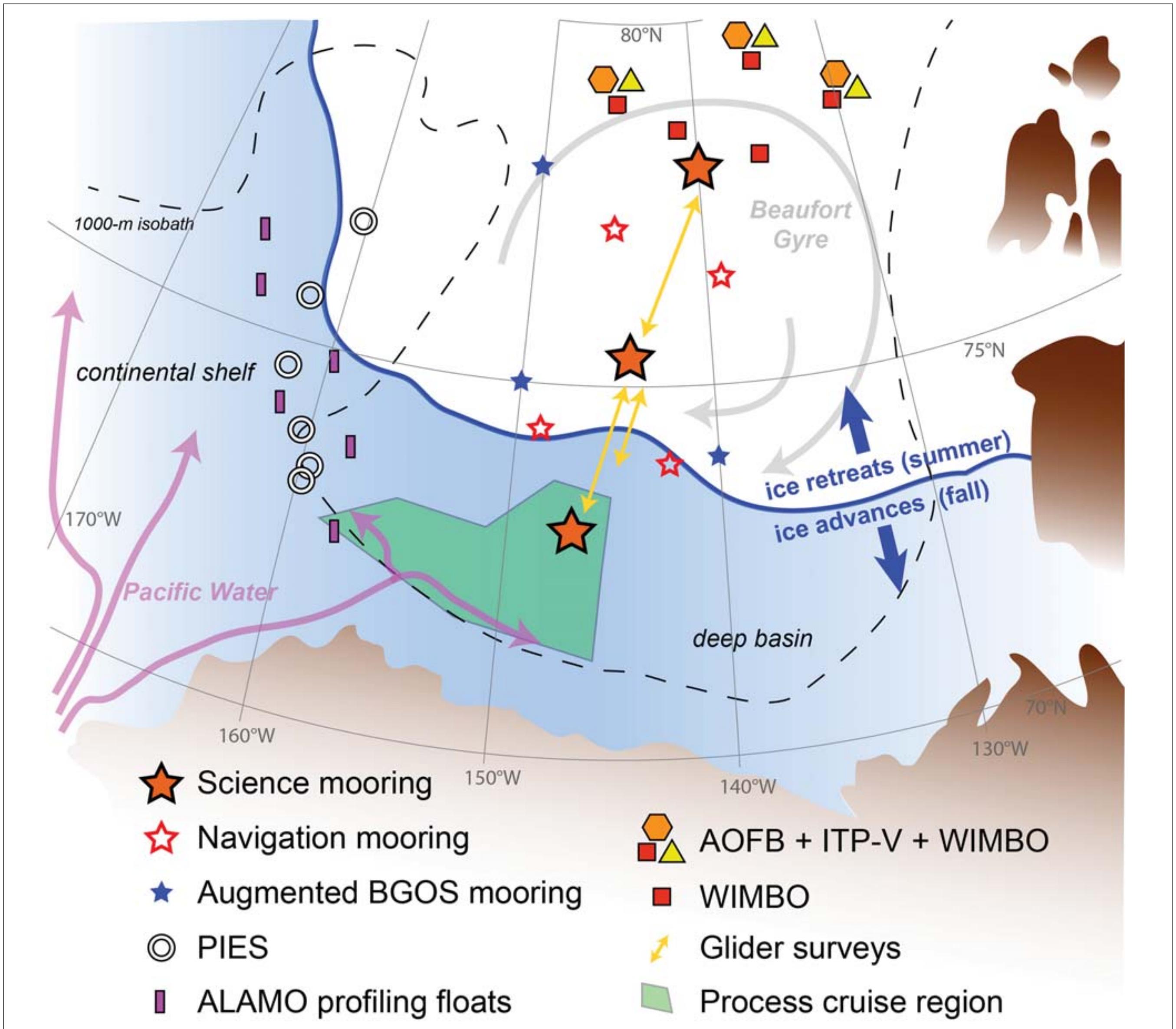

FIGURE 1 | Schematic map of the SODA observational assets. The orange hexagons (ITP-V), yellow triangles (AOFB) and red squares (WIMBO) mark instruments deployed directly onto sea ice. Note that there are 3 clusters that include all three instruments, plus two additional WIMBO sites. Science moorings (orange stars) are surrounded by acoustic navigation moorings (red stars), providing positional information for the gliders (yellow lines) when sampling under a canopy of sea ice. The *Sikuliaq* process cruise took place in the region highlighted in green. *Healy* deployed the moorings and ice instruments (up to 80°N). Argo and ALAMO floats (purple triangles) and PIES monitor circulation from the shelf to the deep basin.

protocols were utilized by the *Sikuliaq* team. Our intent is to highlight the protocols and procedures, along with the close relationship between the science users, the ship operators (here, the United States Coast Guard), and the supporting agencies that are needed in order to increase the throughput of near-real time situational awareness information to a remote field party. In particular, the U.S. National Ice Center (USNIC) was a key supporting agency for these ship-based campaigns and the SODA program as a whole. USNIC's mission is to provide global to tactical scale sea ice and snow products, sea ice forecasting, and other environmental intelligence services for the United States government, and the programs it supports. USNIC routinely provides up-to-date analyses of the ice types and position of the ice edge on its public website, but it can also provide targeted analyses for specific missions and research programs.

Situational Awareness Products

Seamless access to, and an understanding of, satellite images, model output, weather charts and other observational products, is essential to provide the situational awareness that one needs to excel in the Arctic marine environment. There are a wide range of products that are freely available from different space agencies, weather outlets, and associated organizations. Exactly which products are routinely used operationally depends on the expertise of the team along with the needs and location of the mission. Normally there is no single product or service that provides an ideal solution, so effective situational awareness must be achieved through the blending of several products. This multi-product approach reinforces the need to seriously consider the tools and formats required to support the integrated visualization of all the geospatial information products. By identifying the suite of products needed, and being familiar with their visualization and interpretation, a vessel operating in ice-infested waters should be able to navigate through, or around, the sea ice more effectively, and thus efficiently and safely achieve the objectives of the mission.

It is the most up-to-date products that have the maximum value. Generally, the time-window associated with situational awareness products is usually less than 24 h from the time of collection. Forecasts, such as weather predictions, are valuable out to about 5 days, and this advanced knowledge will allow for significant weather events (that could affect operations) to be identified and ensure preparations can be made in advance. **Figure 2** captures the time-period associated with the tactical planning for forecasts (Tactical Future) and near-real time data such as satellite observations that have been collected (Tactical past). It also shows the varying spatial resolution of available products, with higher resolution generally providing only local coverage, and lower resolution information required for wider regional coverage.

It is beyond the scope of this document to provide links to all the various satellite, modeling and weather products available. But many products that are routinely accessed by the ship operators and/or field-based personnel are listed in the catalogs maintained by, amongst others, the United States National Aeronautics and Space Administration (NASA) and the EU Copernicus services. Most of these products are available at no cost, but they often have challenges associated with automatically downloading them and/or making them available in a format that is useful to specific users. Resources exist online to browse and identify relevant products, like the Polar View consortium[3] and NASA's Worldview https://worldview.earthdata.nasa.gov.

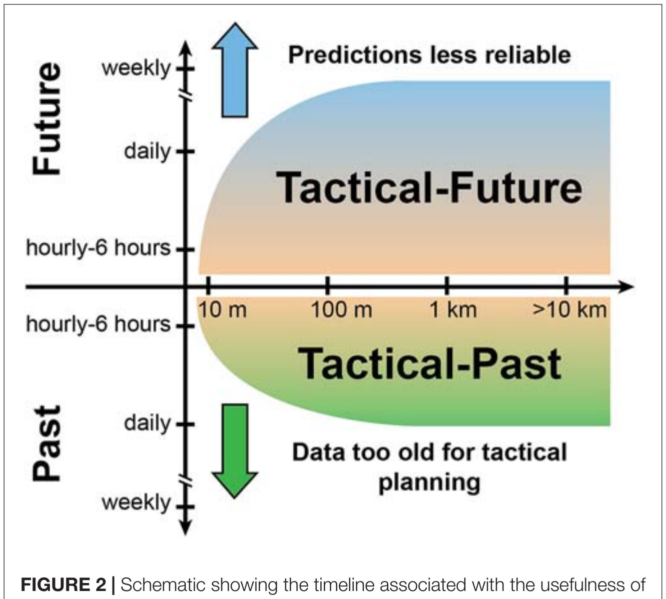

FIGURE 2 | Schematic showing the timeline associated with the usefulness of Earth Observing, modeling, and forecast products. The older the product the less useful it becomes for tactical planning. Different uses will likely require products with different horizontal resolutions (horizontal axis) and coverage.

For completeness we provide an overview of the products sent to, and utilized by, our field teams aboard *Healy*:

(a) Sea ice products: ice conditions change constantly, requiring information on a wide range of scales. We utilized the following Earth Observation products:

- Synthetic Aperture Radar (SAR) satellite imagery: SAR is routinely used for ship-based navigation in ice covered seas. The advantage of SAR images is that they are high resolution, can see through the polar night and ubiquitous Arctic clouds, and most importantly the backscatter characteristics (the amount of energy that returns to SAR sensor) can be used to clearly distinguish sea ice floes, sea ice ridges, leads, and ice type (e.g., Kwok et al., 1999). Furthermore, the motion of the sea ice can be derived from repeat pass SAR imagery. For our needs we utilized both publicly available SAR imagery (e.g., Sentinel-1), as well as others specifically ordered to support the mission (e.g., RADARSAT-2, COSMO-SkyMed, and TerraSAR-X).
- Visible imagery: visible imagery has the advantage of being relatively easy for untrained personnel to interpret; it can be thought of as equivalent to a photograph. In addition, many vessels have a local onboard reception capability for visible imagery (e.g., DARTCOM) which provides access to imagery independent of internet connectivity. Visible imagery does have the disadvantage that it cannot see through the polar night or clouds (a limitation in the polar regions), and thus many images may not be utilized to their full potential. The SODA shore-team occasionally downloaded MODIS visual images directly from the tools provided in Worldview.
- Passive Microwave: since the late 1970's passive microwave-derived ice concentration maps have been available over the Polar Regions. These daily images provide a pan-arctic overview of the ice concentration and extent. While they have relatively low spatial resolution, they do provide a good, reliable, routine and daily representation of ice conditions, particularly in Winter and Spring, with reduced accuracy in Summer and Fall due to ice surface melt.

[3]https://www.polarview.aq

- Ice charts: the United States National Ice Center (USNIC) regularly provides ice charts detailing the ice types and position of the ice edge. In addition to products publicly available, USNIC specialists can provide targeted analyses to projects supported by United States agencies, identifying regions of older, thicker ice for example. In our case, it was this ice type that we wanted to deploy our assets on, as it gives them the best chance for survivability. We utilized both the standard ice charts and their specialized product.

(b) Weather products: daily access to the latest weather forecasts is mandatory for any field program. The Arctic weather can be severe, and an up-to-date picture of the local weather conditions is essential. We note that ships often have access to separate targeted weather reports (e.g., *Healy* receives daily reports from the Naval Fleet Weather Center Norfolk VA). More generally, access to forecasts is needed for ‘on the fly’ planning as Arctic field campaigns are very weather dependent. Ideally, 12, 24, 48, and 72 h forecasts should be available daily.

- Weather charts: partners at the United States National Weather Services also provided targeted weather forecasts to the ship operators and scientists in the fields, complementing more broadly available tools displaying weather conditions and forecasts. For example, the https://www.windy.com site maintained by a private company elegantly displays the European Centre for Medium-Range Weather Forecasts (ECMWF) and Global Forecast System (GFS) forecast models.

(c) Model products: some variables, such as sea ice thickness or certain ocean properties, are not available in near real-time. For these products we relied on model output.

- Model sea ice extent, thickness and drift data were obtained from the Naval Research Laboratory’s high-resolution Global Ocean Forecasting System (GOFS) model. This output, with forecasts over the next 24–48 h, was made available for the Chukchi and Beaufort Seas (the SODA operational area).

Other products are also derived in near-real time from analysis of SAR and other remote sensing products. For example, daily sea ice drifts based on a Maximum Cross Correlation technique are now routinely available from various data centers (e.g., European Organisation for the Exploitation of Meteorological Satellites (EUMETSAT), Ocean and Sea Ice Satellite Application Facilities (OSI SAF)]. Some projects augment these capabilities with specific modeling efforts – for example, the Sea Ice Drift Forecast Experiment (SIDFEx[4]), to predict the drift of the Multidisciplinary drifting Observatory for the Study of Arctic Climate (MOSAiC).

[4]https://sidfex.polarprediction.net

Communication Limitations of Operating in the High Arctic

Moving data to and from vessels operating at high latitudes presents challenges beyond those encountered at lower latitudes. The primary mode for a vessel to move and receive data is through satellite communication systems, which is normally achieved by C, Ku, or Ka-band transmission via high-orbit geosynchronous satellites. These systems maintain a high equatorial orbit, so that their apparent position as viewed from the Earth’s surface does not change. These large spaceborne communication assets are extremely expensive and difficult to develop, manufacture, launch, maintain, and operate, and accordingly tend to be designed and configured in ways intended to maximize revenue, rather than enable and enhance communication in the sparsely populated polar areas. As a result, there are only a few geostationary communication satellite systems available in polar regions (Inmarsat, Eutelsat, Thuraya, Intelsat, etc.), and all have limited coverage poleward of 75°, and essentially no coverage above 80°N (**Figure 3**).

At latitudes above 80°N and for applications requiring less bandwidth, one can use low earth orbiting (LEO) communication satellites, of which the internally routing Iridium satellite constellation is the main provider. As LEOs are deployed in large numbers they are able to provide full global coverage for voice and data, although the bandwidth is severely limited (around 1,300 bps). We note that a new generation of Iridium satellites, known as CERTUS, has the potential to further revolutionize data transmissions in the high Arctic by increasing the bandwidth by about a factor of 50 (Jones et al., 2019).

SYSTEM DESIGNED TO ENHANCE SITUATIONAL AWARENESS

Overview

Perhaps the most critical component of situational awareness is the need for good lines of communication, along with clear mission objectives. Starting several months before the field program, the team of SODA investigators held regular teleconferences, which were aimed at establishing the needs and priorities of the mission, as well as identifying Partners that were essential to the success of the mission: the logistics providers (in our case, the USCG), and the operational sea ice charting community (primarily USNIC).

Regular communication and coordination between the science party, the USCG and the USNIC allowed the SODA team (and its partners) to identify what situational awareness products were needed, and who could provide them. The next step was to develop the mechanisms to automatically obtain these products as soon as they became available from the providers, archive them on a data-server in a logical manner, and to provide the protocols to automatically ‘push’ these products to the field-team, or for the field-team to ‘pull’ the products from the server. An overview of the developed system (**Figure 4**) is provided in this section, and the components are described in more detail below.

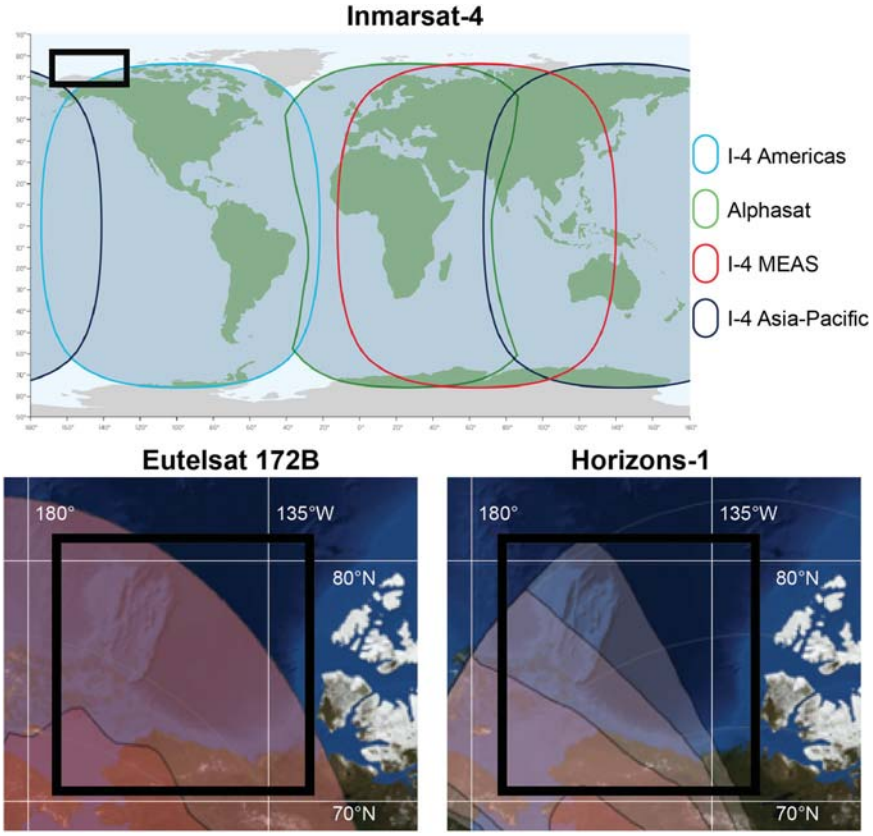

FIGURE 3 | Map of Ku band coverage projection from **(top)** the Inmarsat constellation, from inmarsat.com, for **(bottom left)** Eutelsat 172B North Pacific Ku-band transceiver. Increasingly red shades indicate larger relative effective radiative transmit power of the satellite (signal strength). SODA operation region is highlighted (black rectangles).

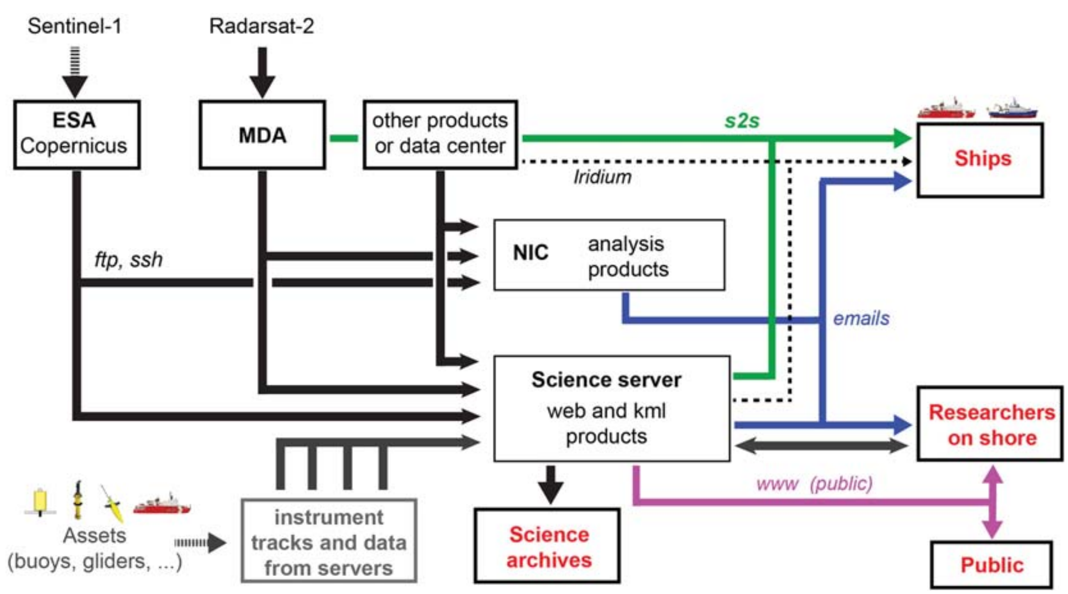

FIGURE 4 | Block diagram of the information sharing during the SODA field campaigns. Data and product providers (black boxes) provide information to users (red). The system and its connection pathways (arrows) are described in detail in the text.

The three black boxes in upper left in **Figure 4** represent the satellite remote sensing and other essential situational awareness products (see section "Ordering and Acquiring Products"). These were automatically downloaded directly from data providers via fast and secure protocols (solid black arrows in **Figure 4**) by both the USNIC and a science server located at the Applied Physics Laboratory, University of Washington (APL-UW). Each product was obtained by slightly different means: Sentinel-1 data were available through the ESA Copernicus servers, whilst for RADARSAT-2, a direct connection between the science and the prime contractor, MacDonald Dettwiler and Associates (MDA), was established to limit the latency in obtaining the images. Other products, such as ice concentration, weather charts, and model outputs, were also included in the suite of products shared and archived. In addition, a centralized database of the hourly positions (drift tracks) of all deployed assets was maintained on the science server (**Figure 4**, gray box; see section "Drift Tracks From Deployed Instrumentation"). Some products, such as the USNIC ice analysis charts (as well as their bespoke SODA product), were distributed to investigators and ships via email (**Figure 4**, blue arrows; see section "Operational Sea Ice Analysis From USNIC").

To ensure all products were up to date, they were automatically downloaded as soon as they became available from the provider and processed on a science-server at APL-UW (RADARSAT-2 were processed directly by MDA for *Healy*). Because of known communication limitations, satellite products were resampled into different spatial resolutions; high-resolution/large file size images for good bandwidth regions, through to low-resolution/small file sizes for lower bandwidth regions. An additional high-resolution product was produced for specific areas, e.g., such as small regions around the planned mooring sites. To further ensure efficient transfer, a low-resolution version of each image was produced and posted on a website as both a Google Earth kml and a geotiff (**Figure 4**, pink arrows; see section "Data Visualization"). These products were also made available to the public. All remote sensing data and products were archived on a separate server, for future analyses and processing.

To ensure the latest information was held by all land-based and ship servers they were synchronized using Ka-Ku-band connection (**Figure 4**, green arrows; see section "Data Transmission: Getting Data to the Ships"). When *Healy* sailed out of range of fast Ka-Ku-band communication, smaller file sizes were transmitted through the Iridium connection (**Figure 4**, dashed arrows).

Ordering and Acquiring Products

SAR: Sentinel-1 Products

Sentinel-1 is a pair of satellites, Sentinel-1A and -B, launched in 2014 and 2016, respectively, that provide all-weather imaging coverage using C-band (5.405 GHz) synthetic aperture radar (SAR). The satellites are part of the European Copernicus Programme, which has a further five types of Earth Observing satellites, all providing routine operational monitoring over large areas of the globe. These are made freely available to all users in near-real time (NRT, <24 h) through Copernicus' open data policy. Operational users including the Copernicus Marine Environment Monitoring Service (CMEMS) and Collaborative Ground Segment operators including the Norwegian Meteorological Institute, which can also access data in near-real time (<3 h).

The satellites were built and operated by the European Space Agency (ESA) on behalf of the European Commission Copernicus Programme. The imaging capabilities of Sentinel-1 are similar to those of the older Canadian RADARSAT-2, but with fewer imaging modes. The two main modes are (1) Extra Wide (EW) with a swath width of 400 km and pixel size of 40 m, typically used for maritime monitoring including the polar regions, and (2) Interferometric Wide (IW) with a swath width of 250 km and higher spatial resolution (20 m pixel size), used for land monitoring. An additional two modes, Stripmap and Wave, are used for high resolution disaster and emergency mapping, and ocean background monitoring, respectively. The imaging can also be conducted as single co-polarization (HH or VV) or dual co- and cross-polarization (HH + HV or VV + VH), with single polarization being used over open ocean and high sea ice concentrations, and dual polarization being used over the marginal ice zone (MIZ). Apart from the Stripmap mode the monitoring modes acquire data according to a predetermined coverage that is designed in consultation with users, primarily the Copernicus services. As SAR is a power intensive and high data volume instrument, operating time is limited to 25 min per orbit. This can prioritize daily coverage of areas of the Arctic and Antarctic of European interest, with areas outside of these regions, including the Beaufort Sea, being covered less frequently.

Data are available via a number of web portals and online sites, depending on the user. The primary source is the Copernicus Open Access Hub[5]. This, and a number of other portals specific to Copernicus services or national space agencies, e.g., the Norwegian Collaborative Ground Segment[6], provide a rolling archive of the most recent data using a common application program interface (API). For older archive data, Copernicus has set up a number of Data and Information Access Services (DIAS) that provide data access and commercial cloud computing resources. In addition, ESA established a number of Thematic Exploitation Platforms (TEPs), including the Polar-TEP[7], that provide a similar data exploration and processing capability.

The use of a common API allows scripting for automated downloading and processing of Sentinel-1 data, for example the Check ESA SciHub routine[8] and ESA SNAP software[9]. Such. scripts were used during SODA to automatically download all images overlapping with a polygon extending from 70 to 83°N and 170° to 130°W.

[5]https://scihub.copernicus.eu/
[6]https://satellittdata.no/
[7]https://portal.polartep.io/
[8]http://doi.org/10.5281/zenodo.159450
[9]https://step.esa.int/main/toolboxes/snap/

SAR: RADARSAT-2 Products

The USNIC typically orders RADARSAT-2 imagery on a monthly basis to meet the needs of USNIC analysts creating their freely available daily and weekly ice products, as well as to support active missions (like SODA) in the Arctic. When planning and placing orders, the USNIC employs a "follow the marginal ice zone (MIZ)" approach. The MIZ is a transition area between open water and full ice cover, it is typically the most dynamic during the freeze-up/melt seasons. Orders are focused on regions for which Sentinel imagery is not available and placement is based on current ice conditions, past climatology, and current forecasts. A bulk imagery request covering a 30-day period is submitted to MDA 1–2 weeks before the first image acquisition. Orders are sent to MDA for approval and to resolve any conflicts with other commercial RS-2 users, due to tasking limitations of the satellite. Generally, the USNIC orders images in ScanSAR Wide mode, which provides the largest, 500 km, footprint and 100-m resolution.

In addition to placing RADARSAT-2 imagery orders for nominal operations, the USNIC also creates customized imagery plans for special support missions, such as the SODA mission. The USNIC communicates extensively with active missions to best utilize joint resources. This includes staying updated on a ship's planned intended movements (PIM), while providing updated kml files which show imagery footprints and metadata. The USNIC is able to adjust RADARSAT-2 imagery orders up to 3 days prior to an image acquisition without incurring financial penalties. This allows the USNIC to continually update plans to account for changing sea ice conditions and ship movement. Orders placed, or altered, with less than 3 days' notice have a much higher risk of not being acquired due to conflicts or other tasking limitations.

Images are acquired and downloaded from one of several ground stations utilized by MDA. MDA then performs initial processing of the acquired data and posts the data to an ftp site. During SODA, users were alerted via email that a new file was available. Between 20 September and 31 October 2018 (40 days), MDA acquired 147 images in the Beaufort Sea for the USNIC, which were passed to the SODA science team and *Healy*. The time interval separating the image acquisition to the file being available on the MDA ftp site (latency) had a bimodal distribution: for images acquired between 0000 and 0400 UTC (110 images), the latency was 6.7 ± 1.5 h, but posting was much faster for images acquired from 1,500 to 1,800 UTC (30 images, 0.8 ± 0.2 h). MDA has several latency options available when imagery orders are placed. Two latency options were utilized for the SODA missions, near-real time (the fastest option) and rush. Imagery defined as near-real time is made available up to 4 h after being downlinked from the satellite to the ground station. This option was utilized for acquisitions from 1,500 to 1,800 UTC, allowing the USNIC analysts on duty to utilize the most up to date imagery. When analysts are not on duty, the rush option is utilized which allows for a longer latency (6–24 h). This allows the USNIC to optimize financial resources while ensuring that mission needs are met. All images were available within 12 h of acquisition, with the fastest delivery being 0.3 h.

Other SAR Products

During the SODA campaigns, additional high-resolution SAR remote sensing imagery on specific targets (such as the on-ice instruments clusters, and *Sikuliaq* during the process study cruise) was ordered, purchased, and processed by the Center for Southeastern Tropical Advanced Remote Sensing (CSTARS) at the University of Miami. The cost of these images has to be weighed against their utility. In this case, guided by the SODA Science Plan (Lee et al., 2016), the very high-resolution images (order of a meter) are important for estimating ice characteristics around the instruments measuring the ice/ocean interface. These images were primarily collected by the COSMO-SkyMed (COnstellation of small Satellites for the Mediterranean basin Observation) system operated by e-GEOS for the Italian Space Agency (ASI), and the TanDEM-X/TerraSAR-X system operated by Airbus Defence and Space for the German Aerospace Center (DLR). CSTARS is a satellite ground station and provided download and processing services for both satellite systems. During the process cruise, low resolution versions of the image products were provided via email to users on the *Sikuliaq* within 3 h of acquisition.

CSTARS coordinated with the satellite operators directly to order the imagery. The small footprint (40 by 40 km is typical) of high-resolution Stripmap mode imagery presented an additional challenge for this process compared to the acquisition of wide-area ScanSAR imagery. Requesting a satellite image within a cost-effective 24–48-h (depending on system) window prior to collection required forecasting the target's location in approximately 30–54 h. For the process cruise, this involved consultations between a CSTARS scientist on board the *Sikuliaq*, the chief scientist, and the ship's officers, the outcome of which was passed along to CSTARS personnel at the ground station, who then performed a feasibility analysis to match target time and location with satellite orbit characteristics, before ordering the optimal acquisition. The process was similar for the on-ice instrument clusters, with CSTARS personnel typically utilizing the current position of an asset and a simple persistence drift model to forecast its location at image acquisition time. The success rate of capturing the target in imagery depended on many factors, including the nature of the target and environmental conditions, but generally exceeded 85%.

Passive Microwave

Pan-Arctic sea ice conditions derived from passive microwave instruments have been a standard product for over 40 years. We obtained daily from AMSR2 (and AMSR-E) sea ice concentrations in near real time (Spreen et al., 2008) and posted at https://seaice.uni-bremen.de/sea-ice-concentration/amsre-amsr2/. This service is part of the GMES project Polar View and of the Arctic Regional Ocean Observing System (Arctic ROOS).

Drift Tracks From Deployed Instrumentation

SODA, like many similar large field programs, employed a diverse mix of platforms and sensors. Visualization of asset

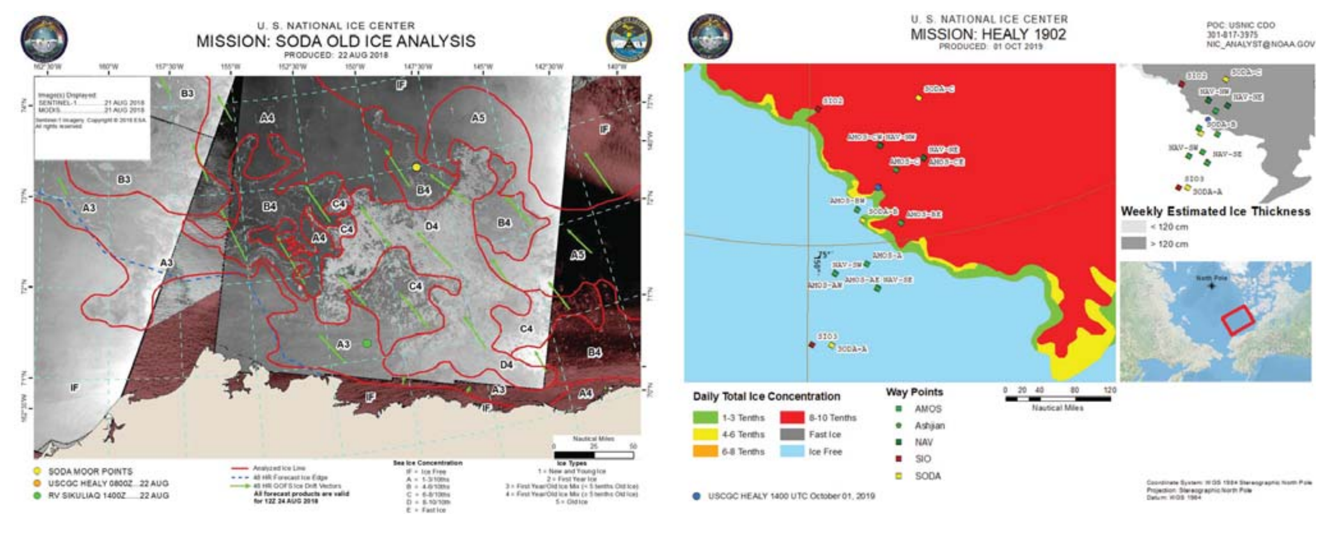

FIGURE 5 | (Left) Annotated image showing ice analysis from USNIC for August 22, 2018. Background is a mosaic of SAR images from RADARSAT-2 and Sentinel-1 (gray images), and visual (MODIS) images (pink to black images). **(Right)** USNIC ice analysis for October 01, 2019, showing ice types and estimated thickness around the SODA array during the recovery cruise.

locations was critical for maintaining efficient operations and optimizing the use of observing resources. Every instrument transmitted its location on an hourly (or less) basis, together with other data from on-board sensors. The owner of each instrument typically has their own server where they gather the transmitted position information and data. The science server at APL-UW automatically gathered this information for all the instruments listed in **Figure 1** and posted their respective time-stamped positions (tracks) in a common format in a common place.

It was quickly realized that any single graphical file or kml generated won't satisfy everyone. Our solution was to make a simple compromise kml file that worked for the users on the ship and on shore, *and* produce, uniformly formatted, time-latitude-longitude text files for every instrument. It should be noted that simply pointing to all the different servers is not enough, since protocol issues and format changes inevitably occur. An often neglected challenge is that several hours per week are typically spent by someone on shore to maintain simple processes like generating the position text files from various instruments. These files are in turn used by many researchers both in real time and in post processing.

Operational Sea Ice Analysis From USNIC

An important component of the situational awareness during SODA was two-way communication with the United States National Ice Center (USNIC). At an early stage USNIC was engaged with the SODA scientists and detailed plans were drawn up to provide regular annotated images of the ice conditions in the operating area (**Figure 5**), well before the ship sailed and instruments were deployed. In addition to being invaluable during the field program to guide operations, having access to these analyses before the cruise enabled the team to obtain a good understanding of the ice conditions in the region of operation well before they are actually encountered.

These analyses combined all the remote sensing products available to the USNIC analysts. Typically, the USNIC supplements visual satellite images with images from Synthetic Aperture Radar (SAR) satellites, some of them available publicly (e.g., Sentinel-1 from the European Space Agency) and other specifically ordered to support their mission (e.g., RADARSAT-2). For SODA the USNIC specialists were asked to identify regions of older, thicker ice. It was this ice type that we wanted to deploy our assets on, as it gives them the best chance for survivability.

Formatting/File Size Challenges

Full resolution extra wide swath (EW) or ScanSAR Wide SAR images can have a pixel resolution smaller than 50 m and be several hundreds of km wide. Higher resolution products can have resolution on the order of a meter. As a result, their file size is generally too large to be sent over a bandwidth-limited communication system. After compression and downsizing, each of the S1 and RS2 overlays were reduced to about 300 KB in size. This size can reasonably be transmitted even with low-bandwidth connections.

Understanding the environment, the needs of the mission, and the limitations in communication ensures that the most relevant information can be extracted from the latest situational awareness products for a specific region. This knowledge is particularly important as it guides decisions regarding how much a product can be downgraded in resolution, and/or compressed in order to still be useful for evidence-based decision making in the field. During SODA, detailed images were generated with 100 m resolution over a 100 km $\times$ 100 km box centered on a planned operational site, such as a mooring deployment. Each of these high-resolution images was between 3 and 4 MB in size.

Data Transmission: Getting Data to the Ships

The ship-to-shore (S2S) system uses an open-source software package, Syncthing[10], as a robust, highly configurable and fault tolerant transport protocol which synchronizes data efficiently over any Internet connection. Data is synced between directories on ship and shore side nodes, and local area network (LAN) access for scientists can be provided by a number of methods including Server Message Block (SMB) network shared drives, File Transfer Protocol (FTP), Hypertext Transfer Protocol (HTTP), Secure Shell (SSH), rsync, etc. Syncthing is a highly customizable service allowing data propagated across nodes to be prioritized, bandwidth throttled and targeted for custom purposes. Bandwidth throttling is particularly important over satellite networks such that data syncing does not saturate limited vessel bandwidth. Only new and modified files are copied, data can be modified on either end of a sync, and data synchronization runs continually without external scripting, automatically resuming following network interruptions. Syncthing runs transparently on Windows, Mac, Android, and all Linux platforms.

For the purposes of SODA, a shore-side Syncthing server, located at University of Alaska Fairbanks (UAF), was used to sync directly to Syncthing nodes on *Healy* and *Sikuliaq*. In this configuration both *Healy* and *Sikuliaq* servers were able to synchronize data to and from shore independently of satellite bandwidth availability on the other vessel. Access to data propagated across these nodes varies from node to node:

- On *Healy* and *Sikuliaq*, a recurring automatic process uses the rsync program to push data from the shipboard node to the primary shipboard data storage array, where it is accessible to embarked science personnel.
- A shore-server, located at UAF during SODA, acted as a repository for files that needed to be transferred to and from *Healy* and *Sikuliaq*.
- Processed images or tracks and other data files were copied to a directory on a server located at APL-UW, a copy of which was pushed to the UAF shore server.

While this configuration requires data to be transmitted twice (*Healy* → Shore → *Sikuliaq*), the overall reliability of the system was maximized and worked well with no issues during the SODA cruise.

Lack of familiarity by security groups with modern distributed services and advanced techniques like those used by Syncthing is a potential obstacle for institutions with more traditional security policies. Broader adoption of distributed technologies will require more advanced security discussions and assessment.

If timing is critical, a more direct process (automated or manual ftp or sftp pull upon receipt of notification of product availability) can also be employed. In both cases the primary limiting factor is allocated throughput, which is generally a function of contracted bandwidth on the satellite transceiver. In an academic research context, this is generally a function of economic resource allocation. The return on investment becomes smaller as the ship gets to very high latitudes, further away from the Equator, and transmit power needs to increase in order to reliably attain nominal download rates.

Data Visualization

As parts of the situational awareness system will be used differently by various users, building such a system is an exercise in flexibility. We found that generating a series of network kml files that can be easily accessed through the desktop version of Google Earth (Gorelick et al., 2017) provides a good overview for shore-users with good connectivity. All products described above are therefore packaged as such, extracting only the portion of the fields relevant to the program. With the appropriate time stamp these can be used to visualize and contextualize the data.

For people onshore, we generated a kml with network links, keeping everyone up to date with the latest information. This could be done by simply adding this network link in a desktop version of Google Earth. This “network kml” pointed to the instrument tracks and the remote sensing information. For people on the ship or with limited connectivity, a compressed file that included all the track information locally could be downloaded.

For example, ice concentration maps from passive microwave, RS2 SAR images, and Sentinel-1 SAR images from 23 September 2018 during SODA cruise on *Healy* is shown in **Figure 6**.

A local kml version of these files (built by attaching the overlay in a kmz archive as opposed to pointing to a network link) were pushed to the ship and used locally. Acknowledging both licensing issues and personal preferences from various users, the same overlays are also packaged as geotiff, which can be read by various commercial software products (ArcGIS, QGIS, GlobalMapper, etc.).

All instruments have their own kml and txt files (latitude, longitude, and time) on the public server. The positions also included a simple “all_fix.txt” file which listed the latest position of each asset, which can easily be shared with the bridge, for example.

We also note the importance of archiving raw images for future science analyses. Typically, these archives are not publicly accessible, as it is important to also keep track of the security and copyright issues associated with some of the data/images. In their native resolution, SAR data in particular are often proprietary and/or sensitive. Lower resolution and derived products can usually be shared freely. As with most research sponsored by ONR and ONR Global, the SODA program has a clear data sharing agreement protecting data and intellectual contributions, while encouraging collaborations and data sharing both within the program and with the broader community.

The SODA kml is available at UW Digital Library[11] and can be downloaded and opened in Google Earth to explore the products described in this paper. The archive is 2.6 GB and includes the ship tracks (*Healy*, 2018, 2019; *Sikuliaq*, 2018), the instrument location and tracks (moorings, PIES, ITPs, WIMBOs,

[10]https://syncthing.net/

[11]http://hdl.handle.net/1773/45592

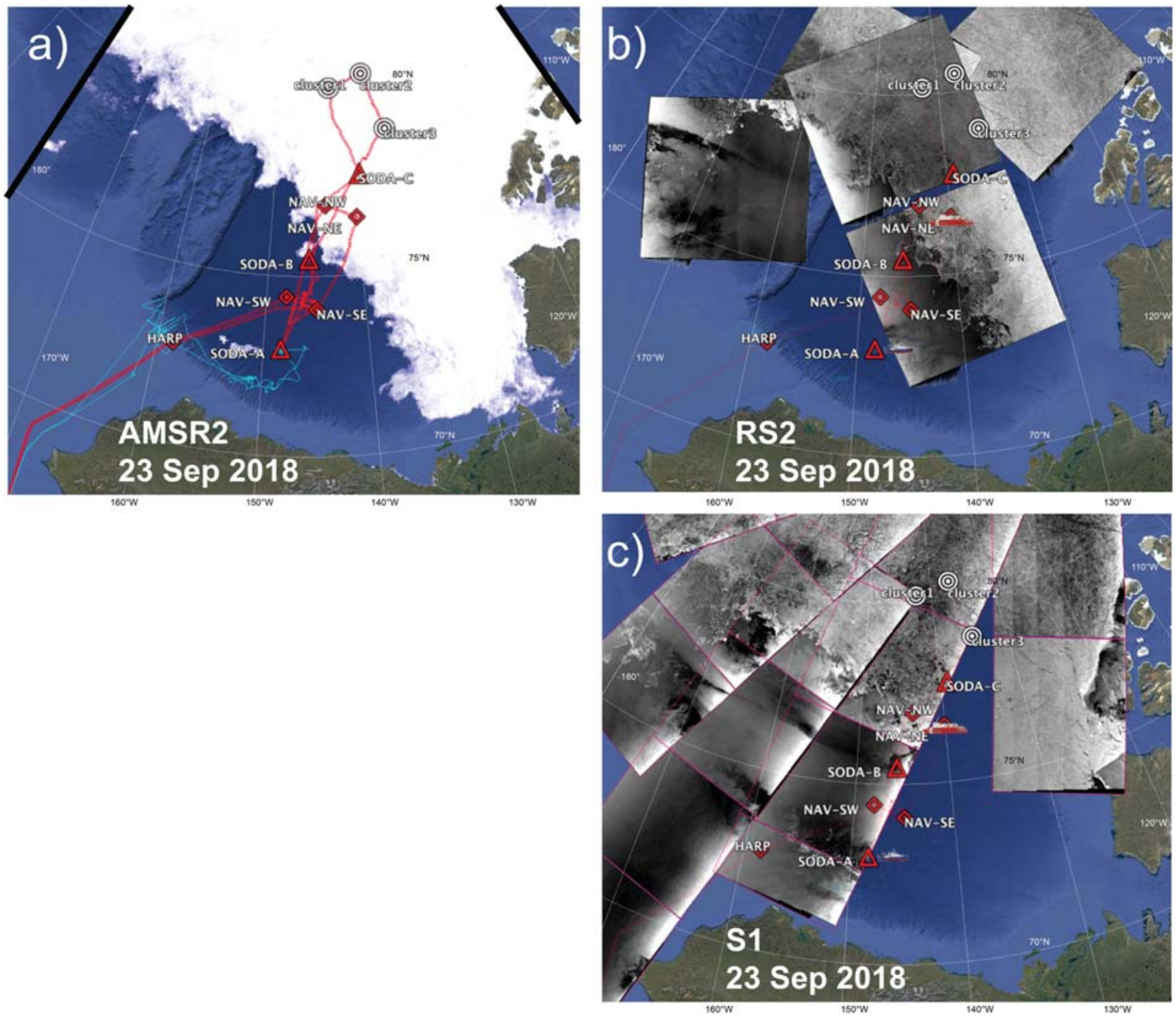

FIGURE 6 | Example of **(a)** Passive Microwave (AMSR2), displayed only between 170 and 110°W, **(b)** Radarsat-2, and **(c)** Sentinel-1 remote sensing products on September 23, 2018. *Healy* (red) and *Sikuliaq* (cyan) cruise tracks are shown in **(a)**, and the location of the ships on that day in **(b,c)**. SODA moorings and instrument clusters are also shown. Images are displayed as an overlay in Google Earth.

AOFBs, and SOLO floats), and the remote sensing images (AMSR2, RS2 and Sentinel-1, as well as the TDX and CSX images acquired by CSTARS; **Table 1**).

TABLE 1 | Satellite ice imagery acquired during SODA (2018-09-01 to 2019-10-15) in the Beaufort Sea, defined as the region 66–85°N, 180–110°W, included in the SODA kml.

Products	Number of images	Resolution, Swath	Availability
AMSR2	412 days	3.125 km grid, pan-Arctic	Public
SAR Sentinel-1	4,370 images	40 m, 400 km (EW)	Public
SAR RADARSAT-2	792 images	100 m, 500 km (ScanSAR)	Proprietary
SAR CSTARS	357 images	1 m, 40 km (Stripmap)	Proprietary

SYSTEM APPLICATIONS

Case Study 1: Navigation

Possibly the most important use of situational awareness products for a vessel within ice covered waters is to enhance the safety and efficiency of navigation. The second is to achieve the mission requirements; for SODA this included deployment of clusters of ice-based instruments and moorings in the northern Beaufort Sea. Both of these objectives demanded extensive navigation through ice-covered waters. To support extended work in the ice, an on-board USNIC analyst monitored the sea ice around the ship, along planned paths, and around the different mooring sites through the use of the imagery acquired. *Healy* did not have a helicopter available for ice reconnaissance flights.

Every evening the Captain, Officers and Chief Scientist would be briefed on the ice conditions for every possible direction the ship may steam over the next 24 h, and to plan accordingly. The briefs would contain images from RADARSAT-2, Sentinel-1 and MODIS/VIIRS with annotation (similar to **Figure 5**) showing the location of the ice edge, the ship location at the time, mooring locations, and possible paths through thinner ice and leads. From this, the Captain, Operations Officer, Navigator and Chief Scientist would decide which direction the ship would proceed to ensure efficient steaming, or to identify specific mooring locations or deploy ice-based assets. After the evening briefing, the analyst would go up to the bridge with the Operations Officer and the Navigator and aid in plotting out a course using knowledge of the velocity of the sea ice (obtained from model sea ice drift data) and the timing of the satellite images. The model sea ice drift data were from the Naval Research Laboratory's high-resolution Global Ocean Forecasting System (GOFS) model output for the Chukchi and Beaufort seas. The ice drifts and model wind data were used to brief the officers on a forecast for how the ice would move over the next 24–48 h. All these products were transmitted daily through the situational awareness system. We note that when in the ice pack, the ship and all the floes can be assumed to generally drift together, so relative course can be set using past images to navigate to specific leads or floes.

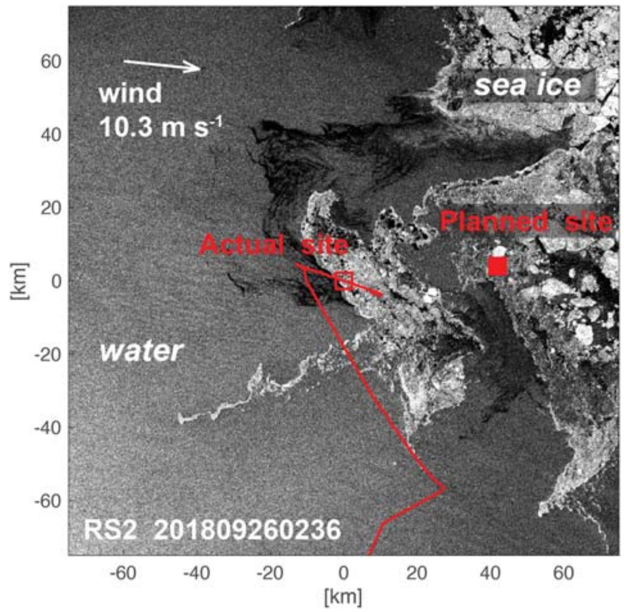

FIGURE 7 | RS2 image from 2018-09-26 02:36, 24 h before the start of the mooring deployment. Red line is the track of *Healy* during the 24-h period after the image acquisition, as the mooring deployment site was adjusted from the planned (solid red square) to actual (open red square) location. In general, gray areas represent open water (left of image), white areas are sea ice (right of image), and the dark areas are newly forming sea ice.

Case Study 2: Mooring Deployments

Ice cover complicates mooring operations, as it severely restricts vessel maneuverability and poses a threat to mooring hardware and instruments during deployment and recovery. Timely and detailed knowledge of the weather and ice conditions in the vicinity of mooring sites can be used to mitigate risk and improve efficiency by allowing the mooring team to target weather windows as well as favorable features, such as leads or areas dominated by weaker, smaller floes, and guiding path planning to optimize the ship's approach.

Deployment of science mooring SODA-B illustrates the use of targeted, rapidly delivered satellite remote sensing, and dedicated analyses to guide operations in ice-covered waters. On September 26, 2018, with *Healy* still 200 km south of the SODA-B target site, passive microwave retrievals for sea ice concentration indicated extensive ice over the site, while weather forecasts predicted strong winds. Faced with a high-risk deployment in high concentrations of rapidly moving ice, the SODA team used the imagery to identify a suitable open-water site south of the original target. Analysis of an RS2 image (**Figure 7**) received as *Healy* transited to this alternative site led to a refinement of the target, shifting west to take advantage of winds pushing ice to the east, thus acting to clear the target region. RS2 acquisition had been specifically targeted to support the SODA-B deployment, and was thus able to provide timely, high-resolution scenes suitable to guide real-time decision making. Advance planning and coordination between the SODA team and the USNIC established the communication and decision-making protocols required for nimble, highly responsive targeting of acquisitions. Guided by the image (almost a day old at that point), the ship selected a starting point in open water, at the target latitude, and transited eastward to the ice edge. *Healy* then positioned into the wind for an open water mooring deployment, beginning the operation almost exactly 24 h after the image acquisition. This application provides a good illustration of adaptive, evidence-based decision making that was guided by targeted remote sensing and weather information and bounded by significant logistical and operation constraints.

Case Study 3: Context for Upper Ocean Sampling

Toward the end of the 2018 *Healy* expedition, there was an opportunity to enhance our knowledge of the impact of sea ice formation on upper-ocean physics. Access to high-quality and recent remote sensing images (**Figure 8**) allowed the ship to take advantage of limited time available to locate the ice edge and optimize the route to sample from open waters to inside a field of newly formed sea ice crystals (frazil ice) which were slowly aggregating into pancake ice (the next stage of the ice formation cycle) under calm wind conditions. Using these images, a 'mowing the lawn' cruise track was identified which took the ship from open water though to regions of new ice formation and back out to open water a number of times (red line in **Figure 8**). The survey was also augmented with sampling from a Surface Wave Instrument Float with Tracking (SWIFT), a free drifting system to measure waves, winds, turbulence, and ambient noise at the ocean surface (Thomson, 2012). In addition to facilitating the decisions in the field, the situational awareness system, making all the positions of instruments and remote sensing images available in a centralized location and

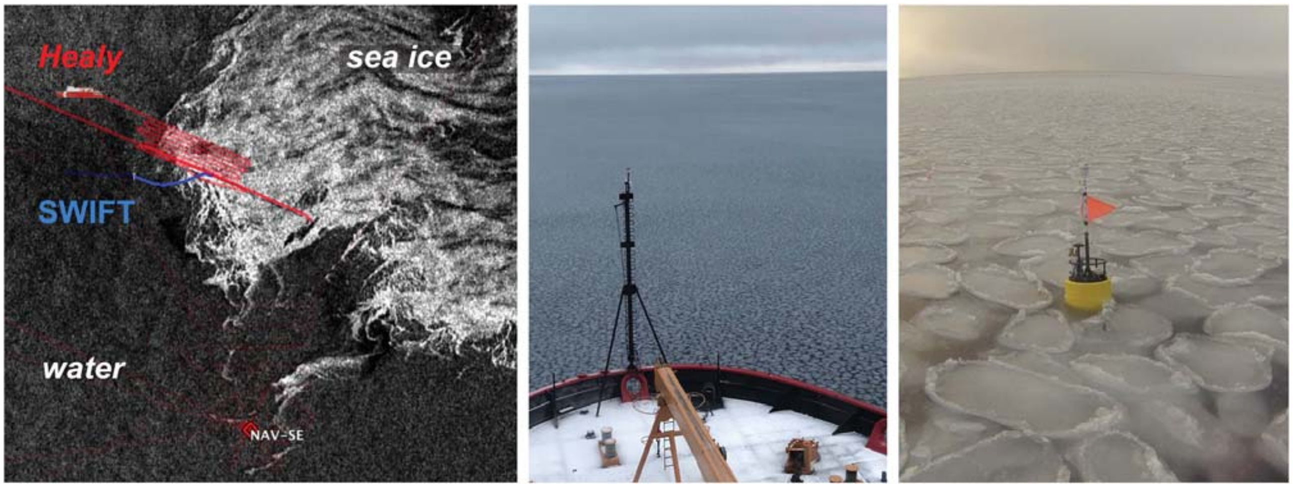

FIGURE 8 | (Left) 100 km square RS2 image (201810120308_RS2_SCWA) with 100 m resolution centered in a new ice formation region on 12 October. Location of the ship (red) and SWIFT buoy (blue) at the time of the image are indicated by their respective icons, with a 24 h track. **(Center)** Photograph of the pancake ice near the time of the image. After 12 h **(Right)**, pancakes were about 1 m in their longest dimension and 6 cm thick. The SWIFT buoy is pictured on the right.

under a uniform format, allows scientists to contextualize the observations and identify the most promising analysis ideas.

Case Study 4: Floe Selection for Ice-Based Instruments

It is clear that the Arctic is undergoing strong environmental changes, and to better understand these changes it is important to have the capability for year-round monitoring of key environmental parameters. Robust technology that is suited to this harsh environment, such as on-ice assets that monitor atmospheric, oceanic and sea ice properties, provide this opportunity. Their long-term survival is very much enhanced if they are deployed on thicker ice that is away from the ice edge, rather than regions of thin ice or open water. However, this is not always possible for logistical, scientific or environmental reasons.

The SODA science objectives demanded that the on-ice assets should be deployed in the vicinity of 75–82°N, 130–160°W. As there was no aerial reconnaissance available to the cruise, we relied entirely on remote sensing imagery to determine suitable floes for each cluster's deployment. Prior to the cruise we worked with USNIC to identify, through remotely sensed products, regions of multiyear ice that were located within the box: In the absence of liquid water on the floe surface, these show a distinct brightness contrast to younger ice in SAR images. This partnership continued during the cruise, and daily SAR images (obtained through the situational awareness system) were used to identify a series of large multi-year ice floe targets that have potential as deployment sites. These target floes were ranked and their locations, including drift calculated from received model data, were presented to the *Healy* Captain and science stakeholders. If the relevant weather charts showed good conditions, the ship sailed to the vicinity of the highest ranked floe, whereby a combination of its latest known position, ship's radar and personnel with binoculars (lookouts) were posted to find the floe. Since the target floe is rarely the only MY ice in a given region, any suitable floe with similar properties might be selected during the transit to the appointed spot.

While remote sensing offers a versatile mechanism to evaluate candidate ice floes, there is no substitute for *in situ* observation. Once a target floe was identified, the *Healy* Conning Officer would slowly guide the ship into the floe – this maneuvering was typically done from the 'aloft conn' station, which offered throttle and rudder control from a higher vantage point on the ship (a higher height of eye and consequently greater field of view). As the vessel slowly broke through the ice, embarked researchers would view the ice thickness. This is easily gauged as the ice blocks immediately beside the hull often turn on their side, allowing the ice thickness to be directly compared to a calibrated measuring pole which hangs over the ship's rail above the ice. These observations might take place from the bridge, aloft conn, or other convenient station. Even on-site, the remote sensing effort continued to be useful for deployment site selection within the target floe, as it could delineate the expected size of the floe and the degree of ridging, which is not always evident in restricted visibility or flat lighting conditions.

If the ice appeared to be of suitable thickness for the instrumentation – a criterion of 70 cm or more was generally desired – the ship was slowly brought 'hove-to' with the floe. Once *Healy* was determined to be dynamically stable with the floe, an ice team was dispatched to confirm that the floe was suitable, drilling with ice augers to determine a representative thickness value and checking whether any frozen melt ponds might present risks to personnel. This method was favored over more complex alternatives (such as electromagnetic induction techniques) because of the immediate and unequivocal result and the simple, lightweight equipment required (augers were attached to a powerful electric hand-drill). Importantly, drilling provides a direct measurement of ice thickness without the need for collaboration. If safe, the assets were deployed, which might be

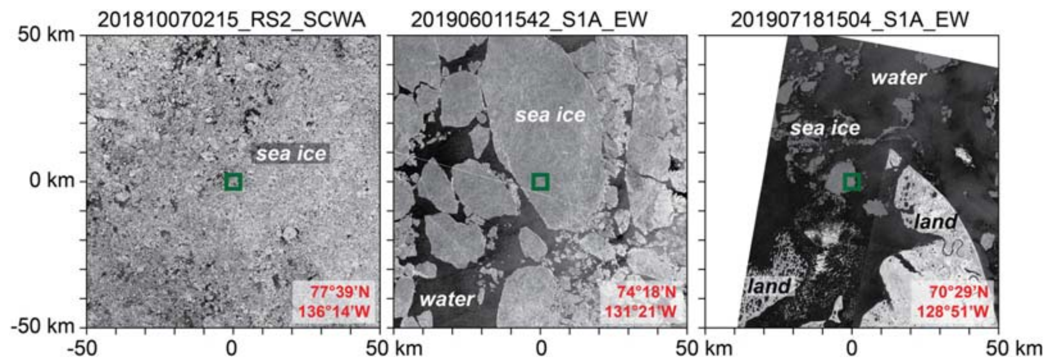

FIGURE 9 | Ice conditions shortly after deployment of WIMBO1 (20181007) and in the following spring (20190601) and summer (20190718) as it drifted 100 s of kilometers south. The floe chosen for WIMBO1 deployment was one of the last floes to melt near the Canadian coast. Bottom row shows 100-m resolution SAR images in a 100-km box centered on WIMBO1 (green box) from October 07, 2018, June 01, 2019, and July 18, 2019. Cape Bathurst is apparent in the last SAR image.

a prolonged operation over several hours or continuing the next day, following a break overnight. If the situation was unstable, we resumed the search, transiting to neighboring floes of similar thickness if available or, failing that, the next highest-ranked floe on the list. It should be noted that in one event, as the team proceeded to offload equipment, a crack developed and propagated along the floe between the team and ship. Given the possible risk of the team being separated from the ship, the equipment and the team were immediately evacuated from the floe. Thus, highlighting the need to always be aware of the local environment, and to act appropriately when it changes. Afterward, the ship proceeded onto a new candidate floe nearby and little time was lost.

An example of the floe choice for the deployment of WIMBO 1 can be seen in **Figure 9**. It clearly demonstrates the value of having good situational awareness as the selected multi-year ice floe was particularly robust. Though only 93 cm ice thickness at the buoy site, it was the thickest encountered in these southerly regions of the ice cover, and hence was one of the last to completely melt in the warm-water adjacent to the coast (green box in **Figure 9** shows location of WIMBO 1 on the floe). Our process thus demonstrably selected a good platform for the deployed asset.

SUMMARY AND CHALLENGES

Over the past few decades the ice, ocean and atmospheric conditions within the Arctic Ocean have changed significantly, which has led to more challenging marine-based operations. The combination of a changing environment with a predicted increase in marine traffic within the Arctic waters suggests accurate situational awareness is essential.

During this period, weather predictions have become more reliable, the availability and selection of satellite-based products has increased dramatically, computer model output is more accurate and satellite communications in the polar regions have improved (albeit slowly). By making the best use of these technological advances, partnering with expert organizations, and having clear goals and lines of communication we can improve the situational awareness through enhancing access to these data streams in a timely fashion, even in remote regions of the Arctic Ocean. This naturally leads to better decision-making across a broad range of operational and scientific scenarios. Successes, challenges, and closing thoughts from each of the different users of the SODA situational awareness system are offered below as a summary.

Coast Guard

Safe operation of an icebreaker in high latitudes requires both good knowledge of environmental conditions and clear communications of the various requirements and desires of the users. The USCG benefits greatly from the relationship with USNIC and its ice analysts. While the ship's navigation and operational systems are separated from the science-centered situational awareness system described here, the availability and sharing of information across the science, ship-board technical groups, and *Healy* Command, makes planning and executing the science mission of *Healy* easier.

The SAR Order Desk Lead at the USNIC sent the Radarsat2 order swaths via kml to the analyst and shipboard technical group on board *Healy*. This ensured that the crew knew when we would have imagery on the bridge and saved bandwidth when only a corner of the image was necessary to download for proper situational awareness. Similar products showing future Sentinel-1 images are also available from Polarview. Knowledge of future acquisitions is very useful for all decisions in the field.

On a more local scale, *Healy* utilized a Rutter Sigma S6 Ice NAV Radar to support navigation through ice, particularly in poor weather conditions and low visibility (a common phenomenon in the Arctic). This Rutter ice navigation radar system processes the signal from the ship's radar system and enhances the definition along ice edges; this can indicate the presence of thick ice floes with weathered edges and identify ice leads. This improved fuel efficiency, reduced wear and tear on the vessel from the battering of breaking ice, and ultimately provided more time to fulfill mission requirements.

Although this paper focuses on the 2018 campaign, it is worth noting the additional challenge faced in recovering the SODA moorings in the 2019 *Healy* mission. Even minor latency in receipt of ice imagery quickly erodes its tactical value. Mooring recoveries require a precise understanding of the net ice drift and presence of polynyas and leads. A high-fidelity image will inform the party on required time on-scene and provide indicators as to the efficacy of the objective (i.e., moving onto the next target and returning to the original objective at a later time.

United States National Ice Center

USNIC benefits from communication and feedback from the customer on support and ice conditions. Constant communication of sea ice observations from the embarked analyst to the USNIC was used to validate and improve the location of the ice edge, multiyear ice, and knowledge of hard to detect new ice formation. Then, forecasters at the USNIC adjusted their analysis of the ice locations to align with the most recent imagery.

High resolution GOFS model ice drift data and model winds were used to make a best guess on how the ice was moving to make the imagery useful 6–12 h after they were acquired. The limitation on ships to the usefulness of old imagery is on obtaining the ice drift forecast and being able to mentally shift the ice in the correct direction. Having a USNIC analyst on board with this data readily available and knowledge on forecasting helped to alleviate these limitations for *Healy* and SODA science team.

Shipboard Technical Group (STG)

The STG is the provider of expertise, personnel, and instrumentation to scientists that use *Healy*, the shipboard technical group is an important component of the ship's situational awareness system. When incorporating ice imagery into navigation systems, often there was a challenge in converting between different projections (Polar Stereographic and Mercator) – this would often result in image distortion when overlaid onto charts, particularly at the extremes of the image. The STG was able to resolve the issue through collaboration with USNIC and MDA. Furthermore, parties using ice imagery should be cautious to the potential for offset from image center when overlaid onto a chart. In some cases, the image appeared several miles offset from what was observed *in situ* (well beyond the effect of ice drift for the given time period between image capture and receipt).

Science

Arctic marine field programs can pose complex challenges, with multiple research teams aiming to conduct coordinated observations above, on and below the sea ice, all within a finite time-window. The Arctic Ocean is an operational environment where the sea ice and weather conditions determine everything from vessel transit times through to scientific instrument deployment opportunities.

Mission success depends on good team skills, adaptive decision-making abilities, and the timely access to accurate information that improves our situational awareness, including up-to-date information on the sea ice and oceanic conditions, instrument positions, and weather forecasts. However, the seagoing experience of a scientific team varies significantly, as does their ability to gather, transmit, and interpret situational awareness products. Especially the ability to process, plot and interpret heterogeneous data streams, curated data products, such as charts and plots (e.g., sea ice with ship and asset tracks) and data sets delivered in formats that enable integration, analysis, and display both at sea and onshore, offer the most value.

The provision of such products requires advance planning and cooperation by the science team, the logistics provider and other related agencies, as well as ongoing shoreside effort throughout the cruise to ensure timely data delivery to the ship. The rewards are well worth the effort, as we have clearly highlighted by the four very different case studies (navigation, mooring deployment, upper-ocean sampling, and floe selection). Each of these studies utilized products in slightly different ways, but all provided an improved situational awareness. By having this advanced knowledge better evidence-based decisions were made which led to successful scientific and operational outcomes.

Good communication is key to good decisions. During active science deployments, nightly science meetings allowed all science stakeholders to be presented with and discuss the latest information regarding situational awareness received that day. This provided a two-way dialogue whereby all science personnel could then add value to the analysts' interpretation and help guide upcoming site selection and other decisions.

It is important to realize that many situational awareness products have a value beyond the life of a field program. They are invaluable for providing context to field observations at specific time and place. This is particularly true for the Arctic where conditions can change rapidly, and therefore Earth Observation data provides a broader spatial context to point measurements, such as those made from buoys or ship operations. As a result, investment in targeting, acquisition, distribution, and archiving of satellite remote sensing products are critical for efficient use of ship, instrument, and personnel resources, and also to ensure that the data can be analyzed to its full potential. Keeping in mind that the data will be used to make discoveries that, by nature, can't be anticipated, providing information about what is available should be prioritized.

Data acquired during the operational portion of the program continue to be available and discoverable. Full resolution images or additional instruments can be identified and downloaded for specific analyses, for example estimates of sea-ice concentration over various spatial scales around a mooring. The utility of a good situational awareness system extends past the intense operational period.

A challenge particular to the sea ice-based assets, and one that is getting more difficult due to changing ice and atmospheric conditions, is our ability to predict where a given ice-mounted instrument will be to be able to order high-resolution remote sensing products. Such predictions require accurate atmospheric and ice drifts predictions several days ahead. Improving our ability to do this routinely would mean streamlining information exchange between *in situ* instrumentation, real-time assimilation models, satellite data providers, and scientists.

CLOSING WORDS

Improving access to a variety of data streams enhances situational awareness and understanding how to interpret these data is a critical component for all Arctic marine operations. The successful use of a situational awareness system, such as the one described here for Arctic operations is the result of good planning and cooperation between, scientists, logistic providers, and operators. It should be recognized from the beginning that any situational awareness system will not meet every need of every user. It should, however, provide a centralized visualization about what information is available both in real-time and for future analyses. In that context, it should be flexible and as simple as possible, while meeting most operational needs.

The technical and human resources required to put in place and maintain a 24/7 situational awareness system are not negligible. However, this investment should be a priority for every large scientific or logistical marine program. Particularly in the harsh Arctic marine environment, these systems greatly improve safety for operations, ensure knowledge-based decisions are made that benefit both for the scientists and the operators of the vessels, and provide invaluable context for future uses of the data collected. We hope that this manuscript shows how to overcome many of the challenges associated with obtaining timely situational awareness information in remote regions.

DATA AVAILABILITY STATEMENT

The datasets generated for this study can be found in online repositories. The names of the repository/repositories and accession number(s) can be found below: UW Digital Library, http://hdl.handle.net/1773/45592.

AUTHOR CONTRIBUTIONS

LR and JeW: conceptualization and writing – original draft. MEJD: conceptualization and project administration. SH: conceptualization, resources, and project administration. JD and GS: methodology, software, and data curation. MJD: writing – review and Editing. AF: writing – review and editing, software, and data curation. DF: methodology. HG, BM, and JoW: methodology and resources. JTH: writing – review and editing, and data curation. JH and NH: writing – review and editing, and software. BH: conceptualization. MJ and HS: conceptualization and writing – review and editing. CL: writing – review and editing, and supervision. DM, SM, and JT: writing – review and editing, and resources. AS: conceptualization, software, and visualization. All authors contributed to the article and approved the submitted version.

FUNDING

The work presented here was supported by multiple ONR grants, with important additional contributions from the United States Coast Guard, National Oceanic and Atmospheric Administration (NOAA), European Space Agency, as well as multiple other international agencies. In additional, JeW and NH acknowledge the contribution of the EU funded KEPLER programme (Grant Agreement No. 821984).

ACKNOWLEDGMENTS

We would like to acknowledge contributions from all members of the SODA team. We appreciate the expert help from the captains and the crews of USCGC *Healy* and R/V *Sikuliaq*. RADARSAT-2 Data and Products are under a copyright of MDA Geospatial Services Inc. 2018 – All Rights Reserved, obtained via the United States National Ice Center. RADARSAT is an official mark of the Canadian Space Agency. Sentinel-1 data was obtained from the Copernicus Data Hub, supported by the European Space Agency.

REFERENCES

Bliss, A. C., Steele, M., Peng, G., Meyer, W. N., and Dickinson, S. (2019). Regional variability of Arctic sea ice seasonal change climate indicators from a passive microwave climate data record. *Environ. Res. Lett.* 14:045003. doi: 10.1088/1748-9326/aafb84

Comiso, J. C. (2012). Large decadal decline of the Arctic multiyear ice cover. *J. Clim.* 25, 1176-1193. doi: 10.1175/JCLI-D-11-00113.1

Doble, M. J., Wilkinson, J. P., Valcic, L., Robst, J., Tait, A., and Preston, M. (2017). Robust wavebuoys for the marginal ice zone: experiences from a large array in the Beaufort Sea. *Elem. Sci. Anth.* 5:47. doi: 10.1525/elementa.233

Gorelick, N., Hancher, M., Dixon, M., Lyushchenko, S., Thau, D., and Moore, R. (2017). Google Earth Engine: planetary-scale geospatial analysis for everyone. *Remote Sens. Environ.* 202, 18–27. doi: 10.1016/j.rse.2017.06.031

Hwang, B., Aksenov, Y., Blockley, E., Tsamados, M., Brown, T., Landy, J., et al. (2020). Impacts of climate change on Arctic sea ice. *MCCIP Sci. Rev.* 20, 208-217.

Jones, K. L., Martin, R., and Patel, S. (2019). *Closing the Arctic Infrastructure Gap: Existing and Emerging Space-based Solutions*. Technical Report, The Aerospace Corporation, 46. Available online at: https://aerospace.org/sites/default/files/2019-10/Jones_ClosingArcticGap_10172019.pdf.

Kwok, R., Cunningham, G. F., LaBelle-Hamer, N. M., Holt, B., and Rothrock, D. (1999). Ice thickness derived from high-resolution radar imagery EOS. *Trans. Am. Geophys. Union* 80, 495–497. doi: 10.1029/EO080i042p00495-01

Lee, C. M., Starkweather, S., Eicken, H., Timmermans, M. L., Wilkinson, J., and Sandven, S. (2019). A framework for the development, design and implementation of a sustained arctic ocean observing system. *Front. Mar. Sci.* 6:451. doi: 10.3389/fmars.2019.00451

Lee, C. M., Sylvia, C., Martin, D., James, M., Ruth, M., and Tom, P. (2016). *Stratified Ocean Dynamics in the Arctic: Science and Experiment Plan*. Technical Report APL-UW TR 1601. Seattle, WC: Applied Physical Laboratory, University of Washington, 46.

Lee, C. M., Thomson, J., the Marginal Ice Zone, and Arctic Sea State Teams. (2017). An autonomous approach to observing the seasonal ice zone in the western Arctic. *Oceanography* 30, 56–68. doi: 10.5670/oceanog.2017.222

Meier, W. N., Mats, A. G., Sebastian, G., Donald, K. P., Jeffrey, R. K., and Kit, M. K. (2014). Arctic sea ice in transformation: A review of recent observed changes and impacts on biology and human activity. *Rev. Geophys.* 52, 185-217. doi: 10.1002/2013RG000431

Shaw, W. J., Stanton, T. P., McPhee, M. G., and Kikuchi, T. (2008). Estimates of surface roughness length in heterogeneous under-ice boundary layers. *J. Geophys. Res.* 113:C08030. doi: 10.1029/2007JC004550

Smith, G. C., Allard, R., Babin, M., Bertino, L., Chevallier, M., Corlett, G., et al. (2019). Polar ocean observations: a critical gap in the observing system and its effect on environmental predictions from hours to a season. *Front. Mar. Sci.* 6:429. doi: 10.3389/fmars.2019.00429

Spreen, G., Kaleschke, L., and Heygster, G. (2008). Sea ice remote sensing using AMSR-E 89 GHz channels. *J. Geophys. Res.* 113:C02S03. doi: 10.1029/2005JC003384

Spreen, G., Kwok, R., and Menemenlis, D. (2011). Trends in Arctic sea ice drift and role of wind forcing: 1992–2009. *Geophys. Res. Lett.* 38:L19501. doi: 10.1029/2011GL048970

Stroeve, J. C., Kattsov, V., Barrett, A., Serreze, M., Pavlova, T., Holland, M., et al. (2012). Trends in Arctic sea ice extent from CMIP5, CMIP3 and observations. *Geophys. Res. Lett.* 39:L16502. doi: 10.1029/2012GL052676

Strong, C., and Rigo, I. G. (2013). Arctic marginal ice zone trending wider in summer and narrower in winter. *Geophys. Res. Lett.* 40, 4864–4868. doi: 10.1002/grl.50928

Thomson, J. (2012). Wave Breaking Dissipation Observed with “SWIFT” Drifters. *J. Atmos. Ocean. Technol.* 29, 1866–1882. doi: 10.1175/JTECH-D-12-00018.1

Wilkinson, J., and Stroeve, J. (2018). “Polar sea ice as a barometer and driver of change,” in *The Routledge Handbook of the Polar Regions*, eds M. Nuttall, T. R. Christensen, and M. Siegert (Abingdon: Routledge), 176–184.

Conflict of Interest: MJD is employed by Polar Scientific Inc.

The remaining authors declare that the research was conducted in the absence of any commercial or financial relationships that could be construed as a potential conflict of interest.

The reviewer BR declared a past co-authorship with one of the authors, CL, to the handling editor.

Comparing observations and parameterizations of ice-ocean drag through an annual cycle across the Beaufort Sea

Samuel Brenner [1], Luc Rainville [1], Jim Thomson [1], Sylvia Cole [2], Craig Lee [1]

[1]Applied Physics Laboratory, University of Washington, Seattle, WA, USA
[2]Woods Hole Oceanographic Institution, Woods Hole, MA, USA

Key Points:

- In-situ measurements are used to estimate ice-ocean drag across a wide range of ice conditions based on the sea ice momentum balance.
- Ice-ocean drag coefficients show a seasonal cycle with a spring maximum and a fall minimum, following the growth and melt of ice keels.
- Geometry-based drag parameterization schemes are able to capture much of the observed variability using direct ice geometry measurements.

Corresponding author: Samuel Brenner, `sdbren@uw.edu`

Abstract

Understanding and predicting sea ice dynamics and ice-ocean feedback processes requires accurate descriptions of momentum fluxes across the ice-ocean interface. In this study, we present observations from an array of moorings in the Beaufort Sea. Using a force-balance approach, we determine ice-ocean drag coefficient values over an annual cycle and a range of ice conditions. Statistics from high resolution ice draft measurements are used to calculate expected drag coefficient values from morphology-based parameterization schemes. With both approaches, drag coefficient values ranged from approximately 1–10×10^{-3}, with a minimum in fall and a maximum at the end of spring, consistent with previous observations. The parameterizations do a reasonable job of predicting the observed drag values if the under ice geometry is known, and reveal that keel drag is the primary contributor to the total ice-ocean drag coefficient. When translations of bulk model outputs to ice geometry are included in the parameterizations, they overpredict drag on floe edges, leading to the inverted seasonal cycle seen in prior models. Using these results to investigate the efficiency of total momentum flux across the atmosphere-ice-ocean interface suggests an inter-annual trend of increasing coupling between the atmosphere and the ocean.

Plain Language Summary

Sea ice moves in response to the push and pull (a.k.a., ‘drag’) of both wind and ocean currents, so speeds of both the ice and the underlying ocean depends on how efficient that drag is. By looking at measurements of ice motion in response to the wind and ocean currents from three sites in the Beaufort Sea, we have calculated drag efficiency over one year. Computer models predict drag efficiency based on how rough the bottom of the sea ice is. Our measurements of the shape of the sea ice bottom are used to test and verify the framework for calculating drag efficiency that is in place in those models. The model framework can do a reasonable job of prediction if given good measurements of how rough the ice is, but may not be good at predicting that roughness. Because of that, current models might overpredict the drag efficiency while ice is melting. With our measurements of drag efficiency, we calculate how the sea ice impacts the total ability of the wind to push on the ocean and find that it is enhanced by the sea ice. As Arctic sea ice becomes more seasonal, we expect this enhancement to increase.

1 Introduction

Ongoing and dramatic changes in Arctic sea ice (e.g., Stroeve & Notz, 2018) and the underlying ocean (Jackson et al., 2011; Timmermans et al., 2018; Armitage et al., 2020) highlight the need to understand Arctic system feedback processes. Sea ice dynamics are thought to play an important role in both localized (e.g., Ivanov et al., 2016) and large-scale ice-ocean feedbacks (Dewey et al., 2018; Meneghello et al., 2018; Armitage et al., 2020). However, there are still fundamental gaps in our knowledge of the role of sea ice in mediating momentum transfer across the atmosphere-ice-ocean system, especially in understanding spatial and seasonal variability in ice-ocean drag.

Turbulent processes in the ocean and in the atmosphere drive surface momentum flux (a.k.a., stress, $\boldsymbol{\tau}$) across the ice-ocean and ice-atmosphere interfaces. These turbulent fluxes are commonly described by the quadratic drag law:

$$\boldsymbol{\tau} = \rho C \boldsymbol{u} \left| \boldsymbol{u} \right|, \qquad (1)$$

which uses a turbulent transfer coefficient (or drag coefficient), C, to describe the momentum flux, $\boldsymbol{\tau}$, in terms of an appropriate bulk, velocity $\boldsymbol{u}$. Thus, the ice-ocean stress, $\boldsymbol{\tau}_{io}$, and atmosphere-ice stress, $\boldsymbol{\tau}_{ai}$ depend on ice-ocean and atmosphere-ice drag coefficients: C_{io} and C_{ai}, respectively. While there has been considerable work in relating observed values of the atmosphere-ice drag coefficient, C_{ai}, to sea ice properties (Arya, 1975; Guest & Davidson, 1987; Garbrecht et al., 2002; Lüpkes & Birnbaum, 2005; Andreas, Horst, et al., 2010; Andreas, 2011; Lüpkes et al., 2012; Castellani et al., 2014; Elvidge et al., 2016; Petty et al., 2017, and others), there is relatively little analogous work on the ice-ocean drag coefficient, C_{io}. Indeed, despite a wide range of observed values of C_{io} spanning across an order of magnitude (e.g., McPhee, 1980; Morison et al., 1987; McPhee, 2002; Shaw et al., 2008; Randelhoff et al., 2014; Cole et al., 2014, 2017), by default many sea ice models use a constant value for the drag coefficient (e.g., Köberle & Gerdes, 2003; Timmermann et al., 2009; Losch et al., 2010; Rousset et al., 2015; Rampal et al., 2016), such as the "canonical" value of $C_{io} = 5.5 \times 10^{-3}$ determined by McPhee (1980). Moreover, studies show that modelled sea ice thickness is sensitive to the chosen value of C_{io} (J. G. Kim et al., 2006; Hunke, 2010).

Recent observations show both spatial and seasonal variations in the ice-ocean drag coefficient (Cole et al., 2017), suggesting the importance of ice morphology on the values of C_{io} (e.g., due to form drag; Steele et al., 1989; Lu et al., 2011; Tsamados et al., 2014). Model studies that incorporate a variable ice-ocean drag via parameterization of form drag (directly, Tsamados et al., 2014; or indirectly, Steiner, 2001) show first-order impacts both on the sea ice (Castellani et al., 2018) and the underlying ocean (Martin et al., 2016; Castellani et al., 2015, 2018). Although form drag parameterizations of the ice-ocean drag provide a nice theoretical description for the relationship between sea ice morphology and the ice-ocean drag coefficient(Lu et al., 2011; Tsamados et al., 2014), until now there has been no detailed observational study comparing morphological features with observed values of C_{io} across a range of sea ice conditions.

In this study, we present observations made over an annual cycle from an array of moorings in the Beaufort Sea. Using a force-balance approach, mooring measurements and atmospheric re-analysis data are used to infer ice-ocean drag coefficients. Uplooking sonar on the moorings provide snapshots of under-ice topography and statistics related to ice keels and floe edges. Together, these results 1) provide insight into the morphological drivers underlying variations of the ice-ocean drag coefficient, 2) are used for evaluation of model parameterization schemes, and 3) provide context for a broader understanding of momentum transfer into the upper ocean in the changing Arctic. The remainder of this paper is organized as follows: sections 1.1 and 1.2 provide additional background about momentum fluxes across the atmosphere-ice-ocean interface (with focus on the sea ice momentum equation and the total atmosphere-ocean momentum flux). Section 2 provides a review of the geometry-based parameterization schemes developed by Lu et al. (2011) and Tsamados et al. (2014), thus giving important context for interpreting the study results. In section 3 we describe the field study and measurements, along with the force-balance and geometry-based descriptions of the ice-ocean drag coefficient. Descriptions of variations in C_{io}, along with evaluation of the parameterization schemes, and a description of the morphological drivers of ice-ocean drag are presented in section 4. Then, in section 5, these results are placed in the context of previous observations of ice-ocean drag and total momentum flux. The main contributions of the study are summarized in section 6.

Table 1: Notation

a_i	ice covered area	S_c	sheltering function
a_{rdg}	area covered in ridged ice	s_l	attenuation parameter
b_1, b_2, A_*	geometry parameters	$\boldsymbol{u}$	generic bulk velocity
A	ice concentration	$\boldsymbol{u}_*$	friction velocity
c_f	floe-edge drag coefficient of resistance	$\boldsymbol{u}_a$	wind velocity at 10 m
c_k	keel drag coefficient of resistance	$\boldsymbol{u}_i$	ice drift velocity
c_s	skin drag coefficient of resistance	$\boldsymbol{u}_o$	ocean velocity at a reference depth
C	generic drag coefficient	$\boldsymbol{u}_g$	geostrophic ocean velocity
C_f	form drag from floe edges	$\boldsymbol{u}_{rel}$	ice-ocean relative velocity
C_k	form drag from keels	v_{rdg}	volume of ridged ice
C_s	skin drag	z_0	roughness length
C_{ao}	atmosphere-ocean drag coefficient	z_{0i}	level ice bottom roughness length
C_{ai}	atmosphere-ice drag coefficient	z_{0w}	roughness length water
C_{io}	ice-ocean drag coefficient	z_{ref}	reference depth
C_{equiv}	atmosphere-ocean equivalent drag	α_k	keel slope
d_i	ice draft	β	turning angle
d_{lvl}	level ice draft	η	sea surface displacement
f	Coriolis parameter	κ	von Kármán constant (= 0.41)
$\boldsymbol{F}_a$	ice acceleration force	ρ	fluid density
$\boldsymbol{F}_i$	ice interaction force	ρ_a	air density
g	gravitational acceleration	ρ_i	ice density
h_i	ice thickness	ρ_o	ocean density
h_k	keel depth (generic)	$\boldsymbol{\sigma}$	internal ice stress tensor
$h_{k\mathrm{rel}}$	relative keel depth	$\boldsymbol{\tau}$	surface stress
$h_{k\mathrm{tot}}$	total keel depth	$\boldsymbol{\tau}_{ai}$	atmosphere-ice stress
ℓ_f	floe length	$\boldsymbol{\tau}_{ao}$	atmosphere-ocean stress
ℓ_k	keel spacing	$\boldsymbol{\tau}_{io}$	ice-ocean stress
ℓ_l	lead length	$\boldsymbol{\tau}_{oi}$	ocean-ice stress
m_e	effective ice mass per unit area	$\boldsymbol{\tau}_{ocn}$	total ocean stress
m_w	skin drag attenuation parameter	$\boldsymbol{\tau}_{atm}$	total atmosphere stress
P_0	boundary-layer integration function	ϕ_k	keel porosity

1.1 The sea ice momentum equation

The conservation of momentum of sea ice can be written as (e.g., Heorton et al., 2014):

$$m_e \Bigg[\underbrace{\frac{\partial \boldsymbol{u}_i}{\partial t}}_{\text{I}} + \underbrace{\boldsymbol{u}_i \cdot \nabla \boldsymbol{u}_i}_{\text{II}} + \underbrace{f\hat{\boldsymbol{k}} \times \boldsymbol{u}_i}_{\text{III}} \Bigg] = \underbrace{A\boldsymbol{\tau}_{ai}}_{\text{IV}} + \underbrace{A\boldsymbol{\tau}_{oi}}_{\text{V}} + \underbrace{\boldsymbol{\nabla} \cdot \boldsymbol{\sigma}}_{\text{VI}} + \underbrace{m_e g \boldsymbol{\nabla}\eta}_{\text{VII}}, \tag{2}$$

for m_e the "effective" ice mass per unit area, $m_e = A\rho_i h_i$, and other variables as defined in table 1, with ∇ the horizontal gradient operator. This form of the sea ice momentum equation is consistent with that presented by Leppäranta (2011), but modified to ensure consistent scaling for mixed ice-open water conditions (per Hunke & Dukowicz, 2003; Connolley et al., 2004). The terms of the equation are as follows: (I) local ice acceleration; (II) advective ice acceleration; (III) Coriolis acceleration; (IV) stress of the atmosphere acting on the ice; (V) stress of the ocean acting on the ice; (VI) internal stress ("ice-ice" stress); and (VII) gravitational force from sea surface tilt. Advective acceleration (term II) is generally considered negligible and excluded. The final term (VII) in eq. (2) can be expressed in terms of the geostrophic balance $f\hat{\boldsymbol{k}}\times\boldsymbol{u}_g = g\nabla\eta$ and then combined with the Coriolis term, so that term III becomes $f\hat{\boldsymbol{k}}\times(\boldsymbol{u}_i - \boldsymbol{u}_g)$ (Leppäranta, 2011). An additional term representing wave radiation stress in the marginal ice zone has been shown to be locally important at the ice edge (e.g., Perrie & Hu, 1997; Steele et al., 1989; Thomson et al., 2021), but overall is small, so it is neglected. Leppäranta (2011) also includes an atmospheric pressure gradient term which is not included here. In mixed ice-open water conditions, the ocean-ice and atmosphere-ice stresses ($\boldsymbol{\tau}_{ai}$ and $\boldsymbol{\tau}_{oi}$) represent the stress acting only on the ice-covered area and are distinct from the total stress out of the ocean/atmosphere (Hunke & Dukowicz, 2003).

Sea ice is considered to be in "free drift" if the internal ice stress (term VI) is negligible (e.g., McPhee, 1980; Hunke & Dukowicz, 2003; Connolley et al., 2004; Leppäranta, 2011). This is often assumed to be the case if the ratio of ice speed to wind speed ($|\boldsymbol{u}_i|/|\boldsymbol{u}_a|$, the "wind factor") is sufficiently high (typically $\geq$2%; e.g., McPhee, 1980), or if ice concentration is sufficiently low (e.g., $\leq$85%; Hunke & Dukowicz, 2003; Heorton et al., 2019). For freely drifting sea ice, the ice-ocean stress ($\boldsymbol{\tau}_{io} = -\boldsymbol{\tau}_{oi}$) can be expressed as:

$$\boldsymbol{\tau}_{io} = \boldsymbol{\tau}_{ai} - \rho_o d_i \left[\frac{\partial \boldsymbol{u}_i}{\partial t} + f\hat{\boldsymbol{k}} \times (\boldsymbol{u}_i - \boldsymbol{u}_g) \right], \tag{3}$$

where the sea ice mass per unit area $\rho_i h_i$ (for ice density ρ_i and total ice thickness h_i) has been replaced with $\rho_o d_i$ (for ocean density ρ_o and ice draft d_i) assuming hydrostatic balance. McPhee (1980) and Dewey (2019) use this balance, assuming steady-state ($\frac{\partial \boldsymbol{u}_i}{\partial t} = 0$), in order to calculate ice-ocean stress and infer the ice-ocean drag coefficient, while Randelhoff et al. (2014) employ this equation retaining the local acceleration. The ice-ocean stress is also frequently presented in terms of friction velocity, u_*, defined by $\boldsymbol{\tau}_{io} = \rho_o \boldsymbol{u}_* |\boldsymbol{u}_*|$.

1.2 Total momentum flux into the ocean

Using the quadratic drag law (eq. 1), the ice-ocean stress, $\boldsymbol{\tau}_{io}$, and atmosphere-ice stress, $\boldsymbol{\tau}_{ai}$, are written as:

$$\boldsymbol{\tau}_{io} = \rho_o C_{io} \boldsymbol{u}_{rel} \left| \boldsymbol{u}_{rel} \right|, \tag{4a}$$

$$\boldsymbol{\tau}_{ai} = \rho_a C_{ai} \boldsymbol{u}_a \left| \boldsymbol{u}_a \right|, \tag{4b}$$

where the ice-ocean stress uses the relative ice-ocean horizontal velocity, $\boldsymbol{u}_{rel} = \boldsymbol{u}_i - \boldsymbol{u}_o$, as a bulk velocity, while the atmosphere-ice stress uses the wind speed, $\boldsymbol{u}_a$ (for other variable definitions, see table 1). The atmosphere-ice stress is also sometimes written with an atmosphere-ice relative velocity $\boldsymbol{u}_a - \boldsymbol{u}_i$ as the bulk velocity (mirroring the use of relative velocity in the ice-ocean stress), but since typically $\boldsymbol{u}_a \gg \boldsymbol{u}_i$, the ice velocity is frequently neglected from eq. (4b). It is also common to include a rotation matrix in eq. (4a) to account for unresolved Ekman turning in the boundary layer (if the velocity is expressed as a complex exponential, $\boldsymbol{u} = u + iv$, then this is achieved by multiplying eq. 4a by $e^{i\beta}$ for turning angle β). While also occasionally included in eq. (4b), the much greater boundary layer heights in the atmosphere compared to the ocean means that there typically is not unresolved Ekman turning there, so it is not necessary to include an equivalent rotation matrix for calculating the atmosphere-ice stress (note that even with no atmospheric turning, there can still be an offset in wind direction and ice drift direction due to other forces in the sea ice momentum equation, and this offset is also occasionally referred to as a turning angle). Under-ice Ekman layers are not a subject of the present study, so rotation matrix is not included in eq. (4a), but we will accept values of $\boldsymbol{\tau}_{io}$ that are not aligned with $\boldsymbol{u}_{rel}$ that result from the presence of Ekman turning.

In mixed ice and open-water conditions, there is both a direct transfer of momentum between the atmosphere and the ocean, and an indirect transfer mediated by sea ice. It is common to represent these fluxes as combinations of the corresponding atmosphere-ice-ocean stresses weighted by sea ice concentration (e.g., Martin et al., 2014, 2016). Then, the total momentum flux into the ocean, $\boldsymbol{\tau}_{ocn}$, and the total momentum flux out of the atmosphere $\boldsymbol{\tau}_{atm}$ can be represented as:

$$\boldsymbol{\tau}_{ocn} = A\boldsymbol{\tau}_{io} + (1-A)\boldsymbol{\tau}_{ao}, \quad \text{and} \tag{5a}$$

$$\boldsymbol{\tau}_{atm} = A\boldsymbol{\tau}_{ai} + (1-A)\boldsymbol{\tau}_{ao}, \tag{5b}$$

where A is sea ice concentration, and each of the stress components (ice-ocean: $\boldsymbol{\tau}_{io}$; atmosphere-ice: $\boldsymbol{\tau}_{ai}$; atmosphere-ocean: $\boldsymbol{\tau}_{ao}$) is described by the quadratic drag law with corresponding drag coefficients: $\boldsymbol{\tau}_{ao} = \rho_a C_{ao}\boldsymbol{u_a}|\boldsymbol{u_a}|$, and $\boldsymbol{\tau}_{io}$, $\boldsymbol{\tau}_{ai}$ from eqs. (4a) and (4b). As a first approximation, the atmosphere-ocean drag coefficient, C_{ao}, can be described as a function of wind speed (e.g., Large & Yeager, 2004). The atmosphere-ice drag coefficient, C_{ai}, is expected to depend on sea ice geometry in a similar way to the ice-ocean drag (Andreas, 2011; Lüpkes et al., 2012; Tsamados et al., 2014); however, it is sometimes parameterized simply as a function of ice concentration, A (see supporting information Text S2), or taken as a constant (then the equivalent total atmospheric drag coefficient is still a function of ice concentration per eq. 5b; see Elvidge et al., 2016 for additional details and a comparison of atmospheric drag coefficient relationships with sea ice concentration for a variety of models).

Combining eqs. (2), (5a) and (5b) leads to the expression:

$$\boldsymbol{\tau}_{ocn} = \boldsymbol{\tau}_{atm} + \boldsymbol{F}_i + \boldsymbol{F}_a, \tag{6}$$

where $\boldsymbol{F}_i$ is the ice interaction force (derived from the inclusion of term VI in eq. 2), and $\boldsymbol{F}_a$ is the equivalent force from the acceleration and tilt terms (terms I, III, VII in eq. 2; i.e., the term in brackets in eq. 3). Equation (6) mirrors the expression from Martin et al. (2014, their equation 2), except for the inclusion of the equivalent forces from ice acceleration, $\boldsymbol{F}_a$, which they neglect.

In the scenario where the transfer of momentum is an overall flux from the atmosphere into the ocean, this equation can be interpreted to state that all of the momentum flux out of the atmosphere ($\boldsymbol{\tau}_{atm}$) goes into either the ice ($\boldsymbol{F}_i + \boldsymbol{F}_a$), or into the ocean ($\boldsymbol{\tau}_{ocn}$). Although, because of the vector summation in eq. (6), both of $\boldsymbol{F}_i$ and $\boldsymbol{F}_a$ can either enhance or subtract from $\boldsymbol{\tau}_{atm}$. Ice interaction is usually thought as a momentum sink that opposes $\boldsymbol{\tau}_{atm}$ (Steele et al., 1997; Martin et al., 2014), but ice acceleration terms could potentially be an additional source of ocean momentum.

To examine the effect of sea ice in mediating the total momentum flux from the atmosphere to the ocean, consider an "equivalent drag coefficient", C_{equiv}, based on the construction of a quadratic drag law between the wind speed and the total ocean stress; i.e.,

$$C_{equiv} = \frac{|\boldsymbol{\tau}_{ocn}|}{\rho_a |\boldsymbol{u}_a|^2}. \tag{7}$$

C_{equiv} does not have a clean analytic form, nor is it a useful prognostic variable: its value will depend on $\boldsymbol{u}_i$ and $\boldsymbol{u}_o$, which are themselves functions of the total atmosphere-ice-ocean momentum transfer. Instead, C_{equiv} is a diagnostic of momentum transfer efficiency, where higher values indicate that a greater proportion of atmospheric momentum is ultimately transferred to the ocean. This is similar to the use of a normalized effective stress in Martin et al. (2014, 2016).

2 Drag from geometry-based parameterizations

This study compares estimates of the observed ice-ocean drag to two schemes that parameterize the ice-ocean drag as a function of the observable ice geometry. Both Lu et al. (2011) and Tsamados et al. (2014) present similar ice geometry-based parameterizations of the ice-ocean drag coefficient based on a combination of skin and form drag components, with the scheme by Tsamados et al. (2014) available in the CICE sea ice model (Hunke et al., 2020). Steiner (2001) presents an alternative scheme using a "deformation energy" approach. That method has been used in the sea ice component of the MITgcm model (Losch et al., 2010) to investigate the impact of variable ice-ocean drag (Castellani et al., 2018); however, we cannot track deformation energy with our measurements, so the deformation energy scheme is not considered here. Strictly, ice geometry-based parameterizations in the forms presented below only model the neutral ice-ocean drag coefficients and do not account for the impacts of stabilizing or destabilizing buoyancy fluxes. Buoyancy fluxes modify the total drag, and are included in atmospheric models as correction term to the neutral drag coefficient, based on Monin-Obukhov similarity theory (Monin & Obukhov, 1954)(which could be included in sea ice models using a parameterization by Lüpkes & Gryanik, 2015). We are unable to account for stability effects in the present study, which may modify some interpretations of the results.

2.1 Details of parameterization schemes

Ice-geometry based parameterizations of the ice-ocean drag coefficient write the total drag as a sum of form drag from floe edges, form drag from keels, and skin drag (Lu et al., 2011; Tsamados et al., 2014):

$$C_{io} = C_f + C_k + C_s. \tag{8}$$

For both schemes, these three drag components can be written as:

$$\begin{aligned}
\text{floe edge drag:} \qquad C_f &= \frac{1}{2} c_f A \frac{d_{lvl}}{\ell_f} \left[S_c \left(\frac{d_{lvl}}{\ell_l} \right) \right]^2 P_0(d_{lvl}, z_{0w}), && \text{(9a)} \\
\text{keel drag:} \qquad C_k &= \frac{1}{2} c_k A \frac{h_k}{\ell_k} \left[S_c \left(\frac{h_k}{\ell_k} \right) \right]^2 P_0(h_k, z_{0i}), && \text{(9b)} \\
\text{skin drag:} \qquad C_s &= c_s A \left(1 - m_w \frac{h_k}{\ell_k} \right), \quad \text{if } \frac{h_k}{\ell_k} \leq \frac{1}{m_w} && \text{(9c)}
\end{aligned}$$

with variables defined in table 1. So the ice geometry appears in the parameterizations as the floe "aspect ratio", d_{lvl}/ℓ_f, and the "ridging intensity", h_k/ℓ_k. The scheme by Tsamados et al. (2014) is an adaptation of an atmospheric drag parameterization by Lüpkes et al. (2012). Note that in Tsamados et al. (2014), the inequality in the valid range for the skin drag, C_s ($h_k/\ell_k \leq 1/m_w$), is mistakenly reversed (compare their equation 19 with the work of Arya, 1975 on which skin drag is based); eq. (9c) presents the correct inequality for both of the parameterization schemes.

The two schemes are functionally similar. The differences between them are due to the following factors: (1) different values of the coefficients of resistance, c_f, c_k, and c_s (which account for the drag on individual elements); (2) different forms of the "sheltering functions" S_c; and (3) the inclusion (or not) of the functions P_0 (which are included in the Tsamados et al., 2014 scheme but not in the Lu et al., 2011 scheme). Additionally, the two schemes use slightly different definitions for keel depth (relative versus total; see fig. 1).

The sheltering function S_c accounts for the reduction in drag of downstream obstacles due to the wake effect of upstream obstacles (Steele et al., 1989). Both parameterization schemes employ different, empirically-derived, sheltering functions:

$$\begin{aligned}
\text{Tsamados et al. (2014):} \qquad S_c(x) &= \left[1 - \exp\left(-\frac{s_l}{x} \right) \right]^{1/2} && \text{(10a)} \\
\text{Lu et al. (2011):} \qquad S_c(x) &= \left[1 - (x)^{1/2} \right] && \text{(10b)}
\end{aligned}$$

For keel sheltering, the input argument, x, is the the ridging intensity, h_k/ℓ_k, which mirrors its other use eq. (9b). For floe sheltering, the argument for the sheltering function is d_{lvl}/ℓ_l (the denominator is the distance between floes), instead of the aspect ratio d_{lvl}/ℓ_f that appears earlier in eq. (9a).

Tsamados et al. (2014) include a term in C_f and C_k which arises due to integration of a depth-varying velocity profile over the height of an obstacle, here called P_0 (it differs from the definition of P_0 in Lüpkes et al., 2012). In the atmospheric drag parameterization, Lüpkes et al. (2012) assume a "law-of-the-wall" velocity profile: $u(z) = (u_*/\kappa)\ln(z/z_0)$, which Tsamados et al. (2014) maintains in adapting the scheme to the ice-ocean boundary layer. This gives

$$P_0(h, z_0) = \left[\frac{\ln(h/z_0)}{\ln(z_{\mathrm{ref}}/z_0)}\right]^2, \tag{11}$$

where the input variable h is either the level ice draft, d_{lvl} or keel depth, h_k for floe edge drag or keel drag, respectively, and an appropriate choice of roughness length is used (see eqs. 9a, 9b). Inclusion of P_0 allows the ice-ocean drag coefficient to be an explicit function of the reference depth z_{ref}. The form of P_0 depends on the assumed law-of-the-wall boundary-layer structure, which is suitable for the atmosphere where the height of logarithmic boundary layer typically much greater than the reference height z_{ref} (e.g., Holton, 2004, chapter 5). However, it is not clear that this is appropriate in the ice-ocean boundary layer. The P_0 functions are not included in the scheme by Lu et al. (2011).

The coefficient of resistance, c_s used in the skin drag parameterization (C_s, eq. 9c) represents the baseline skin drag associated with level ice in the absence of ridges. Both Tsamados et al. (2014) and Lu et al. (2011) treat this term as a free parameter. Keeping with the law-of-the-wall velocity assumption used to develop P_0, the baseline skin drag could instead be represented by

$$c_s = \left[\frac{\kappa}{\ln(z_{\mathrm{ref}}/z_{0i})}\right]^2, \tag{12}$$

where the von Kármán constant $\kappa = 0.41$. This reduces the number of free parameters in the model, and allowing c_s to be an explicit function of the reference depth z_{ref}. As with P_0, the actual form will depend strongly on boundary layer structure.

In applying their parameterization scheme (eqs. 9, 10a, and 11), Tsamados et al. (2014) use total keel depth, $h_{k\mathrm{tot}}$, which is measured from the waterline (fig. 1) as the definition of h_k. However, in full ice cover, it should be the keel depth relative to the level ice draft, $h_{k\mathrm{rel}}$, that contributes to form drag (as in Lu et al., 2011) (note: $h_{k\mathrm{tot}} = h_{k\mathrm{rel}} + d_{lvl}$). Similarly, the reference depth z_{ref} in eqs. (11) and (12) should also be relative to

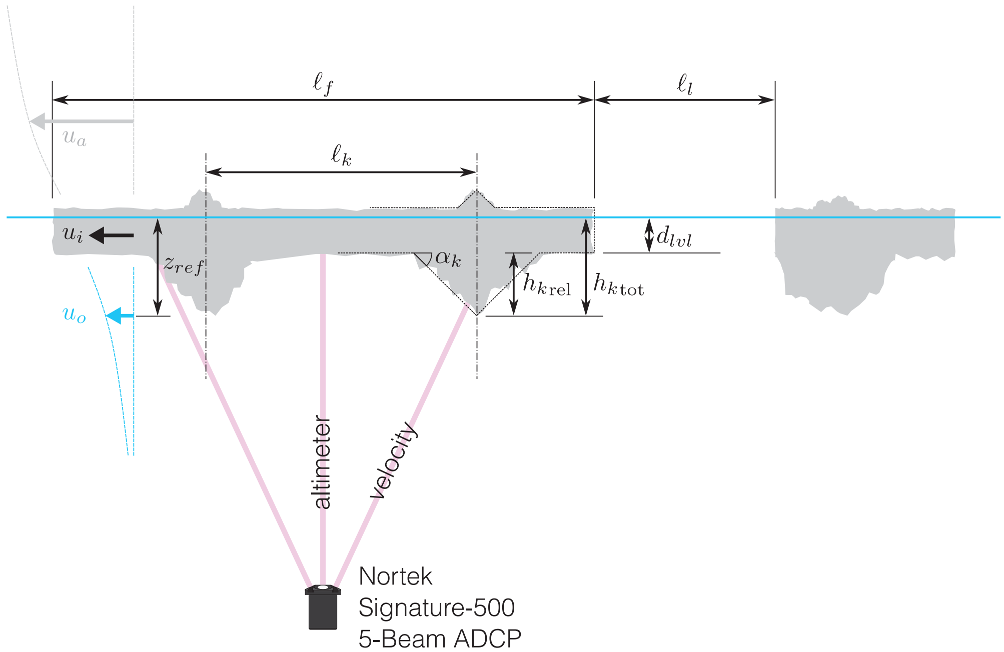

Figure 1: Schematic representation of an ice floe showing sea ice geometry with idealized triangular representation of ice keels, and the in-situ ADCP measurements. Dimension labels of ice geometry correspond to table 1.

the level ice draft (e.g., $z_{\mathrm{ref}}-d_{lvl}$), because that is the range over which the boundary layer develops. In mixed ice-open water conditions, the use of $h_{k\mathrm{rel}}$ is still consistent with the parameterization scheme as floe-edge drag (eq. 9a) is accounted for separately.

2.2 Translating model outputs to ice geometry

The details of sea ice geometry necessary for calculating the ice-ocean drag coefficient with eq. (9) are not generally resolved by models, which do not simulate individual ice floes or keels. Tsamados et al. (2014) developed a scheme for estimating average keel properties based on outputs in the CICE model using assumptions about the keel geometry that are guided by observations (see their supplementary information). Namely, the scheme uses area extent and volume of ridged ice in a model grid cell (a_{rdg} and v_{rdg}, respectively), along with the ice area in a grid cell (a_i, which is the ice concentration A multiplied by the grid-cell area).

For subsurface measurements (as presented below), keel depth and keel spacing are given by taking the limit as $R_h \to \infty$ in equations 24 and 25 from Tsamados et al. (2014) (where R_h is the ratio of keel depth to sail height, so the limit states that all ridged ice in the measurements is attributed to keels). This gives the expressions:

$$h_k = 2\frac{v_{rdg}}{a_{rdg}}\frac{b_1}{\phi_k}, \tag{13a}$$

$$\ell_k = 2h_k\frac{a_i}{a_{rdg}}\frac{b_1}{\tan(\alpha_k)}, \tag{13b}$$

where b_1 is a weight function accounting for the overlap of keels with level ice (taken as 0.75), ϕ_k is the keel porosity (taken as 1), and α_k is the keel slope (see fig. 1).

The floe and lead lengths (ℓ_f, ℓ_l) used in eq. (9a) are also parameterized. Using measurements derived from aerial photographs of the marginal ice zone of Fram Strait, Lüpkes et al. (2012) developed an empirical model for estimating floe size based on ice concentration:

$$\ell_f = \ell_{f,min}\left(\frac{A_*}{A_* - A}\right)^{b_2}, \tag{14}$$

with b_2 a tunable parameter (ranging from 0.3 to 1.4), and A_* a value calculated such that the limits of ℓ_f range from $\ell_{f,min}$ to $\ell_{f,max}$ (for $A \to 0, 1$), the minimum and maximum floe lengths, respectively (see eq. 27 in Lüpkes et al., 2012). Using default parameters, this gives average floe lengths that are limited to range from a minimum of 8 m to a maximum of 300 m. Tsamados et al. (2014) implement this floe size model in their parameterization scheme, though they acknowledge that observations have shown that floe size follows a power-law distribution with a much wider range of scales than is possible with that scheme (e.g., Weiss & Marsan, 2004; see also Stern, Schweiger, Zhang, & Steele, 2018 and references therein). They further acknowledge that this scheme may breakdown in the winter when ice concentration is near 100%, given that the parameterization was developed for the marginal ice zone; but it is employed through the full year nonetheless.

3 Drag from field measurements

3.1 Field measurements

Data were collected during the Stratified Ocean Dynamics of the Arctic (SODA) experiment: an Office of Naval Research (ONR) project to better understand the controls of heat and momentum transfer in the Arctic's upper ocean. A program compo-

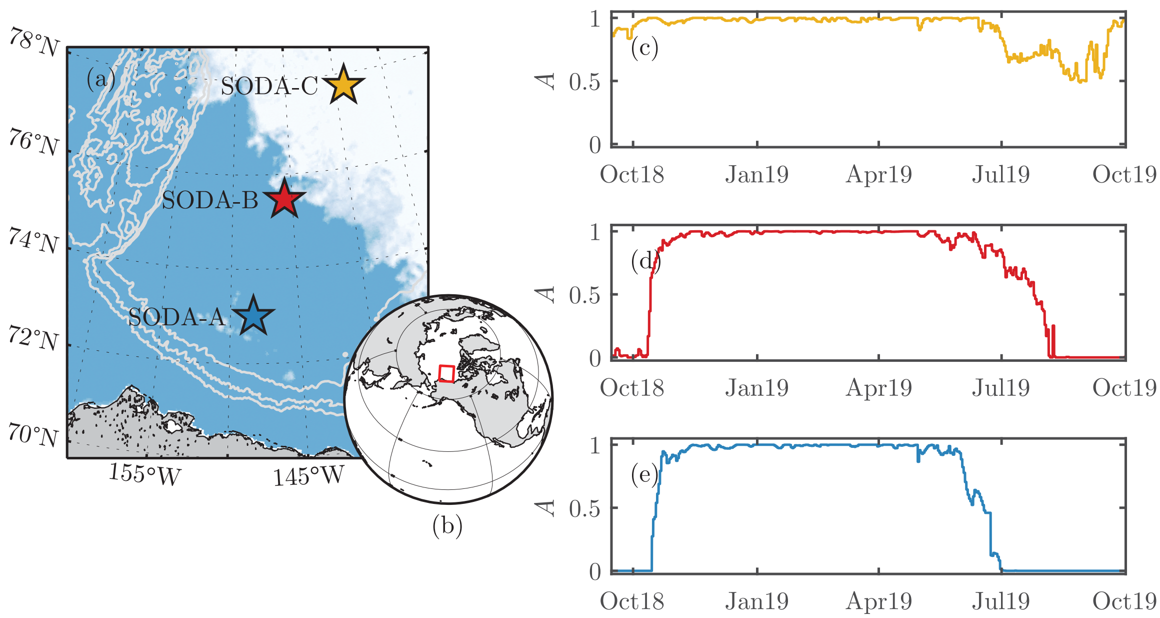

Figure 2: (a,b) Maps of (a) the Beaufort Sea showing the locations of the three moorings overlaid on sea ice concentration map from Sept. 18, 2018 (the 2018 sea ice minimum), with baythymetry shown by grey contours (contours are 1000-m isobaths); and (b) the location of (a). The ice concentration in (a) is from the Sea Ice Remote Sensing database at the University of Bremen (Spreen et al., 2008). (c–e) The annual cycle of sea ice concentration averaged over the mooring locations during the measurement period: (c) SODA-C, (d) SODA-B, and (e) SODA-A.

nent included the installation of three subsurface moorings in a line stretching from the south to the north of the Beaufort Sea, which are designated as SODA-A, SODA-B, and SODA-C (figs. 2a and 2b). The moorings recorded a full annual cycle of sea ice growth and melt from their installation in fall 2018 to their recovery in fall 2019. The spatial distribution of the moorings allowed for sampling of different ice regimes: the southernmost mooring (SODA-A) was in the seasonal ice zone and experienced prolonged open-water periods in summer (fig. 2e); SODA-B was near the edge of the seasonal ice zone and has a minimal open-water period but a longer period of time in marginal ice (fig. 2d); whereas SODA-C was still ice-covered all year long (fig. 2c; the mooring at that location was both deployed and recovered through the ice).

This study utilizes measurements made with uplooking Nortek Signature-500 5-beam acoustic Doppler current profilers (ADCPs) installed on the top float of each mooring (fig. 1). The instrument depths were approximately 45 m for SODA-A, 42 m for SODA-B, and 27 m for SODA-C. To minimize the effects of mooring knock-down, the top float of each mooring was a DeepWater Buoyancy Stablemoor500, which are designed to remain level even during knockdown events (Harding et al., 2017). The maximum tilt deviation measured by any of the ADCPs was $\leq 2°$ from their resting position. A Seabird SBE-37 conductivity-temperature-depth sensor installed underneath the float ($\sim$1 m vertical offset from the ADCP) collected temperature and salinity measurements to compliment the temperature measurements made by the ADCP to calculate and correct the speed of sound (which is used to calculate altimeter distance).

The four slant beams of the ADCP measured velocity profiles, while the fifth vertical beam acted as an altimeter (fig. 1) and measured the distance to the surface (either the water surface or ice bottom). The vertical beam has a beam width of 2.9°, so for the deployment depths here, the width of the ensonified area was roughly 2.3 m for SODA-A, 2.1 m for SODA-B, and 1.4 m for SODA-C. The ADCPs operated with two concurrent sampling plans: "Average+Ice", and "Burst+Waves". For both modes, the ice draft was derived from the difference between the water depth (determined by instrument pressure) and altimeter distance, after making corrections for ADCP tilt, speed of sound, and atmospheric pressure variations (e.g., Magnell et al., 2010; Krishfield et al., 2014).

During the Average+Ice sampling mode, the ADCP measured altimeter distance, water column velocity, and ice drift velocity. Ice drift velocities were measured using the instrument's built-in ice-tracking mode, which functions similarly to traditional ADCP "bottom-tracking": a ping is emitted separate to the water velocity-measuring pings with longer pulse-length that fully ensonifies the ice area for the full beam width and provides velocity measurements that are typically more accurate than in the water column (e.g., Belliveau et al., 1989). Measurements of each of the variables were provided every 10 min based on raw data collected in 1-min long ensembles at a sampling rate of 1 Hz (reported measurements are ensemble-medians after quality control processing of the raw data). The water velocities were measured in 2-m vertical range bins. Due to sidelobe interference, the upper $\sim 10\%$ of each vertical velocity profile (2.7 m to 4.5 m) was discarded, so near-ice logarithmic boundary layers could not be directly observed. At each time step the velocity profiles were interpolated to find the horizontal velocity, $\boldsymbol{u}_o$, at a fixed reference depth, z_{ref}; here, $z_{ref} = 10\,\text{m}$ to conform to the Tsamados et al. (2014) parameterization scheme. The 10-min sampled Average+Ice measurements of $\boldsymbol{u}_i$, $\boldsymbol{u}_o$, and d_i were bin-averaged in 1-h bins to match the atmospheric re-analysis measurements used (see below). The supporting information fig. S1 shows examples of the timeseries of each of the velocity components at SODA-B.

As indicated by its name, the Burst+Waves plan is designed for the measurement of surface gravity waves using altimeter measurements from the vertical beam. However, those altimeter measurements can also be used for measuring under-ice geometry (e.g., ice keels; Magnell et al., 2010). In Burst+Waves mode, the ADCPs measured "bursts" of data containing 2048 samples at a rate of 2 Hz, so each burst length was 1024 s (~ 17 min). These bursts were collected once every two hours. Because the Burst+Waves and Average+Ice measurement plans were concurrent, the ADCPs recorded two values of the ice drift speed during each burst. Using the mean of those two ice drift measurements, the sampling time for each burst was converted to an along-burst distance. Within each burst, ice draft data were despiked using a moving-median outlier criteria in 127-point windows (outliers are identified as points more than three scaled median absolute deviations from the median, and replaced with linearly interpolated values). Then, the ice draft from Burst+Waves sampling were used to characterize the ice geometry (see section 3.3).

We used atmospheric forcing from the European Center for Medium-Range Weather Forecasts (ECMWF) Reanalysis version 5 (ERA5; Hersbach et al., 2020). ERA5 provides hourly measurements at a $0.25^\circ \times 0.25^\circ$ grid resolution. A recent comparison with in situ measurements in the Eastern Arctic showed that of the six re-analysis products assessed, ERA5 provided the best representation of wind speed (which is the primary variable of interest here) during winter and spring, and second best (by a small margin) during summer (Graham et al., 2019). To generate a timeseries of atmospheric forcing at each mooring, grid points were averaged within a 30 km radius centred at each of the mooring locations (14–16 gridpoints per mooring). There is a degree of uncertainty in re-analysis wind measurements in the Arctic (particularly in the marginal ice zone; e.g., Brenner et al., 2020). Nonetheless, there is strong coherence between the re-analysis wind velocities and the in situ measured ice drift velocities (not shown) and associated high correlations between the two (correlation coefficients of $r = 0.69$, 0.75, and 0.63 for SODA-

A, -B, and -C, respectively). To test sensitivity, wind velocities at the mooring locations were also found using two alternative re-analysis products: Modern-Era Retrospective analysis for Research and Applications version 2 (MERRA-2; Gelaro et al., 2017) and Japanese 55-year Reanalysis (JRA-55; Kobayashi et al., 2015, which is on a slightly coarser grid in both space and time). Across these different products, wind velocities at the mooring locations were very similar; MERRA-2 wind velocities were correlated with ERA5 winds with $r = 0.97$ across all three moorings, and JRA-55 were correlated with ERA5 with $r = 0.96$ (after subsetting ERA5 to the same timestamps). Resulting drag coefficient measurements (calculated per section 3.2) were correlated with $r = 0.94$ between MERRA-2 and ERA5, and $r = 0.84$ between JRA-55 and ERA5. Thus, the results presented in this study are not overly sensitive to the choice of re-analysis product used.

3.2 Application of the force-balance approach

Following McPhee (1980; see also Randelhoff et al., 2014; Dewey, 2019), we use a force-balance approach (eq. 3) to calculate the ice-ocean stress, $\boldsymbol{\tau}_{io}$. Then the ice-ocean drag coefficient, C_{io}, is inferred from the quadratic drag law (eq. 4a).

The ice-ocean stress ($\boldsymbol{\tau}_{io}$) is calculated hourly with eq. (3) using data from the ADCP measurements and ERA5 re-analysis. The ice draft (d_i) and ice velocity ($\boldsymbol{u}_i$) are from the 1-hour-averaged ADCP measurements. The local acceleration ($\frac{\partial \boldsymbol{u}_i}{\partial t}$) is the numerical derivative of the 1-hour-averaged $\boldsymbol{u}_i$ values. The geostrophic velocity ($\boldsymbol{u}_g$) is estimated as the depth-averaged velocity between 5 m and 20 m (based on results by Armitage et al., 2017), and low-pass filtered with a 2-day cutoff (the result is insensitive to these choices for $\boldsymbol{u}_g$; see supplementary Text S1). The atmosphere-ice stress ($\boldsymbol{\tau}_{ai}$) is determined using the quadratic drag law (eq. 4b), with 10-m wind velocity and surface air density taken from ERA5 re-analysis and C_{ai} parameterized as a function of ice concentration (following ECMWF, 2019; see supporting information Text S2). In mixed ice-open water conditions, the atmosphere-ice stress, $\boldsymbol{\tau}_{ai}$, used in eq. (3) is distinct from the total atmospheric stress (eq. 5b). Because eq. (3) assumes that ice is in free drift, values for which the wind factor ($|\boldsymbol{u}_i|/|\boldsymbol{u}_a|$; determined hourly) was less than 2% were rejected (the so-called "2%-rule"). The use of wind factor as a filtering criteria implies an intermittency of internal ice stresses, which is consistent with Steele et al. (1997), who found that on short timescales the atmospheric stress input to the ice ($\boldsymbol{\tau}_{ai}$) was primarily balanced by only one of either the ocean-ice stress ($\boldsymbol{\tau}_{oi}$) or the internal ice stress. ($\nabla \cdot \boldsymbol{\sigma}$). The friction velocity ($\boldsymbol{u}_*$) is determined from $\boldsymbol{\tau}_{io}$ assuming a constant $\rho_o = 1025\,\mathrm{kg\,m^{-3}}$ (with the definition $\boldsymbol{\tau}_{io} = \rho_o \boldsymbol{u}_* |\boldsymbol{u}_*|$).

To calculate the ice-ocean drag coefficient, the record is split into windows. Within each window the quadratic drag law (eq. 4a) is applied by regressing hourly calculated values of $|\boldsymbol{u}_*|^2$ (as described above) with hourly measured $|\boldsymbol{u}_{rel}|^2$ (with $\boldsymbol{u}_o$ defined at a 10-m reference depth). Then the value of C_{io} is the slope of the regression line (fig. 3). Windows are chosen to be 7 days in length, which provides an average of 80 points in each window (after using the 2%-rule to exclude non-free-drift points). Based on average ice drift speeds, each window covers roughly 75 km of ice (though there is both spatial and temporal variability in the actual window size). While shorter window lengths can resolve some higher frequency variability at the expense of larger uncertainties, the overall seasonal patterns found here are not sensitive to the window length chosen. Regression is performed with a bisquare robust linear fitting algorithm and forced through the origin (Huber, 1981). This method iteratively reduces the weighting on outliers, which may occur, for example, from intermittent violation of the free-drift assumption. Performing regression within windows instead of calculating C_{io} on a point-by-point basis (as in Dewey, 2019) minimizes the effects of noise and uncertainty (particularly for low values of $\boldsymbol{u}_{rel}$), which may have resulted from a combination of measurement noise, higher frequency temporal variations, or unaccounted stresses (e.g., internal ice stress). Calculated values of the drag coefficient were rejected if the uncertainty in C_{io} was $\geq 2.5 \times 10^{-3}$ (based on a t-test with 95% confidence interval; Bendat & Piersol, 1971). High uncertainties in C_{io} occurred most frequently in winter when many of the data were rejected due to free drift conditions not being met. Tests using non-linear fits of the form $|\boldsymbol{\tau}_{io}| \propto |\boldsymbol{u}_{rel}|^n$ (see section 5.1) did not produce better fits than the quadratic drag law with $n = 2$ (r^2 values from $n \neq 2$ fits were approximately equal to those with $n = 2$). Given the direct concurrent and collocated measurements of the ice and ocean velocities here, it is not necessary to exclude periods of small ice-ocean relative velocity, a condition often necessary when using satellite remote sensing to estimate ocean velocities (e.g., in McPhee, 1980).

This method of drag calculation essentially asks what value of C_{io} would be required to reproduce the observed sea ice motion. In doing so, the method effectively integrates over both the temporal intermittency and the spatial heterogeneity of turbulent momentum fluxes across ice floes and thus provides bulk-average drag coefficient values. These

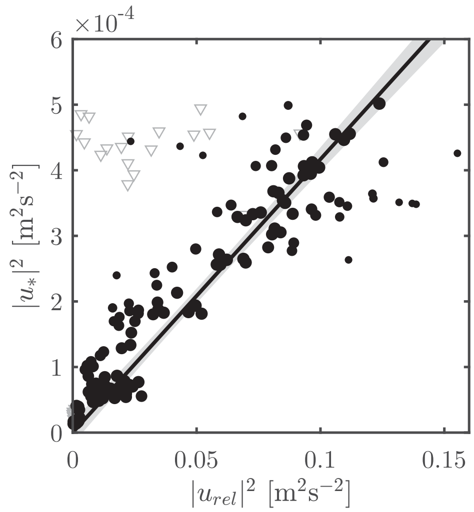

Figure 3: Example of quadratic-drag-law fit between hourly values of observed relative velocity ($|\boldsymbol{u}_{rel}|^2 = |\boldsymbol{u}_i - \boldsymbol{u}_o|^2$), and calculated friction velocity ($|\boldsymbol{u}_*|^2 = |\boldsymbol{\tau}_{io}|/\rho_o$) from the force-balance approach (eq. 3). Black points show values used in the fitting procedure, with point sizes an indicator of the relative weighting determined by the robust fitting method. Grey triangles show points rejected from the fit by the 2%-rule and demonstrate the utility of the wind factor to filter points that are not in free drift. The black line shows the regression line with 95% confidence interval shaded in grey. Data correspond to 1 week of measurements in November 2018 at SODA-A.

resulting drag coefficients are appropriate for comparison to model parameterizations as the goal of those parameterizations is to provide a bulk coefficient for use within a model grid cell.

There is no physical basis to expect that the relationship between total ocean stress, $\boldsymbol{\tau}_{ocn}$, and wind speed should follow the quadratic drag law, so the linear fitting procedure used to calculate C_{io} cannot be similarly applied to find C_{equiv}. Instead, C_{equiv} is computed on a point-by-point (hourly) basis using eq. (7), with $\boldsymbol{\tau}_{ocn}$ given by eq. (5a) and with A from ERA5. For points defined as being in free-drift (based on the 2%-rule), the ice-ocean stress, $\boldsymbol{\tau}_{io}$ used in eq. (5a) is the same as described above (eq. 3). The analysis was extended beyond free-drift periods by calculating $\boldsymbol{\tau}_{io}$ for those times using eq. (4a) and values of C_{io} from the regression procedure, interpolated to points with a wind factor $< 2\%$.

3.3 Ice geometry

During periods of ice cover, the ADCP Burst+Waves sampling provides one dimensional (along-drift) tracking of the under-ice geometry (fig. 4a). We use these to quantify the geometric characteristics used in the parameterization schemes in section 2. Importantly, the fixed mooring platforms allow for sampling across a broad range of different ice conditions as they evolve over the annual cycle.

Spectral analysis is used as part of a filtering criteria to separate ice-covered conditions from open water conditions; this ensures that surface gravity waves are not erroneously misidentified as ice keels. For each burst, frequency spectra of measured altimeter distances are constructed. Surface gravity waves have distinct and well known spectral shapes (e.g., Phillips, 1985), with peaks at relatively high frequencies ($\gtrsim$0.04 Hz), while sea ice has broadly distributed spectral energy with energy concentrated at lower horizontal wavenumbers (which translate to low frequencies) (e.g., McPhee & Kantha, 1989). Following Shcherbina et al. (2016) and Kirillov et al. (2020), ice-covered conditions are identified using the ratio of integrated spectral energy in low- and high-frequency bands (using a cutoff frequency of 0.1 Hz, based on observed conditions): burst are deemed to be ice-covered when the ratio of high-to-low frequency spectral energy is less than 5. Then, bursts identified as being open-water but with measured non-zero level ice draft, d_{lvl}, provide a secondary empirical correction to ice draft measurements to account for water-column sound-speed variations (e.g., due to shallow stratification; Kirillov et al., 2020). These corrections were small, and primarily applied to marginal ice covered periods.

For each ice-covered burst we quantify the draft of level ice, the extent and number of leads, and the number and size of keels (fig. 4b). Prior to classification, bursts are smoothed with a moving-average filter using a centered window with a width of 2 m (because of variability in ice drift speed, the number of points in each window varies from burst to burst). Bursts frequently contained apparent leads, identified as all points in a burst with a measured draft below a tolerance level (taken as 0.15 m to account for instrument noise and uncertainty associated with both atmospheric pressure variations and

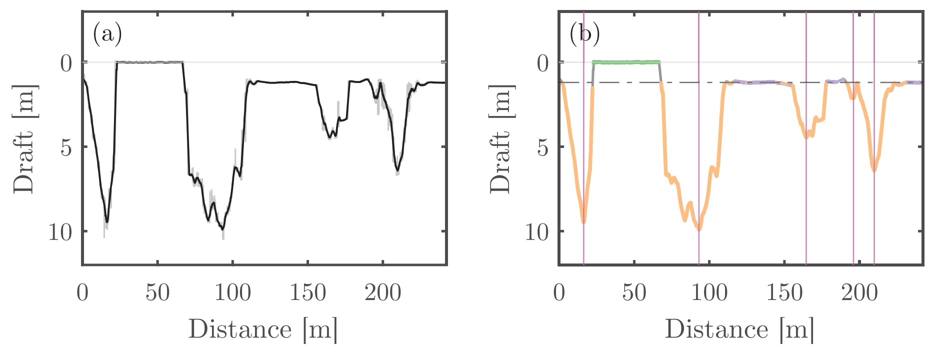

Figure 4: Example of ice draft from burst measurements: (a) Raw (thin grey line) and smoothed (black line) ice draft during a single burst (∼17 min) in April 2019 at SODA-A. (b) The burst from (a) classified to show leads (green line), level ice (purple), and ridged ice (orange), with vertical magenta lines showing unique keels (based on Rayleigh criterion), and black dashed-dotted line showing the level ice draft classified for that burst.

sound speed). Strictly, this procedure is unable to differentiate between open-water leads and refrozen leads containing thin ice, but from the perspective of the drag parameterizations (section 2), both scenarios are dynamically equivalent in that they both contribute to the floe edge form drag. Within each burst, level ice is defined by a local gradient less than 0.025 (equivalent to the process in Wadhams & Horne, 1980) and a draft of less than 3 m (roughly the limit of thermodynamic growth; Maykut & Untersteiner, 1971). The level ice draft for each burst is then taken as the median draft of all ice identified as level within the burst. In cases where no level ice was identified (i.e., the entire burst measured ridged ice), the level ice draft is found by interpolating across adjacent bursts. Keels identification follows Martin (2007), using a Rayleigh criterion to define unique keels (see also Williams et al., 1975; Wadhams & Horne, 1980; Wadhams & Davy, 1986) with a minimum keel depth cutoff of 0.5 m relative to the level ice draft for that burst. Relative keel depths at each of the moorings closely followed exponential probability distributions (not shown), which is in line with previous literature (e.g., Wadhams & Horne, 1980; Wadhams & Davy, 1986), and a total of 14 694 individual keels are identified throughout the full study period (6282, 4305, and 4107 at SODA-A, -B, and -C, respectively). The maximum relative keel depth measured at any of the moorings through the full deployment was 11.4 m at SODA-B. Keel sizes across the three moorings were fairly similar.

The parameterized ice-ocean drag is based on statistical descriptions of the ice geometry (see section 2). Statistics are accumulated over one-week periods to be consistent with the windowing procedure for the ice-ocean drag (section 3.2). The keel depth (h_k) and level ice draft (d_{lvl}) are simply averages of individual measurements taken for all bursts in each window. The average keel spacing (ℓ_k) is taken as the total distance measured by all bursts in a given window (both ice and open water) divided by the total number of keels counted during that window. Except for some bursts in the marginal ice zone, floe lengths are typically longer than the distance measured by an individual burst. To estimate an average floe length (ℓ_f) the total measured ice-covered distance for a given window is divided by the number of leads counted in that window. Similarly, the average lead length (ℓ_l) was the total open water distance divided by the number of leads. These definitions for ℓ_k and ℓ_f are consistent with their inclusion in parameterizations (Lu et al., 2011; Tsamados et al., 2014). A local average daily ice concentration, (A) was also calculated using burst data as a ratio of the total measured ice-covered distance to the total distance measured by all bursts (ice and open water). Using A, the average lead length can be written as $\ell_l = \ell_f(1 - A)/A$ for one-dimensional measurements (Lu et al., 2011). The values ℓ_f and ℓ_l are only defined for ice concentration less than 100%. The measurements show seasonal signals in all of the measured geometry statistics at all moorings (fig. 5). Despite both d_{lvl} and ℓ_f decreasing in the summer/fall (figs. 5a and 5c), the much wider range of variation of ℓ_f (over roughly 3 order of magnitude) compared to d_{lvl} results in floe aspect ratios (d_{lvl}/ℓ_f) that are elevated in the fall (fig. 5e). The relative keel depths and spacing ($h_{k\mathrm{rel}}$ and ℓ_k) appear to have some negative correlation (cf., figs. 5b and 5d), so that both signals contribute to the minimum ridging intensity (h_k/ℓ_k) in the summer/fall (fig. 5f).

3.4 Implementing model parameterization schemes

Four different variations of ice-ocean drag parameterizations were tested. These are summarized in table 2. In the first two variations (labelled L11 and T14(I), respectively), direct measurements of the sea ice geometry (section 3.3) were used to test the parameterization schemes proposed by Lu et al. (2011) and Tsamados et al. (2014) (section 2.1) using default parameter values in each scheme. We introduce an alternative version of

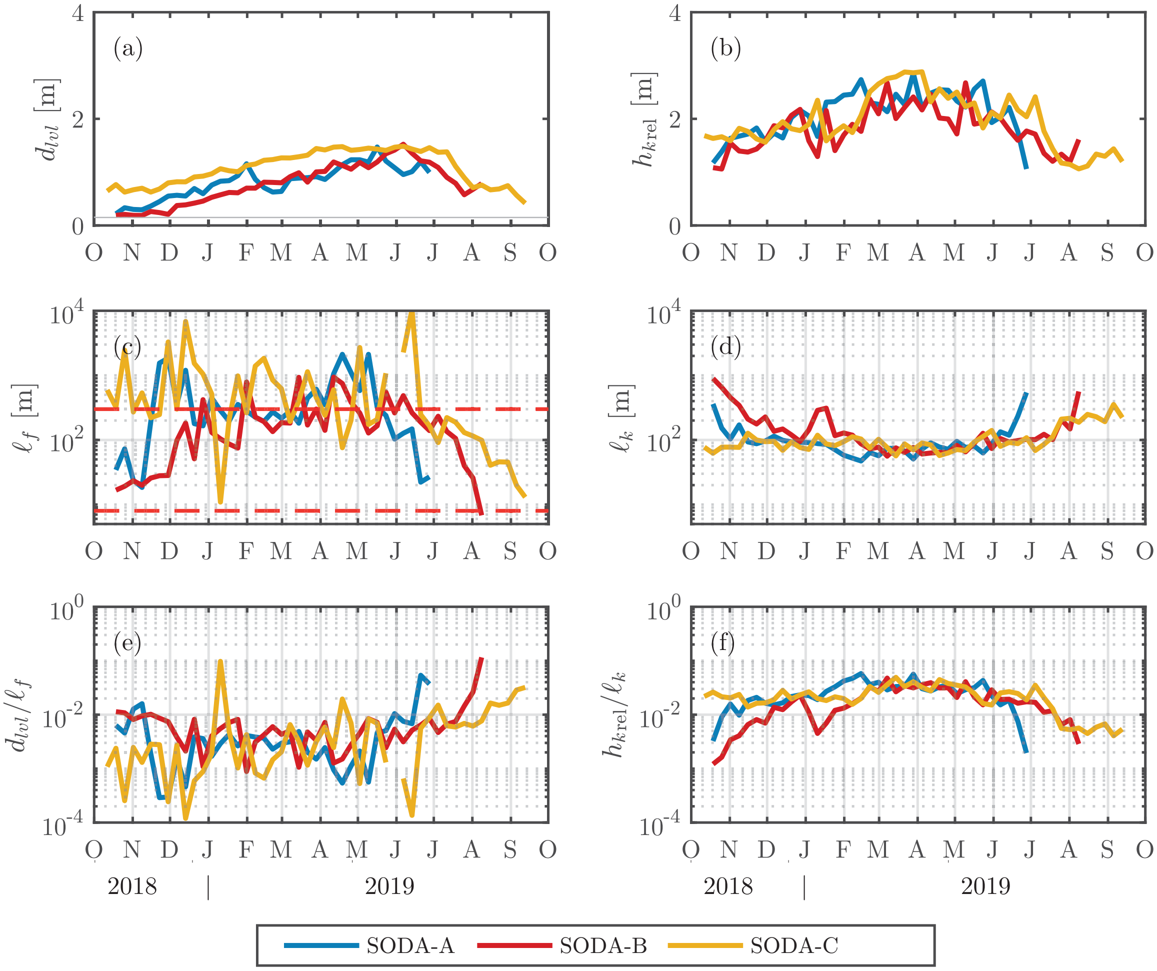

Figure 5: Weekly statistics of sea ice geometry for each mooring: (a) mean level ice draft; (b) mean relative keel depth; (c) mean floe length; (d) mean keel spacing (e) aspect ratio (d_{lvl}/ℓ_f); and (f) ridging intensity (h_k/ℓ_k). Horizontal dashed red lines in (c) show the maximum and minimum extents of the parameterized floe length (eq. 14).

Table 2: Summary of parameters and functions used in the parameterization schemes tested.

	L11	T14(I)	T14(II)	T14(III)
c_f	1	1	$0.3^\dagger$	1
c_k	$1/\pi$	0.2	$0.4^\dagger$	0.2
c_s	2×10^{-3}	2×10^{-3}	eq. $(12)^\ddagger$	2×10^{-3}
z_{0i}	n/a	5×10^{-4} m	1×10^{-3} m	5×10^{-4} m
z_{0w}	n/a	3.27×10^{-4} m	3.27×10^{-4} m	3.27×10^{-4} m
m_w	10	10	10	10
s_l	n/a	0.18	0.18	0.18
S_c	eq. (10b)	eq. (10a)	eq. (10a)	eq. (10a)
P_0	n/a	eq. (11)	eq. $(11)^\ddagger$	eq. (11)
h_k	meas. $h_{k\mathrm{rel}}$	meas. $h_{k\mathrm{tot}}$	meas. $h_{k\mathrm{rel}}$	eq. (13a)
ℓ_k	meas.	meas.	meas.	eq. (13b)
ℓ_f	meas.	meas.	meas.	eq. (14)

†parameters adjusted based on best fit to observations in this study;
‡using a relative reference depth ($z_{\mathrm{ref}} - d_{lvl}$);
n/a: not applicable;
meas.: measured (see section 3.3)

the Tsamados et al. (2014) scheme, labelled T14(II), which uses slightly modified geometry definitions and coefficient values, and still uses direct ice geometry measurements. Finally, the T14(III) variation tested a combination of both physics and ice geometry parameterization from Tsamados et al. (2014), and thus is most comparable to modelling efforts where geometry measurements are not available.

The T14(II) scheme is a modification of the T14(I) scheme, introduced for this study. It still uses the direct measurements of sea ice geometry, but uses the relative definitions of keel depth and reference depth (see section 2.1). Additionally, in T14(II), some of the parameters have been changed from their default values. The skin drag coefficient of resistance (c_s) is replaced with eq. (12) and the roughness length associated with level ice bottom, z_{0i} is replaced with a value of 1×10^{-3} m, which is reflective of observations of ice with no significant morphology (McPhee et al., 1999; McPhee, 2002). With this z_{0i} and a 10-m reference depth, the value of c_s calculated for a 1-m ice draft is 2×10^{-3}, which is the same as in T14(I); however, the use of eq. (12) allows c_s to vary slightly through the year as the ice draft changes seasonally, and gives it an explicit dependence on z_{ref}. By using this formulation c_s is no longer a free parameter. Finally, the coefficients of resistance c_f and c_k have been replaced with values that provide the closest fit between parameterized and observed drag coefficient values when considered across all moorings. These values were found with multiple linear regression: first the values c_f and c_k in eqs. (9a) and (9b) were set to 1, then resulting C_f and C_k from all moorings were regressed against the residual observed drag after subtracting the skin drag component, $C_{io}-C_s$; the regression coefficients then gave the new values of c_f and c_k which were used in T14(II). While used as fitting parameters here, c_f and c_k should be reflective of the individual geometries of the floe edges and keels. For example, the value of $c_k = 0.4$ found with this method corresponds to a keel slope angle of 19.6° based on the fit to experimental results by Zu et al. (2020) (noting that their definition of C_k introduces a factor of $\pi/2$ difference in values of c_k compared to this study), which is close to the mean keel slope of first year ridges of $\alpha_k = 26.6°$ found by Timco and Burden (1997), and the value of $\alpha_k = 22°$ used in the parameterization by Tsamados et al. (2014). Note that the T14(II) scheme does not reflect a full optimization tuning of all of the available parameters, nor is it a rigorous fitting approach for c_f, c_k (as discussed in section 5.2).

As the ADCP measurements provide direct observations of ice geometry (section 3.3), the parameterization of ice geometry (section 2.2) is not necessary in order to implement eq. (9) in L11, T14(I), and T14(II). Instead, this allows us to separately test the physics parameterization (section 2.1) and the geometry parameterization (section 2.2). To do so, a final variation (T14(III)) is tested that uses the default parameter values from Tsamados et al. (2014) but instead of using the direct measurements of sea ice geometry, geometry statistics are estimated using bulk measurements and eqs. (13) and (14).

Application of eq. (13) using ADCP measurements provides some challenges. The ice volume (v_{rdg}) and areas (a_{rdg}, a_i) in eq. (13) are fundamentally defined over a two dimensional area (i.e., within a model gridcell), but the ADCP draft measurements are one dimensional (along-drift). To adapt our measurements to apply eq. (13), we calculate v_{rdg}, a_{rdg}, and a_i on a per-unit-width basis. However, the relative angles between the keel orientations and the direction of sampling (which is unknown) will cause an overestimate of the area or volume of the feature unless measurements are made perpendicular to the keels. Fortunately, this mismatch creates an equal bias for both volume and area calculations, so the ratio v_{rdg}/a_{rdg} in eq. (13a) is not impacted. However, due to crossing angle mismatch, extra care must be taken when calculating and interpreting ℓ_k from eq. (13b). If both keels and leads are linear features whose orientations follow the same statistical distributions then the ratio a_i/a_{rdg} measured with along-drift data will approximate the true (two-dimensional) value if averaged over a sufficiently large sample of keels and leads. However, in full ice cover leads are relatively scarce while in the marginal ice zone it may not be appropriate to consider leads to be linear features. It is unclear whether one-dimensional sampling of a_i will introduce any mean bias. For a uniformly distributed keel orientation, one-dimensional sampling will lead to a mean overestimate of a_{rdg} by a factor of $\pi/2$. On that basis a_{rdg} are multiplied by a $2/\pi$ correction factor when applying eq. (13b).

4 Results

4.1 Seasonal and spatial variation of ice-ocean drag

For all three moorings, the force-balance approach provided estimates for the ice-ocean drag coefficient, C_{io}, throughout the full annual cycle (fig. 6) even despite some winter data gaps (due to higher internal stresses). These estimated values of the ice-ocean drag coefficient exhibit both spatial and seasonal variations.

Drag coefficients measured at SODA-A and SODA-B (the two southern moorings; fig. 2a) show a similar seasonal behaviour. For both, the drag coefficients start at low values (C_{io} ~2×10^{-3} to 3×10^{-3}), and steadily increase through the winter to a maximum in spring (Apr.–May) before declining (figs. 6b and 6c). The decrease of C_{io} is more gradual at SODA-B than SODA-A, and summertime minimum values at SODA-A are lower than at SODA-B (cf., figs. 6b and 6c). The timing of the shift from increasing to decreasing C_{io} at these two moorings is roughly coincident with the change from net surface cooling to net surface heating in the atmospheric re-analysis data, which occurred in Apr.–May.

In contrast, the record at SODA-C begins with an elevated drag coefficient ($C_{io} \sim 6 \times 10^{-3}$) which remains roughly constant from fall through spring (fig. 6a). After the shift to net atmospheric surface heating in Apr.–May, there may be a slight decline in

C_{io}, but values are still elevated for some months, until there is a sharp drop in early to mid-July. This sudden drop in ice-ocean drag is associated with a similar sharp decline in both floe sizes (fig. 5c) and ridging intensity (fig. 5f), suggesting a dramatic ice breakup and melting event occurred.

At all three moorings, drag coefficient values from mid-winter to spring are similar to each other, and fluctuate near or above the canonical value of $C_{io} = 5.5 \times 10^{-3}$. However, differences between the moorings in fall and summer imply large-scale spatial gradients in the ice-ocean drag coefficient across the Beaufort Sea. Section 4.3 discusses morphological drivers of the observed seasonality in greater depth.

4.2 Evaluation of parameterization schemes

Ice-ocean drag coefficients calculated with all of the tested parameterization schemes (table 2) show values and temporal variability that broadly match the values observed with the force-balance approach (fig. 6). This agreement indicates that variability of ice-ocean drag can be primarily explained by seasonal changes in the ice morphology and the associated skin/form drag contributions. Despite general success, some versions of the parameterization schemes are better performing. In particular, while the T14(III) scheme provides a reasonable match at all moorings in the early part of the record, it diverges significantly from the observations in the latter half of the record, and even reaches a maximum C_{io} in summer/fall when the observations show a minimum. Figure 7 shows direct comparisons of the observed and parameterized values for each of the four test schemes. There is good agreement between the observed drag coefficients and those predicted by both L11 and T14(I) when C_{io} are low ($\lesssim 5 \times 10^{-3}$); for higher values of C_{io} ($\gtrsim 5 \times 10^{-3}$), there is a roll-off of the modelled values (figs. 7a and 7b). Values from T14(II) follow the one-to-one line across the full range of C_{io} (fig. 7c), while those from T14(III) are mostly above the one-to-one line and do not present any recognizable correlation with force-balance observations. A few notable outliers exist that are not described by any of the model schemes (e.g., high observed values of drag in mid-April at SODA-A; fig. 6a), potentially suggesting other sources of drag (e.g., internal wave drag) that cannot be explained by ice geometry variations alone; however, these points are fairly limited.

These statements are corroborated by quantitative assessments of model performance across all moorings (table 3). Values from both L11 and T14(I) have weak cor-

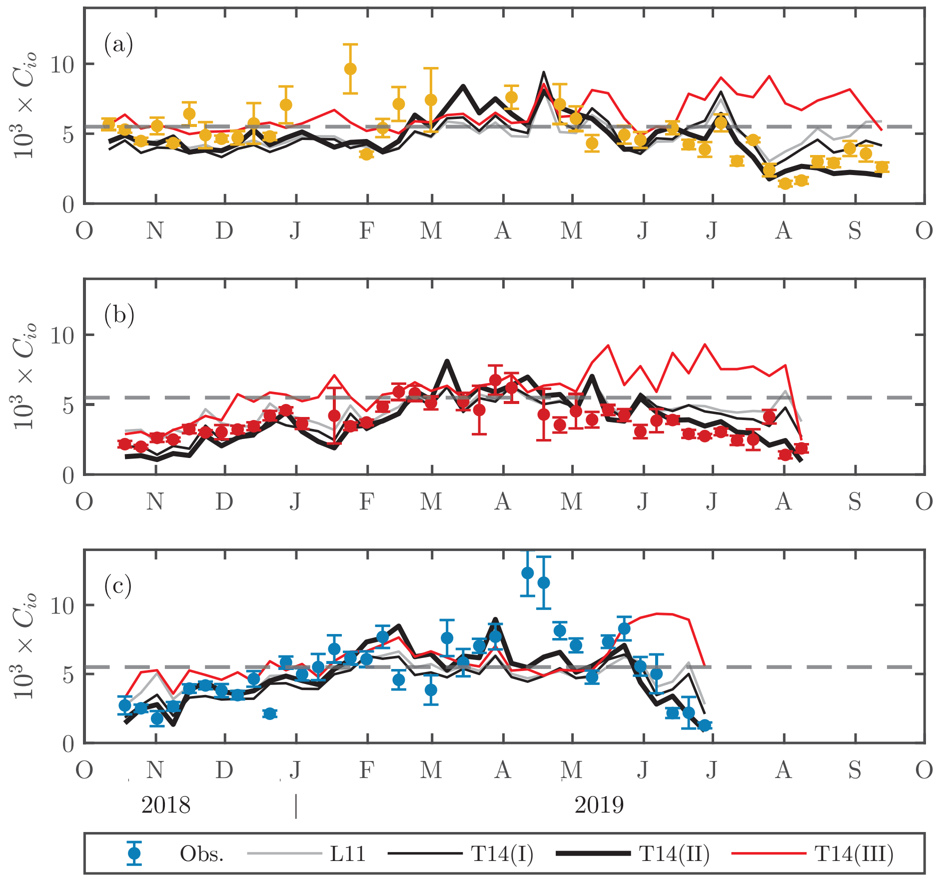

Figure 6: Ice-ocean drag coefficients from north-to-south: (a) SODA-C, (b) SODA-B, and (c) SODA-A. In each panel, points with error-bars (coloured by moorings per fig. 2a) show the values of C_{io} calculated with the force-balance approach (labelled "Obs."), while lines correspond to the different variations of parameterization schemes (table 2), as indicated by the legend. Error bars show 95%-confidence interval bounds from the linear fitting procedure. The horizontal grey dashed line shows the value of $C_{io} = 5.5 \times 10^{-3}$ for comparison.

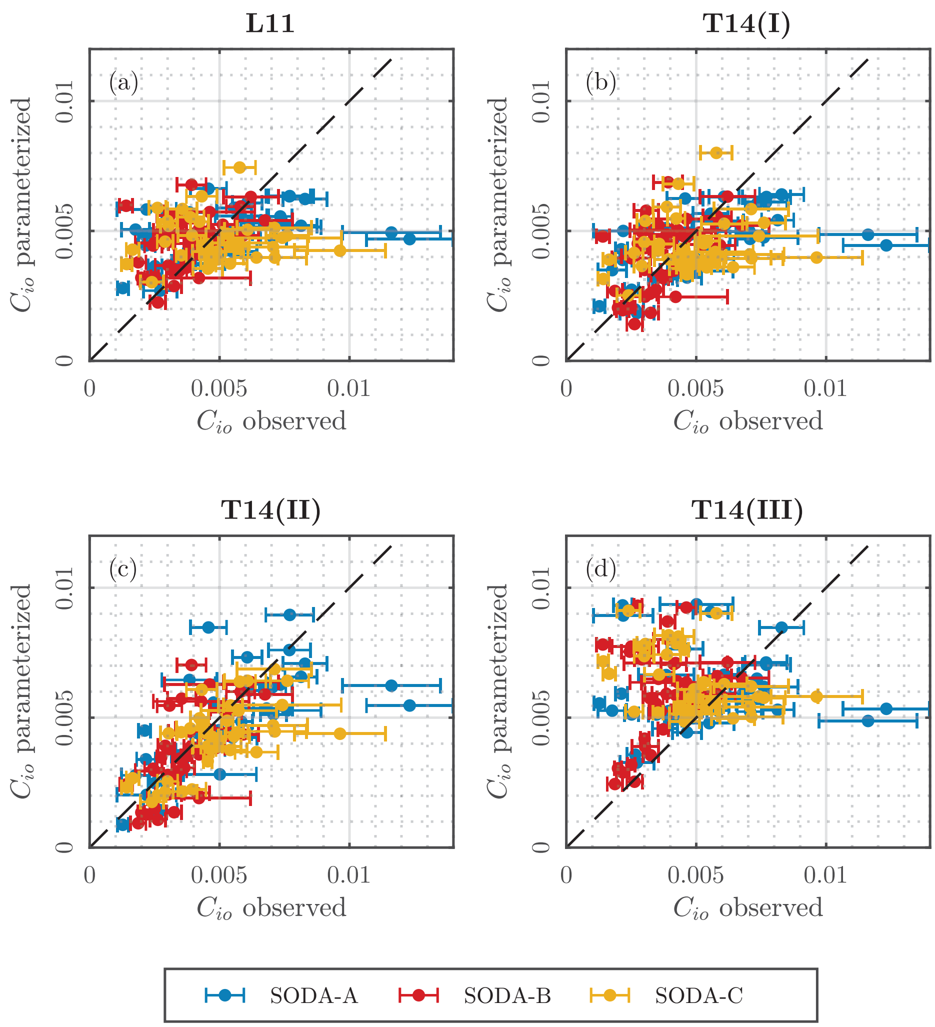

Figure 7: A comparison between the ice-ocean drag coefficients determined using the force-balance approach ("observed"), and using the different variations of geometry-based parameterization: (a) L11, (b) T14(I), (c) T14(II), and (d) T14(III). In each panel, the black dashed line shows the one-to-one slope, and the points are coloured by mooring according the legend.

Table 3: Summary of fit statistics of ice-ocean drag coefficients determined using the force-balance approach and using the different variations of geometry-based parameterization. (NRSME = normalized root mean square error; NBI = normalized bias)

Scheme	r^2	NRMSE	NBI
L11	0.13	0.37	-0.00
T14(I)	0.22	0.36	-0.08
T14(II)	0.46	0.31	-0.09
T14(III)	0.00	0.57	0.31

relations with observations ($r^2 = 0.13$ and 0.22, respectively). T14(I) has a slightly negative normalized bias (NBI; -012), while L11 is approximately unbiased. The T14(II) scheme has the best correlation of the four tests ($r^2 = 0.46$), the lowest normalized root-mean-squared error (NRMSE; 0.31), though it also has a slightly negative normalized bias (-0.09). When considered over the full year, the T14(III) scheme is biased high (NBI of 0.31), has high NRMSE (0.57), and is uncorrelated with observations; however, if only the early part of the record (before May 2019) is considered, the fit is better ($r^2 = 0.17$, NRMSE=0.35). Tests in which the observed drag coefficients and geometry statistics were determined using different window lengths (ranging between 1 d and 14 d) all produce similar correlations as the 7-d windows presented (not shown), giving confidence that the parameterization schemes are appropriate over a wide range of scales.

4.3 Partitioning of drag components and predictions of ice geometry

Parameterized ice-ocean drag coefficients are built up from three components: form drag on floe edges (eq. 9a), form drag on keels (eq. 9b), and skin drag (eq. 9c). Insofar as the ice-ocean drag coefficient is driven by ice morphology, examination of the partitioning of drag components allows us to better understand the impact of those morphological variations. In all four of the parameterization schemes tested, the ice-ocean drag coefficient in the winter is largely driven by form drag on ice keels (C_k). Skin drag (C_s) is generally much smaller, and does not show significant seasonal variation, and floe edge drag (C_f) becomes more important in the summer as the ice begins to melt and break apart into smaller floes. This general pattern qualitatively matches results from sea ice models (Tsamados et al., 2014; Martin et al., 2016), but details vary from those model results.

For the three schemes that use direct measurements of the geometry (L11, T14(I), and T14(II)), the seasonality of C_{io} observed in fig. 6 is driven by seasonal growth and melt of ice keels, as seen by variation in C_k (T14(I) and T14(II) are shown in figs. 8a to 8f; L11 is very similar to T14(I) so it is not shown). The exact partition between C_f and C_k in these schemes depends on the values of the coefficients of resistance c_f and c_k (see table 2), but the overall behaviour is similar for the different schemes (c.f. figs. 8a to 8c and figs. 8d to 8f). At the southern moorings (SODA-A, -B), which start the timeseries in open water, there is initially only small contribution from C_k and most of the drag is due to a combination of C_f and C_s. As the number and size of keels grow through the year (fig. 5), so too does the contribution from C_k (figs. 8b, 8c, 8e and 8f). At SODA-C, the timeseries begins in ice cover with established ridging, and C_k is the main component of C_{io} from the onset (figs. 8a and 8d). All three moorings have some small contributions to floe edge drag throughout the full year due to the presence of (potentially refrozen) leads. Following the onset of melting conditions, an increase in floe edge drag accompanies the decline of keel drag at all locations; however, the increased floe edge drag is not enough to compensate for the lack of keels at any of the moorings (figs. 8a to 8f). This contrasts the modelling results from Tsamados et al. (2014) and Martin et al. (2016), which show that floe edge drag is substantial during summer/fall. While not the main focus here, it is also noteworthy that keel decline varied between the three moorings: at both the southernmost mooring (SODA-A) and northernmost mooring (SODA-C), there was a fairly rapid drop in C_k over the period of approximately 2 weeks in late June and early July, respectively, due to both decreased size and number of keels (figs. 5b and 5d); at SODA-B, the decrease in C_k was more gradual. Note that at SODA-A and -B, where there was a strong seasonality in keel drag, growth of C_k proceeded at a much slower rate than ice cover growth; at both moorings, ice concentration was close to 100% by early November (figs. 2c to 2e), while C_k remained relatively low through January. As such, it is unlikely that ice concentration based drag parameterizations (such as are suggested for atmospheric drag; e.g., Andreas, Horst, et al., 2010) would ever be able to sufficiently capture observed seasonal variations in C_{io}.

The drag partition from the T14(III) scheme (figs. 8g to 8i) differs from the results of the T14(II) scheme. While keel drag (C_k) is still the dominant contribution during

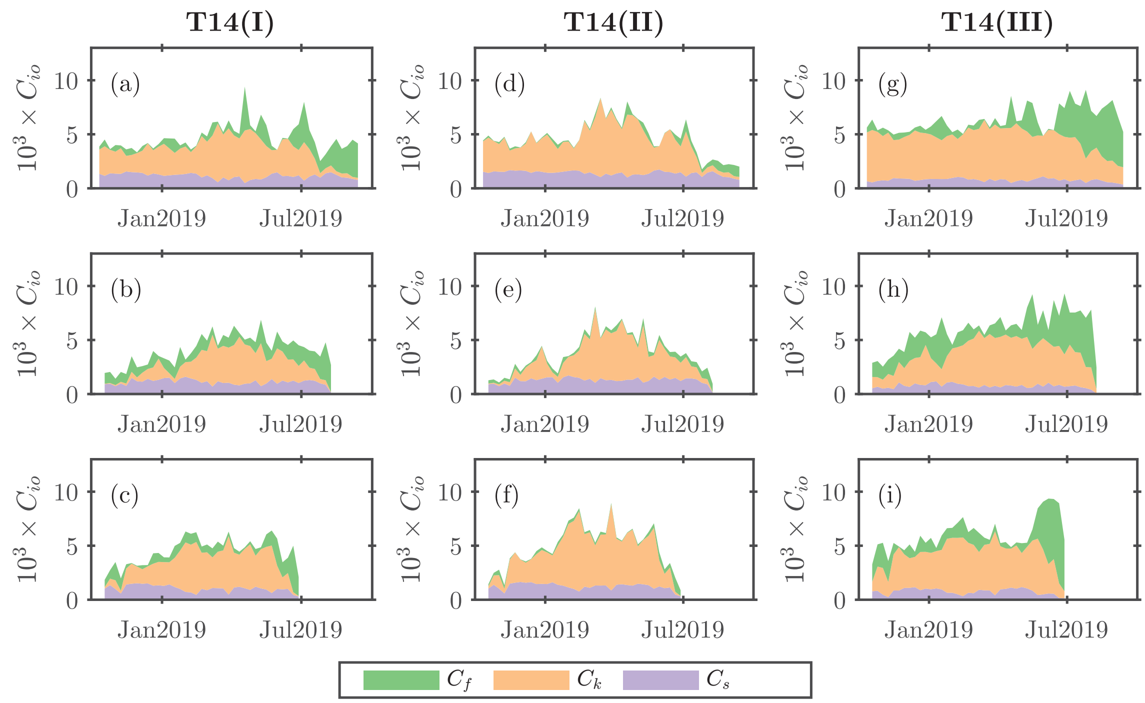

Figure 8: Stacked contributions to the ice-ocean drag coefficient C_{io} from form drag on floe edges (C_f), form drag on keels (C_k), and skin drag (C_s) calculated using (a-c) the T14(I) scheme, (d-f) the T14(II) scheme, and (g-i) the T14(III) scheme (see table 2) for (a,d,g) SODA-C, (b,e,h) SODA-B, and (c,f,i) SODA-A.

winter, its seasonality is somewhat muted compared to T14(II) (compare C_k in figs. 8d to 8f with figs. 8g to 8i). More striking are the differences in floe edge drag: C_f is much higher in the T14(III) scheme at all moorings and times of the year, and in summer/fall the increase in C_f outpaces the associated decrease in C_k. As a result, the T14(III) scheme has the largest value of C_{io} in summer/fall, which conforms to previous model results (Tsamados et al., 2014; Martin et al., 2016). While these differences can be partly attributed to the differences in coefficients of resistance between the two schemes (c_f and c_k, see table 2), the main difference arises from the fact that the T14(III) scheme does not use direct measurements of the sea ice geometry, and instead relies on parameterized geometry statistics (section 2.2). In the early part of the record, before C_f becomes large, the T14(III) scheme is comparable to the other parameterization schemes.

Differences in C_f between T14(II) and T14(III) depend mainly on the floe aspect ratio, d_{lvl}/ℓ_f, while differences in C_k depend on the ridging intensity, h_k/ℓ_k. As shown in figs. 9a and 9d, neither of these ratios is well predicted by the parameterizations of ice geometry eqs. (13) and (14), with parameterizations overestimating the results in both cases. For the highest values of ridging intensity ($h_k/\ell_k \gtrsim 5 \times 10^{-2}$) predicted values fall near the one-to-one line but deviate substantially as observed values decrease (fig. 9a). As such, the overall magnitude of C_k values is not strongly modified by the over-prediction of ridging intensity, but the decreased range of variability of modelled values is responsible for the muted seasonality of C_k seen in the T14(III) scheme. Considering the separate roles of h_k and ℓ_k in setting this ratio, the predictions of each individual variable have as much (or more) variability as observations (fig. 9b), but there is an apparent compensating effect between the two quantities. Predicted values of h_k and ℓ_k vary roughly along lines of constant h_k/ℓ_k, while observations vary primarily across lines of h_k/ℓ_k.

The elevated levels of C_f seen in the T14(III) test result from parameterized values of the aspect ratio, d_{lvl}/ℓ_f, being much greater than observations across nearly the full range of values (fig. 9d, black points), with a median factor of $\sim$4 times higher than the observed values. Differences between the observed and predicted aspect ratio are driven solely by differences in ℓ_f (d_{lvl} is not parameterized), which is generally underestimated by eq. (14) (fig. 9c). The relationship between floe lengths and ice concentration used in eq. (14) to predict ℓ_f is an empirical result derived from a set of aerial photos of ice in the marginal ice zone in the Fram Strait (Lüpkes et al., 2012). However, a wide variety of factors set the size and density of floes (Roach et al., 2018) and so it is unlikely that such empirical relationships would be valid in different Arctic regions and all times of year. The mismatch in the seasonality of C_{io} between observations and values predicted with the T14(III) parameterization arise mainly from this overestimate of aspect ratio. A modification to the parameters used in eq. (14) (to $\ell_{f,min} = 18.4\,\mathrm{m}$, $\ell_{f,max} = 1730\,\mathrm{m}$, $b_2 = 0.9$) provided a much better to fit the floe length observations (fig. 9c, and fig. 9d, grey points). However, the applications of the T14(III) scheme using the modified parameters in eq. (14) still retained the seasonal mismatch in C_{io} (not shown), albeit to a lesser degree (possibly due to the very wide variability around the fitted curve in fig. 9c, noting that the comparisons in fig. 9d are plotted on logarithmic axes).

5 Discussion

5.1 Comparison with previous drag observations

The range of values reported for the ice-ocean drag coefficient are consistent with previous observations. Shirasawa and Ingram (1991) and Lu et al. (2011) collated observations of the ice-ocean drag coefficient from a wide set of historical studies (publication dates from 1970 to 1997). These studies indicate a broad range of measured values with extremes from as low as 0.13×10^{-3} (under land-fast ice in Hudson's bay; Shirasawa et al., 1989) to the highest value of 47×10^{-3} (indirectly estimated based on fitting log-layer profiles to velocity measurements; Johannessen, 1970). The bulk of the studies summarized suggest drag coefficient values range from roughly 1×10^{-3} to 20×10^{-3}. More modern studies based either on direct measurements (Shaw et al., 2008; Randelhoff et al., 2014; Cole et al., 2014, 2017) or force-balance approaches (Randelhoff et al., 2014; T. W. Kim et al., 2017; Dewey, 2019; Heorton et al., 2019) provide similar limits. This study finds drag coefficient values from 1.3×10^{-3} to 12.3×10^{-3}, which fall well within the conventional bounds, and the mean and median values are close to, but slightly below, the canonical drag coefficient value of 5.5×10^{-3} (fig. 10). The overall mean value of 4.6×10^{-3} in these observations is very similar to the average ice-ocean drag coefficient of 4.7×10^{-3} found by Dewey (2019) for the Beaufort Sea.

Cole et al. (2017) present detailed analysis of surface momentum flux from four ice drift stations in the Beaufort Sea, each containing a cluster of autonomous instruments. The four clusters provide measurements spanning March to December 2014, nearly a full annual cycle. Their results show weekly median ice-ocean drag coefficients ranging from

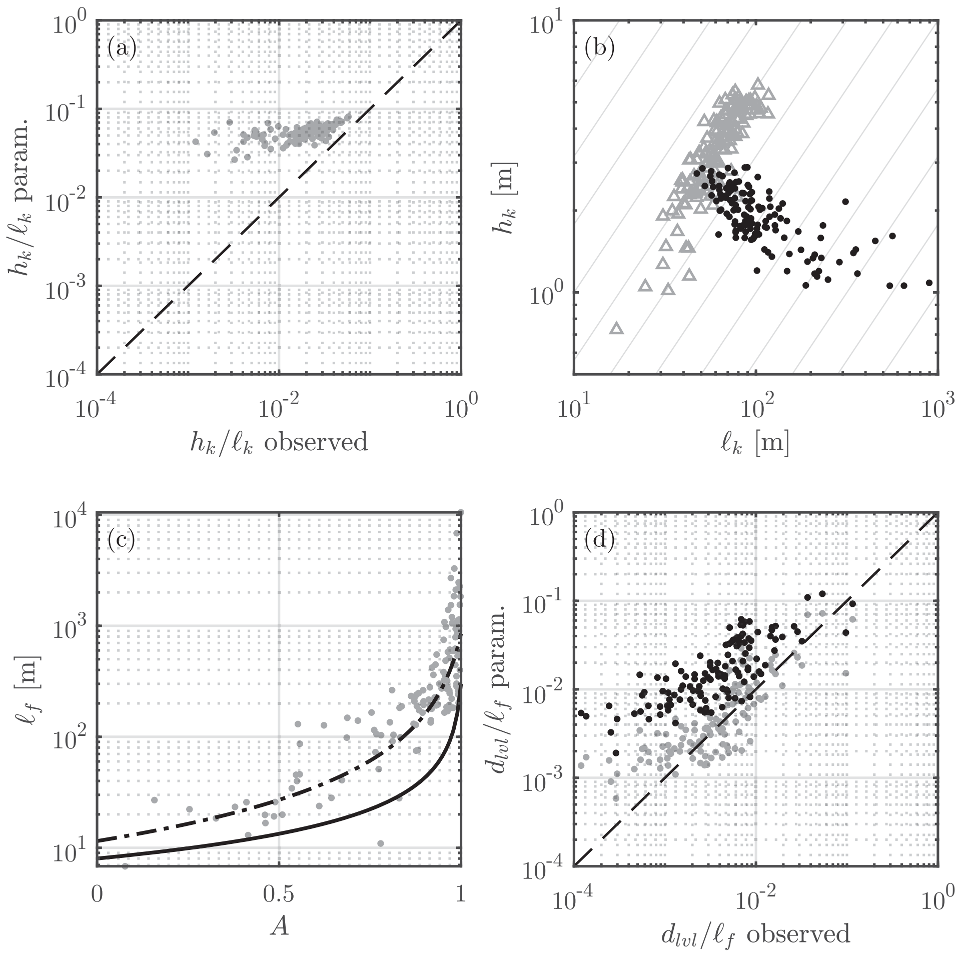

Figure 9: A comparison of observed and parameterized sea ice geometry statistics: (a) Observed versus parameterized ridging intensity (h_k/ℓ_k) with weekly values measured at all moorings; the black dashed line shows the one-to-one slope. (b) Weekly values of ridge spacing (ℓ_k) versus keep depth (h_k) from observations (black points) and parameterizations (grey triangles). Grey contours correspond to lines of constant h_k/ℓ_k. Observed values of h_k in (a) and (b) are relative keel depth ($h_{k\mathrm{rel}}$). (c) Observed floe length ℓ_f as a function of ice concentration A (grey points) showing the fit of eq. (14) when using the default parameter set (solid black line), and with modified set of parameters (dashed line). (d) As per (a) but for aspect ratio (d_{lvl}/ℓ_f); black points show the aspect ratio when ℓ_f is calculated using the default parameters in eq. (14), and grey points show the aspect ratio when a modified set of parameters are used in eq. (14).

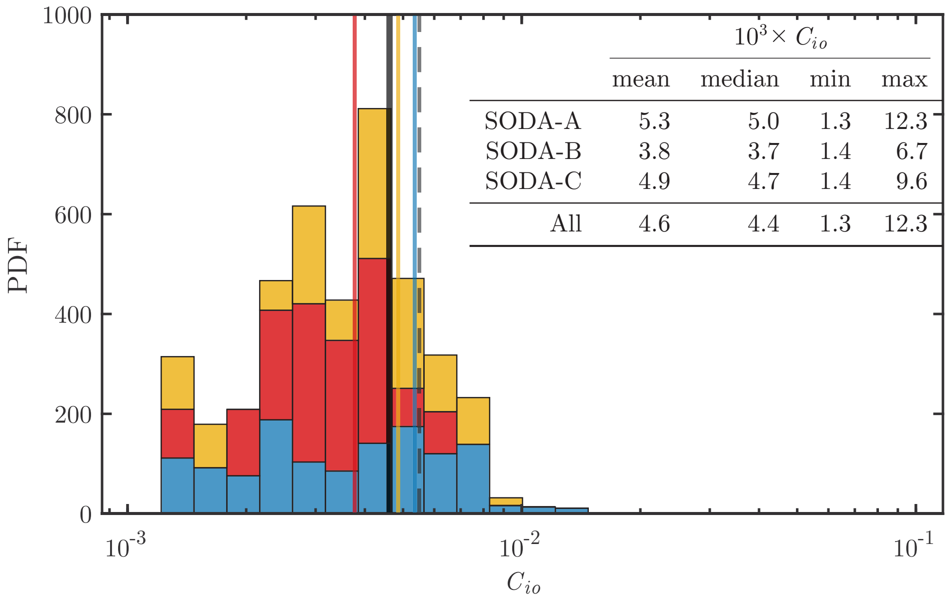

Figure 10: Stacked histograms showing the probability distribution function (PDF) of the ice-ocean drag coefficient values calculated at each of the three moorings (coloured by mooring according to fig. 2a). Coloured vertical lines show the annual mean value of C_{io} for each mooring, and the vertical black line shows the overall mean. The vertical grey dashed line shows the value of $C_{io} = 5.5 \times 10^{-3}$ for comparison.

approximately 0.2×10^{-3} to 10×10^{-3}, with significant spatial and temporal variability (see their figure 12). Their measured values of C_{io} span a broader range than reported here, with minimum values an order-of-magnitude lower than ours (but similar maximum values). Nonetheless, there is good agreement with some of the qualitative behaviour exhibited by the ice cluster measurements. Namely, despite strong spatial variation in the values of C_{io}, all of the ice clusters showed consistent seasonal variations in ice-ocean drag, with minimum values at the time of ice minimum (Aug.–Sep.) and maximum values in spring (Apr.–Jun.). Dewey (2019) find a similar seasonal cycle based on a force-balance approach to calculate C_{io} from remote measurements in the Beaufort Sea over a 5-year period from 2011–2016: basin-wide average C_{io} show minimum values from Jul.–Oct. of each year. These patterns are in agreement with our observations which show minimum ice-ocean drag coefficient values in fall (fig. 6). In contrast, pan-Arctic averages of C_{io} from models incorporating a variable drag coefficient scheme (section 2.1) show the opposite behaviour (Tsamados et al., 2014; Martin et al., 2016). In those models, the maximum value of C_{io} occurs during the summer/fall season, driven by form drag on floe edges (eq. 9a). As described above (section 4.3), seasonality in modelled values of C_{io} may be a result of over predicted values of the floe aspect ratio, d_{lvl}/ℓ_f.

With a few exceptions, direct observational estimates of the ice-ocean drag coefficient are made using point measurements of turbulent fluxes. In comparison to the force-balance approach used here, C_{io} values derived from point measurements require far fewer assumptions about the ice dynamics (e.g., they are valid whether or not the ice is in free drift). However, these measurements are also inherently local and as such it is not clear how they scale to application across entire ice floes. For logistical reasons, measurements are typically made away from ice keels, so reported values of C_{io} may under-represent floe- or regional-average values (McPhee, 2012). Randelhoff et al. (2014) provide a direct comparison between a force-balance approach to calculate ice-ocean drag (the procedure used here) and in-situ measurements of turbulent fluxes. Their results showed that the force-balance approach produced ice-ocean stress estimates that were, on average, 3 times larger than direct measurements. They attribute the mismatch to unmeasured sources of drag (e.g., due to internal wave radiation; McPhee & Kantha, 1989), but it may also be due to horizontally varying and thus non-local turbulence. Similarly, application of the force-balance approach to the ice cluster data from Cole et al. (2017) shows higher values of C_{io} and decreased temporal variability compared to local measurements

(Heorton et al., 2019). While this may explain why the values of C_{io} observed here have a much higher minimum value than those by Cole et al. (2017), more work is needed to understand the inherent differences in between direct point measurements and force-balance measurements of ice-ocean drag.

In comparing values of C_{io} between different studies, it is important to consider the choice of reference depth used, which will impact the drag coefficient through depth variations of $\boldsymbol{u}_o$. For example, repeating our analysis with a shallower reference depth of $z_{ref} = 6\,\mathrm{m}$ yields slightly higher values of C_{io}, with an overall average of 5.2×10^{-3} (compared to 4.6×10^{-3} for $z_{ref} = 10\,\mathrm{m}$). Typically, values of C_{io} are reported corresponding to either fixed reference depths near the ice bottom, thus in or near the logarithmic boundary layer, or they are reported using the underlying geostrophic current, $\boldsymbol{u}_g$, as a reference velocity (table 1 in Lu et al., 2011, lists reference depths used for a number of studies). Within the log-layer, $\boldsymbol{u}_o \propto \boldsymbol{u}_*$, so the application of the quadratic drag law is appropriate. However, beyond the logarithmic layer, the relationship between stress and velocity in the ice-ocean boundary layer is not expected to be quadratic (e.g. McPhee, 2008, and references therein). If $\boldsymbol{u}_g$ is used as a reference velocity, drag may be better described by Rossby Similarity Theory (Blackadar & Tennekes, 1968; McPhee, 2008), which accounts for the existence of an outer Ekman-like layer matched to an inner logarithmic layer (as has been observed in the ice-ocean boundary layer, e.g., Hunkins, 1966; McPhee, 1979). In this more general case, McPhee (1979, and others) find reasonable empirical agreement from an alternative power law form: $|\boldsymbol{\tau}_{io}| \propto |\boldsymbol{u}_i - \boldsymbol{u}_g|^n$ where $n < 2$ (e.g., Cole et al., 2017, find values of n ranging from 0.51 to 1.76). The use of a fixed reference depth of $z_{ref} = 10\,\mathrm{m}$ in the present study likely extends beyond the surface log-layer so the quadratic drag law is not strictly applicable. Nonetheless, tested parameterizations that assume a law-of-the-wall velocity profile (T14(I), T14(II)) produce reasonable results (figs. 6 and 7). Furthermore, the relationship between stress and relative velocity seems to be well described by the quadratic drag law (fig. 3). This suggests a "fuzzy" transition between the inner logarithmic boundary layer and the outer Ekman-like layer such that the law-of-the-wall still provides a useful approximation for determining C_{io}. Likely, the use of a smaller reference depth that is closer to the base of the logarithmic boundary layer may increase the accuracy of the quadratic drag assumption (e.g., Park & Stewart, 2016, suggest a hybrid Rossby Similarity Theory using the quadratic drag law to model the inner boundary layer coupled to classic Ekman-layer dynamics for the outer layer).

5.2 Recommendations for model development

This study identifies some possible directions that future modelling work could focus on. The parameterizations here can be described as having two parts: one part that models the underlying physics (eqs. 9; tested by schemes L11, T14(I), T14(II)), and a second part for the geometry (eqs. 13 and 14; tested by scheme T14(III)). There are some opportunities for improvements in both of these parts; however, based on the results in section 4.3, it is apparent that there is a more urgent need to improve descriptions of the sea ice geometry.

Translating bulk sea ice model outputs to the detailed geometry needed to apply eqs. (9a) to (9c) appears to be a particular challenge. Both the ridging intensity, h_k/ℓ_k, and the floe aspect ratio, d_{lvl}/ℓ_f, are overpredicted by the parameterization schemes from section 2.2 (see fig. 9). Some efforts are being made to directly model different aspects of the sea ice geometry (e.g., floe sizes, Roach et al., 2018; or keel statistics, Roberts et al., 2019), thus alleviating the need for geometry parameterizations. However, until such modelling schemes are widely implemented, there will be some value in improvements to existing geometry parameterizations.

The keel depth and spacing predicted from model outputs by Tsamados et al. (2014) (eqs. 13a and 13b) are based on geometric arguments that are informed by measurements of sea ice sails and keels. In formulating those equations, the authors assume a uniform field of equally sized, shaped, and spaced non-overlapping ridges in each grid cell box. However, past measurements have shown that keel depth, width, and spacing are better described by statistical distributions (e.g., Hibler et al., 1972; Wadhams & Davy, 1986; Davis & Wadhams, 1995; Timco & Burden, 1997; Martin, 2007). Some improvement in the parameterizations could likely be made simply by considering the shape of these distributions. For example, using an exponential distribution to describe relative keel depths (per Wadhams & Davy, 1986), the total ice volume associated with keels will differ from that calculated with a uniform distribution by a factor of 2 when both distributions have the same mean keel depth. Figure 9b suggests that some of these geometry variables may be jointly distributed.

The mismatch between modelled and observed seasonal variations in ice-ocean drag coefficients is largely due to discrepancies in modelled floe lengths, ℓ_f (section 4.3). The floe length parameterization (eq. 14) is an empirical result relating ℓ_f to A from aerial photographs of ice in the Fram Strait in the 1990s (Lüpkes et al., 2012). While Lüpkes et al. (2012) developed this relationship for the marginal ice zone, its implementation by Tsamados et al. (2014) does not distinguish between marginal and pack ice (though the authors acknowledge a possible breakdown in winter conditions). Additionally, Lüpkes et al. (2012) highlight that variability in the relationship between ℓ_f and A points to other variable dependencies on floe sizes. Employed here, we are able to adjust the input parameters to eq. (14) to provide a better fit to the observed floe lengths (fig. 9c), suggesting that some general variability in the behaviour of floe length may be modelled by some form of that equation. However, there remains a significant amount of scatter in the observations (over orders of magnitude), and so even with the adjusted parameters the model floe edge drag is still too high during the ice melt season. Future development of empirically derived floe length parameterizations should, at minimum, include observations from across different Arctic regions based in modern ice conditions. Moreover, deterministic models for the evolution of floe size distributions (Horvat & Tziperman, 2017; Roach et al., 2018) highlight which other variables could be included in empirical fits. For example, rather than casting ℓ_f as a function just of A, it may be more appropriate to develop two-parameter empirical fits that also include the ice thickness. Further multi-parameter fits might consider the inclusion of wind speed, $|\boldsymbol{u}_a|$ (which would have impacts both on sea ice welding and breakup by driving ice motion, and on surface wave conditions which can lead to fracture), and sea surface temperature (which is important for lateral growth and melt).

While better geometry schemes should be a focus, the improvement of the T14(II) scheme over the L11 and T14(I) schemes also show that minor modifications to the physics part of the parameterization scheme have the potential to increase the predictive skill. There are a number of changes between the schemes (see table 2), however, most of the improvement is made by simply choosing more appropriate values of the coefficients of resistance c_f and c_k. While those are chosen here with a slightly ad hoc fitting method (using multiple linear regression; see section 3.4), determining appropriate ranges for these values is a subject of ongoing research (e.g., Zu et al., 2020). In addition to these coefficients, the parameterization schemes tested include a number of other constants whose values are not fully constrained that could be used to tune the modelled drag coefficients: c_s, s_l, z_{0w}, z_{0i}, m_w.

Detailed optimization accounting for all free parameters or more rigorously fitting the values of c_f and c_k is deliberately not performed here. This choice is primarily driven by the fact that the tests here do not account for all of the physical processes that modify the ice-ocean drag coefficient. In particular, the parameterization schemes only model the neutral drag coefficient and do not account for variations due to buoyancy (which should be included as a correction term; e.g. Lüpkes & Gryanik, 2015), whereas the observed values of C_{io} reflect the total drag, including non-neutral effects. Similarly, shallow surface stratification may act to partly decouple the sea ice motion from subsurface velocity measurements, especially during the melt season. Additionally, drag due to internal wave radiation is thought to be important in some oceanographic conditions (McPhee & Kantha, 1989; Pite et al., 1995) but is not included. Finally, the forms of the functions P_0 (eq. 11) and c_s (eq. 12) are based on an assumed velocity profile that may not be suitable through the full reference depth; the logarithmic boundary layer at the ice-ocean interface is thought to be only $\sim$2 m thick (e.g. McPhee, 2002; Shaw et al., 2008; Randelhoff et al., 2014; Cole et al., 2017), which is much shallower than the 10-m reference depth used. The generally close match between parameterized values of C_{io} (with T14(II)) and those determined through the force balance suggest that these effects may be small, but a thorough optimization of free parameters should be performed that considers these effects.

In addition to improvements in existing parameterizations, there has been some interest in simplified parameterization schemes for drag coefficients based solely on ice concentration (which have been applied for atmospheric drag; e.g., Andreas, Horst, et al., 2010; Andreas, Persson, et al., 2010; Lüpkes et al., 2013). While there is some value in such an approach, we recommend caution in the development of such schemes for the ice-ocean drag coefficient. The atmospheric drag schemes such as those by Andreas, Horst, et al. (2010) focus on the effects of floe edges, and thus might work well when the sea ice concentration dominates form drag but less well when drag is dominated by ice ridges. Because of the different scales of both the boundary layer and the ridges at the ice-ocean boundary compared to the atmosphere-ice boundary, the influence of keels on ice-ocean drag may be much more important than the influence of ice sails on atmospheric drag. Thus, approaches for simplified modelling employed in atmospheric literature may not be appropriate to adopt for ice-ocean drag. The differing timescales for ridge intensity growth (relatively slow; fig. 5e) compared to ice concentration growth (relatively rapid; figs. 2d and 2e), along with the strong control of ridging intensity on the total ice-ocean drag (section 4.3) means that concentration-based schemes are unlikely to be capable of representing ice-ocean drag. From the results of this study, we speculate that a simplified ice-ocean drag parameterization might be better described with a two-parameter scheme that includes both ice concentration and ice thickness.

5.3 Implications for momentum transfer into the ocean

We have focused on the efficiency of momentum transfer between the sea ice and the upper ocean; however, these questions exist in a broader context of the impact of sea ice on mediating total momentum flux between the ocean and the atmosphere. Conventional wisdom has been that sea ice damps atmosphere-ocean momentum flux (Plueddemann et al., 1998; Rainville & Woodgate, 2009), and so an increase in open water will lead to an increase in momentum flux into the ocean (Rainville et al., 2011). However, other recent studies have suggested a more complex view (Martin et al., 2014, 2016; Dosser & Rainville, 2016). Martin et al. (2014, 2016) show that sea ice can either enhance or diminish momentum flux into the ocean depending on the interplay between internal ice stress and wind stress (which is amplified over the sea ice; e.g., Guest et al., 1995, and many others). A detailed accounting of the upper ocean response to the combined sea ice and atmospheric forcing is outside the scope of the current study; here we consider the potential for amplification or damping of momentum flux into the ocean by sea ice.

The equivalent drag coefficient, C_{equiv} (eq. 7) provides a measure of the total momentum transfer efficiency between the atmosphere and the ocean as it is mediated by sea ice. To provide additional context for the observations, consider two limits for the value of C_{equiv}: (1) a "free-drift limit", where $\boldsymbol{F}_a = \boldsymbol{F}_i = 0$ in eq. (6), so $\boldsymbol{\tau}_{ocn} = \boldsymbol{\tau}_{atm}$; (2) the atmosphere-ice stress, $\boldsymbol{\tau}_{ai}$, is balanced by internal ice stress, $\nabla \cdot \boldsymbol{\sigma}$, and $\boldsymbol{F}_a$ is negligible, so $\boldsymbol{\tau}_{io} = 0$. Then for each case the equivalent drag coefficient is given by:

$$\text{case 1:} \qquad C_{equiv} = AC_{ai} + (1-A)C_{ao}, \tag{15a}$$

$$\text{case 2:} \qquad C_{equiv} = (1-A)C_{ao}. \tag{15b}$$

Taking C_{ao} as constant (an appropriate approximation for typical wind speeds), the two cases above provide formula for C_{equiv} that are functions solely of ice concentration (noting application of an ice-concentration based parameterization scheme for C_{ai}). While these two cases are referred to as limits, they are not strict limits as both the role of acceleration terms ($\boldsymbol{F}_a$) and the vector addition of terms in eq. (6) can either increase or decrease C_{equiv} beyond these bounds.

Values of C_{equiv} span a wide range, and the variability of observed values increases with increasing sea ice concentration (fig. 11). This increase in variability of C_{equiv} with A reflects the divergence of the two limits of C_{equiv} introduced above, which both approach C_{ao} as $A \to 0$ but either increase (eq. 15a) or decrease (eq. 15b) as A increases. Results also show a separation of C_{equiv} based on the wind factor ($|\boldsymbol{u}_i|/|\boldsymbol{u}_a|$). Points with a wind factor $\geq 2\%$ (defined as being in free drift) generally fall near the upper "free-drift limit" (as expected). This limit shows that in the absence of acceleration terms ($\boldsymbol{F}_a$), ice in free drift will amplify the efficiency of stress transfer compared to open water; however, as $\boldsymbol{F}_a$ also includes the Coriolis acceleration, $\boldsymbol{F}_a$ is non-zero even at steady-state. Points with wind factor below 2% cover a more broad range of values, but for low values (wind factor $\leq$ 1%), C_{equiv} are generally bounded by eq. (15b). This shows that, as expected, the ice interaction force $\boldsymbol{F}_i$ causes a reduction in momentum transfer relative to open-water conditions. Whether the net effect of the ice is to amplify or damp momentum transfer ultimately depends on the strength of this force.

Annual median values of C_{equiv} were similar for each of the three mooring locations with a slight north-south trend: 1.69×10^{-3}, 1.44×10^{-3}, 1.34×10^{-3} for SODA-A, -B, and -C, respectively. This similarity reflects that increased open-water areas (which have a lower efficiency of momentum transfer) at the southern moorings may partly offset expected increases in winter C_{equiv} due to free-drift conditions. However, because wind forcing also has strong seasonal variations with a winter maximum (e.g., Dosser & Rainville, 2016), long-term trends in the total momentum flux into the ocean ($\boldsymbol{\tau}_{ocn}$) will depend both on a balance of increasing open-water conditions and changing internal stress conditions in the winter.

Based on the 2%-rule, the wind factor ($|\boldsymbol{u}_i|/|\boldsymbol{u}_a|$) provides a first-order estimate of the extent of free drift conditions at each mooring. While only a rule-of-thumb, measured values of the wind factor showed asymptotic behaviour supporting use of this rule: as the wind speed increased (i.e., as $\boldsymbol{\tau}_{ai}$ becomes a dominant term in the force balance), wind factor values converged around 2%; bin-average values of the wind factor stay ap-

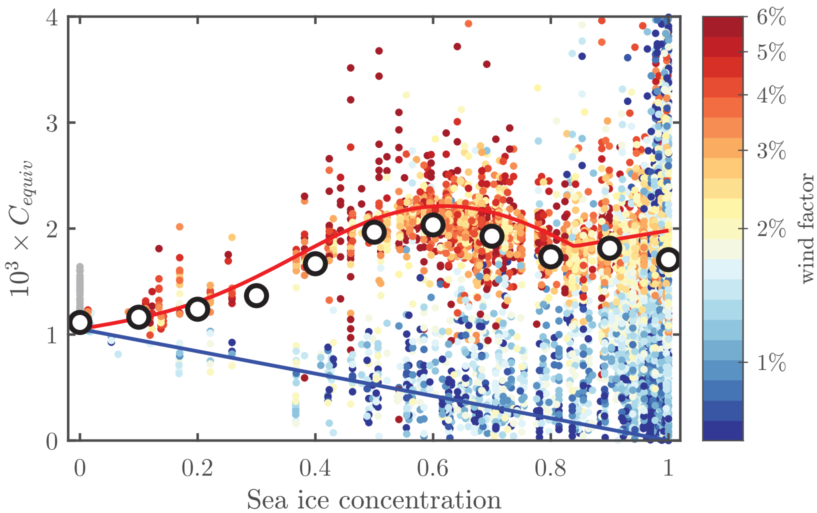

Figure 11: Equivalent drag coefficient C_{equiv} (eq. 7) as a function of sea ice concentration (from ERA5). Points shows all hourly values from all moorings, coloured by wind factor (log-scale; grey points had no measurable $\boldsymbol{u}_i$), while black circles show bin-median values by sea ice concentration. The red and blue lines shows the limit cases discussed in the text: red is eq. (15a); blue is eq. (15b).

proximately near 2% across a wide range of wind speeds (fig. 12a). There was also a relationship between wind factor and sea ice concentration: for concentrations below ∼80%–85%, the wind factor was elevated and generally greater than 2% (fig. 12b). This suggests that an 80%–85% ice-concentration-based limit for defining free drift is an approximation of the 2%-rule, but it may be the case that free drift conditions also occur intermittently for higher ice concentrations (e.g., on short timescales, atmospheric stress may be balanced primarily by only one of either the ice-ocean or ice-ice stresses, as in Steele et al., 1997). The prevalence of wind factor values greater than 2% have a north-south trend, with roughly 66% of measurements designated as being free drift at SODA-A, 54% at SODA-B, and 37% at SODA-C. Dosser and Rainville (2016) previously showed that the wind factor is a useful indicator for atmosphere-ice-ocean momentum transfer. If the differences between SODA-A and SODA-C are indicative of future trends of sea ice (in which more and more of the Arctic is similar to SODA-A) then this suggests the potential for increasing amplification of stress transfer from the atmosphere to the ocean in the Beaufort Sea during winter.

Martin et al. (2014, 2016) suggests that interplay between wind stress enhancement over sea ice and internal ice stresses (i.e., the relative sizes of $\boldsymbol{\tau}_{atm}$ and $\boldsymbol{F}_i$ in eq. 6) lead to a local maximum in the normalized $\boldsymbol{\tau}_{ocn}$ at some optimal sea ice concentration (their results suggest ∼80 % to 90 %). We see similar evidence for an optimal sea ice concentration in C_{equiv}; binned-median values of C_{equiv} have a peak near 60% ice concentration (fig. 11). However, our observations show that binned-median C_{equiv} roughly follow the free-drift limit (case 1), and there is not an appreciable decrease below that limit in median C_{equiv} at 100% ice concentration (which is in contrast to the pan-Arctic average results presented by Martin et al., 2014). This suggests that the optimal ice concentration for momentum transfer seen in our results is driven by the maximum of eq. (15a), and is minimally affected the ice interaction force ($\boldsymbol{F}_i$). As such, results for optimal ice concentration will be highly sensitive to the parameterization of C_{ia}. Furthermore, these results indicate that, on average, at all three moorings the presences of sea ice causes an amplification of stress transfer compared to open-water conditions for a given wind speed. This is consistent with Martin et al. (2016), who found that sea ice in the Beaufort Sea causes a mean amplification of stress into the ocean for all seasons regardless of whether a constant or variable ice-ocean drag coefficient was used in the model (see their figure 12).

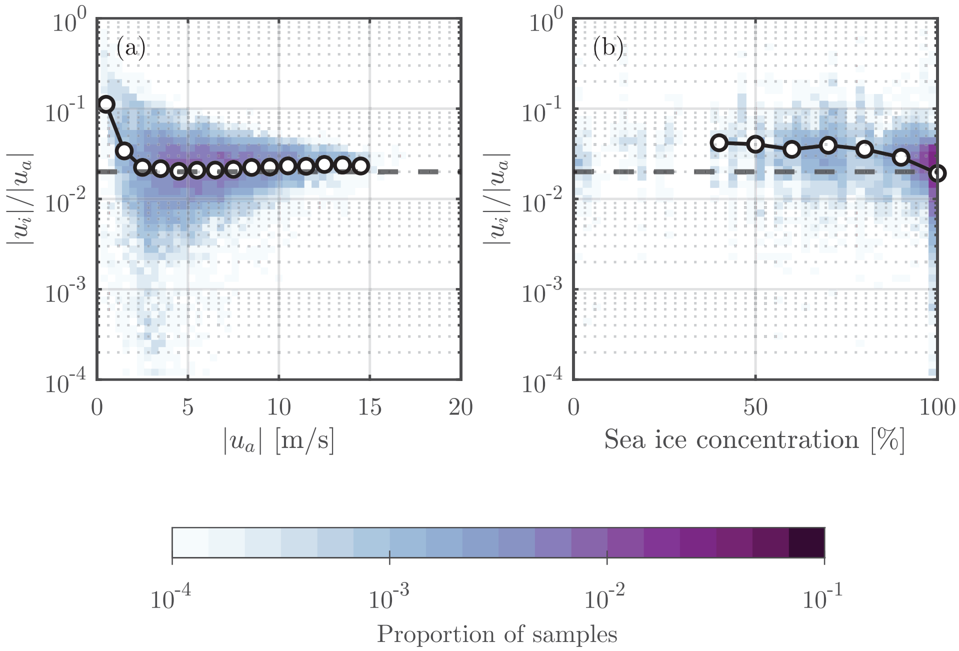

Figure 12: Wind factor ($|\boldsymbol{u}_i|/|\boldsymbol{u}_a|$) as a function of (a) wind speed, and (b) sea ice concentration (from ERA5). In both panels, shading shows a 2-dimensional histogram of the proportion of total samples (on a log-scale), while black lines with circles show the values of wind factor bin-averaged by (a) wind speed, and (b) sea ice concentration. Bin-averages in (b) were only produced for sea ice concentration ≥40% due to data scarcity for lower ice concentrations. The horizontal dashed black line in both panels corresponds to a wind factor of 2%.

6 Conclusions

Using a force-balance approach to estimate the ice ocean drag coefficient, C_{io}, the annual cycle of the efficiency of ice-ocean momentum transfer is inferred from mooring observations. These estimates compare favorably with drag coefficients using parameterization schemes, based on measured statistics of ice geometry, as well as with previous observations of ice-ocean drag. We summarize the main contributions of the study as follows:

1. The ice ocean drag coefficient, C_{io}, varied seasonally. Variations were more pronounced for the moorings in the seasonal ice zone compared to the mooring that was ice-covered through the full year (fig. 6), suggesting that the enhanced seasonality of the Arctic ice pack is directly influencing seasonality in C_{io}. This manifested as a decrease in C_{io} in the summer and fall, driven by changes in intensity of ridged ice (fig. 8). Wintertime mean values of C_{io} were similar to, or higher than, the canonical value of 5.5×10^{-3} (up to a maximum of 12.3×10^{-3}), but summer and fall values at SODA-A and -B (which may be more representative of future conditions) were as low as $\sim 1.3 \times 10^{-3}$ (fig. 10). The observed seasonality agrees with previous observational studies in the Western Arctic (Cole et al., 2017; Dewey, 2019), but contrast with pan-Arctic model results (Tsamados et al., 2014; Martin et al., 2016).
2. Geometry-based drag parameterizations reproduce many of the spatial and temporal variations of ice-ocean drag, provided that the ice geometry is known (figs. 6 and 7). Slight modifications to the existing parameterization schemes produces the most favourable results (T14(II); fig. 7c), but a full optimization of all free parameters has yet to be performed (and should account for non-neutral conditions and differences in boundary layer structure). Parameterization of the ice geometry (T14(III)) appears more challenging (fig. 7d), particularly predicting the correct floe sizes (impacting the total floe edge drag, figs. 8g to 8i). The mismatch in seasonality of ice-ocean drag between observations (Cole et al., 2017; Dewey, 2019, and the present study) and models (Tsamados et al., 2014; Martin et al., 2016) is likely a direct result of the difficulties in predicting floe aspect ratios using bulk parameters. Despite these challenges, the scheme that included ice ge-

ometry parameterization (T14(III)) still provided reasonably predictions of the ice-ocean drag prior to ice breakup in the spring/summer (fig. 6, red lines).

3. In the seasonal ice zone, ridging intensity grows relatively slowly compared to the growth of ice concentration (compare figs. 2d and 2e with fig. 5f). As a result, approaches for simplified ice concentration-based parameterization schemes that have been successful for calculating atmospheric drag (e.g., Andreas, Horst, et al., 2010; Andreas, Persson, et al., 2010) may not be the correct approach for drag at the ice-ocean interface. It is unlikely that schemes based solely on ice concentration will be able to adequately capture variations in ice-ocean drag during the ice growth season.
4. The presence of sea ice causes a net amplification of the efficiency of stress input to the ocean compared to open water (section 5.3) which we attribute to the prevalence of free drift conditions (including intermittently during full ice cover). Our measurements support the notion of an "optimal ice concentration" for momentum transfer (Martin et al., 2014, 2016), but suggest the value of the optimal concentration has high sensitivity to the parameterization of the atmosphere-ice drag coefficient, C_{ai} (fig. 11). A comparison between moorings indicates that free drift conditions are more common to the south, and thus may become more common throughout the Beaufort Sea in the future, with a net trend of amplified coupling between the atmosphere and the ocean.

The capability of models to represent the coupled atmosphere-ice-ocean system continues to evolve. Despite mismatches in predictions of ice geometry statistics which are used as inputs, the general success of the parameterization schemes described here gives greater confidence in our ability to use modelled results to learn about the "new Arctic", provided that methods can be developed to account for those mismatches. New sea-ice modelling schemes may be able to directly represent floe size distributions (Roach et al., 2018) or keel statistics (Roberts et al., 2019), reducing the need to redefine parameterizations of sea ice geometry. As model parameterizations of ice-ocean drag evolve, it will become important for users who apply those schemes to choose a framework that matches the model application, including an appropriate choice of reference depth, z_{ref}. For example, for an upper-ocean mixing study that uses $\boldsymbol{\tau}_{io}$ as a surface boundary condition it may be most appropriate to use a value of C_{io} consistent with drag at the base of the surface log-layer, or to choose z_{ref} in eq. (9) corresponding to the shallowest resolved ocean model level. Drag in a large-scale ice drift model driven by geostrophic ocean currents may be better described by Rossby Similarity Theory (Blackadar & Tennekes, 1968; McPhee, 2008) than by a quadratic drag law; though linking the "effective" roughness length used in that theory to statistics of large scale geometric features remains an open problem. Finally, differences between drag values measured at the different mooring sites indicates that variations in ice morphology may lead to large-scale spatial gradients in the ice-ocean drag, and consequently the surface momentum flux into the ocean, which may have important consequences for studies of large-scale Beaufort Sea circulation (e.g., gyre equilibrium and freshwater storage; Meneghello et al., 2018; Timmermans et al., 2018; Armitage et al., 2020).

Acknowledgments

This work was supported by the Office of Naval Research as part of the Stratified Ocean Dynamics of the Arctic (SODA) research project. Funding was through grant numbers N00014-16-1-2349, N00014-14-1-2377, N00014-18-1-2687. and N00014-16-1-2381. Data files containing the timeseries of the measurements and results described in this study, including sea ice momentum terms, sea ice geometry and ice-ocean drag coefficients, will be made available at `https://digital.lib.washington.edu/researchworks/handle/1773/15609`. More information about the project can be found at `www.apl.washington.edu/soda`. We thank Captain Greg Tlapa and Captain MaryEllen Durley, along with the rest of the command team and crew of USCGC Healy for operational support in 2018 and 2019. This work has benefited from ideas and feedback from members of the SODA project team and by two anonymous reviewers. We would also like to thank Sarah Dewey for helpful views and conversations.

References

Andreas, E. L. (2011). A relationship between the aerodynamic and physical roughness of winter sea ice. *Quarterly Journal of the Royal Meteorological Society*, *137*(659), 1581–1588. doi: 10.1002/qj.842

Andreas, E. L., Horst, T. W., Grachev, A. A., Persson, P. O. G., Fairall, C. W., Guest, P. S., & Jordan, R. E. (2010). Parametrizing turbulent exchange over summer sea ice and the marginal ice zone. *Quarterly Journal of the Royal Meteorological Society*, *136*(649), 927–943. doi: 10.1002/qj.618

Andreas, E. L., Persson, P. O. G., Grachev, A. A., Jordan, R. E., Horst, T. W., Guest, P. S., & Fairall, C. W. (2010). Parameterizing Turbulent Exchange over Sea Ice in Winter. *Journal of Hydrometeorology*, *11*(1), 87–104. doi: 10.1175/2009JHM1102.1

Armitage, T. W. K., Bacon, S., Ridout, A. L., Petty, A. A., Wolbach, S., & Tsamados, M. (2017). Arctic Ocean surface geostrophic circulation 2003-2014. *Cryosphere*, *11*(4), 1767–1780. doi: 10.5194/tc-11-1767-2017

Armitage, T. W. K., Manucharyan, G. E., Petty, A. A., Kwok, R., & Thompson, A. F. (2020). Enhanced eddy activity in the Beaufort Gyre in response to sea ice loss. *Nature Communications*, *11*(1), 761. doi: 10.1038/s41467-020-14449-z

Arya, S. P. S. (1975). A drag partition theory for determining the large-scale roughness parameter and wind stress on the Arctic pack ice. *Journal of Geophysical Research*, *80*(24), 3447–3454. doi: 10.1029/JC080i024p03447

Belliveau, D. J., Bugden, G. L., & Melrose, S. G. K. (1989). Measurement of sea ice motion using bottom mounted Acoustic Doppler Current Profilers. *Sea Technology*, *30*.

Bendat, J. S., & Piersol, A. G. (1971). *Random data: Analysis and measurement procedures*. New York: Wiley-Interscience.

Blackadar, A. K., & Tennekes, H. (1968). Asymptotic similarity in the neutral barotropic planetary boundary layer. *Journal of the Atmospheric Sciences*, *25*(6), 1015–1020. doi: 10.1175/1520-0469(1968)025⟨1015:ASINBP⟩2.0.CO;2

Brenner, S., Rainville, L., Thomson, J., & Lee, C. (2020). The evolution of a shallow front in the Arctic marginal ice zone. *Elementa: Science of the Anthropocene*, *8*(17), 17. doi: 10.1525/elementa.413

Castellani, G., Gerdes, R., Losch, M., & Lüpkes, C. (2015). Impact of Sea-Ice Bottom Topography on the Ekman Pumping. In G. Lohmann, H. Meggers, V. Unnithan, D. Wolf-Gladrow, J. Notholt, & A. Bracher (Eds.), *Towards an Interdisciplinary Approach in Earth System Science: Advances of a Helmholtz Graduate Research School* (pp. 139–148). Cham: Springer International Publishing. doi: 10.1007/978-3-319-13865-7_16

Castellani, G., Losch, M., Ungermann, M., & Gerdes, R. (2018). Sea-ice drag as a function of deformation and ice cover: Effects on simulated sea ice and ocean circulation in the Arctic. *Ocean Modelling*, *128*, 48–66. doi: 10.1016/j.ocemod.2018.06.002

Castellani, G., Lüpkes, C., Hendricks, S., & Gerdes, R. (2014). Variability of Arctic sea-ice topography and its impact on the atmospheric surface drag. *Journal of Geophysical Research: Oceans*, *119*(10), 6743–6762. doi: 10.1002/2013JC009712

Cole, S. T., Timmermans, M.-L., Toole, J. M., Krishfield, R. A., & Thwaites, F. T. (2014). Ekman Veering, Internal Waves, and Turbulence Observed under Arctic Sea Ice. *Journal of Physical Oceanography*, *44*(5), 1306–1328. doi: 10.1175/JPO-D-12-0191.1

Cole, S. T., Toole, J. M., Lele, R., Timmermans, M.-L., Gallaher, S. G., Stanton, T. P., ... Thomson, J. (2017). Ice and ocean velocity in the Arctic marginal ice zone: Ice roughness and momentum transfer. *Elementa: Science of the Anthropocene*, *5*, 55. doi: 10.1525/elementa.241

Connolley, W. M., Gregory, J. M., Hunke, E. C., & Mclaren, A. J. (2004). On the consistent scaling of terms in the sea-ice dynamics equation. *Journal of Physical Oceanography*, *34*, 5.

Davis, N. R., & Wadhams, P. (1995). A statistical analysis of Arctic pressure ridge morphology. *Journal of Geophysical Research*, *100*(C6), 10915. doi: 10.1029/95JC00007

Dewey, S. (2019). *Evolving ice-ocean dynamics of the western Arctic* (Unpublished doctoral dissertation). University of Washington.

Dewey, S., Morison, J., Kwok, R., Dickinson, S., Morison, D., & Andersen, R. (2018). Arctic ice-ocean coupling and gyre equilibration observed with remote sensing. *Geophysical Research Letters*, *45*(3), 1499–1508. doi: 10.1002/2017GL076229

Dosser, H. V., & Rainville, L. (2016). Dynamics of the Changing Near-Inertial Internal Wave Field in the Arctic Ocean. *Journal of Physical Oceanography*, *46*(2), 395–415. doi: 10.1175/JPO-D-15-0056.1

ECMWF. (2019). Part IV: Physical Processes. In *IFS Documentation CY46R1.* ECMWF.

Elvidge, A. D., Renfrew, I. A., Weiss, A. I., Brooks, I. M., Lachlan-Cope, T. A., & King, J. C. (2016). Observations of surface momentum exchange over the marginal ice zone and recommendations for its parametrisation. *Atmospheric Chemistry and Physics*, *16*(3), 1545–1563. doi: 10.5194/acp-16-1545-2016

Garbrecht, T., Lüpkes, C., Hartmann, J., & Wolff, M. (2002). Atmospheric drag coefficients over sea ice–validation of a parameterisation concept. *Tellus Series A: Dynamic Meteorology and Oceanography*, *54*(2), 205–219. doi: 10.3402/tellusa.v54i2.12129

Gelaro, R., McCarty, W., Suárez, M. J., Todling, R., Molod, A., Takacs, L., ... Zhao, B. (2017). The modern-era retrospective analysis for research and applications, version 2 (MERRA-2). *Journal of Climate*, *30*(14), 5419–5454. doi: 10.1175/JCLI-D-16-0758.1

Graham, R. M., Cohen, L., Ritzhaupt, N., Segger, B., Graversen, R. G., Rinke, A., ... Hudson, S. R. (2019). Evaluation of Six Atmospheric Reanalyses over Arctic Sea Ice from Winter to Early Summer. *Journal of Climate*, *32*(14), 4121–4143. doi: 10.1175/JCLI-D-18-0643.1

Guest, P. S., & Davidson, K. L. (1987). The effect of observed ice conditions on the drag coefficient in the summer East Greenland Sea Marginal Ice Zone. *Journal of Geophysical Research*, *92*(C7), 6943. doi: 10.1029/JC092iC07p06943

Guest, P. S., Glendening, J. W., & Davidson, K. L. (1995). An observational and numerical study of wind stress variations within marginal ice zones. *Journal of Geophysical Research*, *100*(C6), 10887. doi: 10.1029/94JC03391

Harding, S., Kilcher, L., & Thomson, J. (2017). Turbulence Measurements from Compliant Moorings. Part I: Motion Characterization. *Journal of Atmospheric and Oceanic Technology*, *34*(6), 1235–1247. doi: 10.1175/JTECH-D-16-0189.1

Heorton, H. D. B. S., Feltham, D. L., & Hunt, J. C. R. (2014). The response of the sea ice edge to atmospheric and oceanic jet formation. *Journal of Physical Oceanography*, *44*(9), 2292–2316. doi: 10.1175/JPO-D-13-0184.1

Heorton, H. D. B. S., Tsamados, M., Cole, S. T., Ferreira, A. M. G., Berbellini, A., Fox, M., & Armitage, T. W. K. (2019). Retrieving sea ice drag coefficients and turning angles from in situ and satellite observations using an inverse modeling framework. *Journal of Geophysical Research: Oceans*, *124*(8), 6388–6413. doi: 10.1029/2018JC014881

Hersbach, H., Bell, B., Berrisford, P., Hirahara, S., Horányi, A., Muñoz-Sabater, J., ... Thépaut, J.-N. (2020). The ERA5 global reanalysis. *Quarterly Journal of* *the Royal Meteorological Society*, *146*(730), 1999–2049. doi: 10.1002/qj.3803

Hibler, W. D., Weeks, W. F., & Mock, S. J. (1972). Statistical aspects of sea-ice ridge distributions. *Journal of Geophysical Research*, *77*(30), 5954–5970. doi: 10.1029/JC077i030p05954

Holton, J. R. (2004). *An introduction to dynamic meteorology* (4th ed ed.) (No. v. 88). Burlington, MA: Elsevier Academic Press.

Horvat, C., & Tziperman, E. (2017). The evolution of scaling laws in the sea ice floe size distribution. *Journal of Geophysical Research: Oceans*, *122*(9), 7630–7650. doi: 10.1002/2016JC012573

Huber, P. J. (1981). *Robust statistics*. John Wiley & Sons.

Hunke, E. C. (2010). Thickness sensitivities in the CICE sea ice model. *Ocean Modelling*, *34*(3), 137–149. doi: 10.1016/j.ocemod.2010.05.004

Hunke, E. C., Allard, R., Bailey, D. A., Blain, P., Craig, A., Dupont, F., ... Winton, M. (2020). *CICE-Consortium/CICE: CICE Version 6.1.2*. Zenodo. doi: 10.5281/zenodo.3888653

Hunke, E. C., & Dukowicz, J. K. (2003). *The sea ice momentum equation in the free drift regime* (Tech. Rep. No. LA-UR-03-2219). Los Alamos, New Mexico, US: Los Alamos National Laboratory.

Hunkins, K. (1966). Ekman drift currents in the Arctic Ocean. *Deep Sea Research and Oceanographic Abstracts*, *13*(4), 607–620. doi: 10.1016/0011-7471(66)90592-4

Ivanov, V., Alexeev, V., Koldunov, N. V., Repina, I., Sandø, A. B., Smedsrud, L. H., & Smirnov, A. (2016). Arctic Ocean Heat Impact on Regional Ice Decay: A Suggested Positive Feedback. *Journal of Physical Oceanography*, *46*(5), 1437–1456. doi: 10.1175/JPO-D-15-0144.1

Jackson, J. M., Allen, S. E., McLaughlin, F. A., Woodgate, R. A., & Carmack, E. C. (2011). Changes to the near-surface waters in the Canada Basin, Arctic Ocean from 1993–2009: A basin in transition. *Journal of Geophysical Research: Oceans*, *116*(C10). doi: 10.1029/2011JC007069

Johannessen, O. M. (1970). Note on some vertical profiles below ice floes in the Gulf of St. Lawrence and near the North Pole. *Journal of Geophysical Research*, *75*(15), 2857–2861. doi: 10.1029/JC075i015p02857

Kim, J. G., Hunke, E. C., & Lipscomb, W. H. (2006). Sensitivity analysis and parameter tuning scheme for global sea-ice modeling. *Ocean Modelling*, *14*(1), 61–80. doi: 10.1016/j.ocemod.2006.03.003

Kim, T. W., Ha, H. K., Wåhlin, A. K., Lee, S. H., Kim, C. S., Lee, J. H., & Cho, Y. K. (2017). Is Ekman pumping responsible for the seasonal variation of warm circumpolar deep water in the Amundsen Sea? *Continental Shelf Research*, *132*, 38–48. doi: 10.1016/j.csr.2016.09.005

Kirillov, S., Babb, D., Dmitrenko, I., Landy, J., Lukovich, J., Ehn, J., ... Stroeve, J. (2020). Atmospheric forcing drives the winter sea ice thickness asymmetry of Hudson Bay. *Journal of Geophysical Research: Oceans*, *125*(2). doi: 10.1029/2019JC015756

Kobayashi, S., Ota, Y., Harada, Y., Ebita, A., Moriya, M., Onoda, H., ... Takahashi, K. (2015). The JRA-55 Reanalysis: General Specifications and Basic Characteristics. *Journal of the Meteorological Society of Japan. Ser. II*, *93*(1), 5–48. doi: 10.2151/jmsj.2015-001

Köberle, C., & Gerdes, R. (2003). Mechanisms Determining the Variability of Arctic Sea Ice Conditions and Export. *Journal of Climate*, *16*(17), 2843–2858. doi: 10.1175/1520-0442(2003)016⟨2843:MDTVOA⟩2.0.CO;2

Krishfield, R. A., Proshutinsky, A., Tateyama, K., Williams, W. J., Carmack, E. C., McLaughlin, F. A., & Timmermans, M.-L. (2014). Deterioration of perennial sea ice in the Beaufort Gyre from 2003 to 2012 and its impact on the oceanic freshwater cycle. *Journal of Geophysical Research: Oceans*, *119*(2), 1271–1305. doi: 10.1002/2013JC008999

Large, W. G., & Yeager, S. G. (2004). *Diurnal to decadal global forcing for ocean and sea-ice models: The data sets and flux climatologies* (Technical Note Nos. NCAR/TN-460+STR). Boulder Colorado: National Center for Atmospheric Research.

Leppäranta, M. (2011). *The drift of sea ice* (M. Leppäranta, Ed.). Berlin, Heidelberg: Springer. doi: 10.1007/978-3-642-04683-4_2

Losch, M., Menemenlis, D., Campin, J.-M., Heimbach, P., & Hill, C. (2010). On the formulation of sea-ice models. Part 1: Effects of different solver implementations and parameterizations. *Ocean Modelling*, *33*(1-2), 129–144. doi: 10.1016/j.ocemod.2009.12.008

Lu, P., Li, Z., Cheng, B., & Leppäranta, M. (2011). A parameterization of the ice-ocean drag coefficient. *Journal of Geophysical Research*, *116*(C7), C07019. doi: 10.1029/2010JC006878

Lüpkes, C., & Birnbaum, G. (2005). Surface drag in the Arctic marginal sea-ice zone: A comparison of different parameterisation concepts. *Boundary-Layer Meteorology*, *117*(2), 179–211. doi: 10.1007/s10546-005-1445-8

Lüpkes, C., & Gryanik, V. M. (2015). A stability-dependent parametrization of transfer coefficients for momentum and heat over polar sea ice to be used in climate models. *Journal of Geophysical Research: Atmospheres*, *120*(2), 552–581. doi: 10.1002/2014JD022418

Lüpkes, C., Gryanik, V. M., Hartmann, J., & Andreas, E. L. (2012). A parametrization, based on sea ice morphology, of the neutral atmospheric drag coefficients for weather prediction and climate models. *Journal of Geophysical Research: Atmospheres*, *117*(D13), n/a-n/a. doi: 10.1029/2012JD017630

Lüpkes, C., Gryanik, V. M., Rösel, A., Birnbaum, G., & Kaleschke, L. (2013). Effect of sea ice morphology during Arctic summer on atmospheric drag coefficients used in climate models. *Geophysical Research Letters*, *40*(2), 446–451. doi: 10.1002/grl.50081

Magnell, B., Ivanov, L., & Siegel, E. (2010). Measurements of ice parameters in the Beaufort Sea using the Nortek AWAC acoustic Doppler current profiler. In *OCEANS 2010 MTS/IEEE SEATTLE* (pp. 1–8). doi: 10.1109/OCEANS.2010.5664016

Martin, T. (2007). *Arctic sea ice dynamics: Drift and ridging in numerical models and observations* (Unpublished doctoral dissertation). University of Bremen.

Martin, T., Steele, M., & Zhang, J. (2014). Seasonality and long-term trend of Arctic Ocean surface stress in a model. *Journal of Geophysical Research: Oceans*, *119*(3), 1723–1738. doi: 10.1002/2013JC009425

Martin, T., Tsamados, M., Schroeder, D., & Feltham, D. L. (2016). The impact of variable sea ice roughness on changes in Arctic Ocean surface stress: A model study. *Journal of Geophysical Research: Oceans*, *121*(3), 1931–1952. doi: 10.1002/2015JC011186

Maykut, G. A., & Untersteiner, N. (1971). Some results from a time-dependent thermodynamic model of sea ice. *Journal of Geophysical Research*, *76*(6), 1550–1575. doi: 10.1029/JC076i006p01550

McPhee, M. G. (1979). The Effect of the Oceanic Boundary Layer on the Mean Drift of Pack Ice: Application of a Simple Model. *Journal of Physical Oceanography*, *9*(2), 388–400. doi: 10.1175/1520-0485(1979)009⟨0388:TEOTOB⟩2.0.CO;2

McPhee, M. G. (1980). An analysis of pack ice drift in summer. *Sea ice processes and models*, 62–75.

McPhee, M. G. (2002). Turbulent stress at the ice/ocean interface and bottom surface hydraulic roughness during the SHEBA drift. *Journal of Geophysical Research*, *107*(C10), 8037. doi: 10.1029/2000JC000633

McPhee, M. G. (2008). *Air-ice-ocean interaction: Turbulent ocean boundary layer exchange processes*. New York: Springer-Verlag. doi: 10.1007/978-0-387-78335-2

McPhee, M. G. (2012). Advances in understanding ice–ocean stress during and since AIDJEX. *Cold Regions Science and Technology*, *76-77*, 24–36. doi: 10.1016/j.coldregions.2011.05.001

McPhee, M. G., & Kantha, L. H. (1989). Generation of internal waves by sea ice. *Journal of Geophysical Research*, *94*(C3), 3287. doi: 10.1029/JC094iC03p03287

McPhee, M. G., Kottmeier, C., & Morison, J. H. (1999). Ocean Heat Flux in the Central Weddell Sea during Winter. *Journal of Physical Oceanography*, *29*(6), 1166–1179. doi: 10.1175/1520-0485(1999)029⟨1166:OHFITC⟩2.0.CO;2

Meneghello, G., Marshall, J., Campin, J.-M., Doddridge, E., & Timmermans, M.-L. (2018). The Ice-Ocean Governor: Ice-Ocean Stress Feedback Limits Beaufort Gyre Spin-Up. *Geophysical Research Letters*, *45*(20), 11,293–11,299. doi: 10.1029/2018GL080171

Monin, A. S., & Obukhov, A. M. (1954). Basic laws of turbulent mixing in the surface layer of the atmosphere. *Trudy Geofiz. Inst. Akad. Nauk SSSR*, *24*(151), 163–187.

Morison, J. H., McPhee, M. G., & Maykut, G. A. (1987). Boundary layer, upper ocean, and ice observations in the Greenland Sea Marginal Ice Zone. *Journal of Geophysical Research: Oceans*, *92*(C7), 6987–7011. doi: 10.1029/JC092iC07p06987

Park, H.-S., & Stewart, A. L. (2016). An analytical model for wind-driven Arctic summer sea ice drift. *Cryosphere*, *10*(1), 227–244. doi: 10.5194/tc-10-227-2016

Perrie, W., & Hu, Y. (1997). Air–ice–ocean momentum exchange. Part II: Ice drift. *Journal of Physical Oceanography*, *27*, 21.

Petty, A. A., Tsamados, M. C., & Kurtz, N. T. (2017). Atmospheric form drag coefficients over Arctic sea ice using remotely sensed ice topography data, spring 2009-2015. *Journal of Geophysical Research: Earth Surface*, *122*(8), 1472–1490. doi: 10.1002/2017JF004209

Phillips, O. M. (1985). Spectral and statistical properties of the equilibrium range in wind-generated gravity waves. *Journal of Fluid Mechanics*, *156*(-1), 505. doi: 10.1017/S0022112085002221

Pite, H. D., Topham, D. R., & van Hardenberg, B. J. (1995). Laboratory measurements of the drag force on a family of two-dimensional ice keel models in a two-layer flow. *Journal of Physical Oceanography*, *25*(12), 3008–3031. doi: 10.1175/1520-0485(1995)025⟨3008:LMOTDF⟩2.0.CO;2

Plueddemann, A. J., Krishfield, R., Takizawa, T., Hatakeyama, K., & Honjo, S. (1998). Upper ocean velocities in the Beaufort Gyre. *Geophysical Research Letters*, *25*(2), 183–186. doi: 10.1029/97GL53638

Rainville, L., Lee, C., & Woodgate, R. A. (2011). Impact of wind-driven mixing in the Arctic Ocean. *Oceanography*, *24*(3), 136–145.

Rainville, L., & Woodgate, R. A. (2009). Observations of internal wave generation in the seasonally ice-free Arctic. *Geophysical Research Letters*, *36*(23), L23604. doi: 10.1029/2009GL041291

Rampal, P., Bouillon, S., Ólason, E., & Morlighem, M. (2016). NeXtSIM: A new Lagrangian sea ice model. *Cryosphere*, *10*(3), 1055–1073. doi: 10.5194/tc-10-1055-2016

Randelhoff, A., Sundfjord, A., & Renner, A. H. H. (2014). Effects of a shallow pycnocline and surface meltwater on sea ice–ocean drag and turbulent heat flux. *Journal of Physical Oceanography*, *44*(8), 2176–2190. doi: 10.1175/JPO-D-13-0231.1

Roach, L. A., Horvat, C., Dean, S. M., & Bitz, C. M. (2018). An Emergent Sea Ice Floe Size Distribution in a Global Coupled Ocean-Sea Ice Model. *Journal of Geophysical Research: Oceans*, *123*(6), 4322–4337. doi:

10.1029/2017JC013692

Roberts, A. F., Hunke, E. C., Kamal, S. M., Lipscomb, W. H., Horvat, C., & Maslowski, W. (2019). A variational method for sea ice ridging in earth system models. *Journal of Advances in Modeling Earth Systems*, *11*(3), 771–805. doi: 10.1029/2018MS001395

Rousset, C., Vancoppenolle, M., Madec, G., Fichefet, T., Flavoni, S., Barthélemy, A., ... Vivier, F. (2015). The Louvain-La-Neuve sea ice model LIM3.6: Global and regional capabilities. *Geoscientific Model Development*, *8*, 2991–3005. doi: 10.5194/gmd-8-2991-2015

Shaw, W. J., Stanton, T. P., McPhee, M. G., & Kikuchi, T. (2008). Estimates of surface roughness length in heterogeneous under-ice boundary layers. *Journal of Geophysical Research*, *113*(C8), C08030. doi: 10.1029/2007JC004550

Shcherbina, A., D'Asaro, E. A., Light, B., Deming, J. W., & Rehm, E. (2016). *Maiden Voyage of the Under-Ice Float.*

Shirasawa, K., & Ingram, R. G. (1991). Characteristics of the turbulent oceanic boundary layer under sea ice. Part 1: A review of the ice-ocean boundary layer. *Journal of Marine Systems*, *2*(1), 153–160. doi: 10.1016/0924-7963(91)90021-L

Shirasawa, K., Ingram, R. G., & Aota, M. (1989). Measurements in the boundary layer under landfast ice in the southeast Hudson Bay, Canada. *Low Temperature Science*, *A*(47), 213–221.

Spreen, G., Kaleschke, L., & Heygster, G. (2008). Sea ice remote sensing using AMSR-E 89-GHz channels. *Journal of Geophysical Research: Oceans*, *113*(C2). doi: 10.1029/2005JC003384

Steele, M., Morison, J. H., & Untersteiner, N. (1989). The partition of air-ice-ocean momentum exchange as a function of ice concentration, floe size, and draft. *Journal of Geophysical Research*, *94*(C9), 12739. doi: 10.1029/JC094iC09p12739

Steele, M., Zhang, J., Rothrock, D., & Stern, H. (1997). The force balance of sea ice in a numerical model of the Arctic Ocean. *Journal of Geophysical Research: Oceans*, *102*(C9), 21061–21079. doi: 10.1029/97JC01454

Steiner, N. (2001). Introduction of variable drag coefficients into sea-ice models. *Annals of Glaciology*, *33*, 181–186. doi: 10.3189/172756401781818149

Stern, H. L., Schweiger, A. J., Zhang, J., & Steele, M. (2018). On reconciling disparate studies of the sea-ice floe size distribution. *Elementa: Science of the Anthropocene*, *6*(1), 49. doi: 10.1525/elementa.304

Stroeve, J., & Notz, D. (2018). Changing state of Arctic sea ice across all seasons. *Environmental Research Letters*, *13*(10), 103001. doi: 10.1088/1748-9326/aade56

Thomson, J., Lund, B., Hargrove, J., Smith, M. M., Horstmann, J., & MacKinnon, J. A. (2021). Wave-driven flow along a compact marginal ice zone. *Geophysical Research Letters*. doi: 10.1029/2020GL090735

Timco, G., & Burden, R. (1997). An analysis of the shapes of sea ice ridges. *Cold Regions Science and Technology*, *25*(1), 65–77. doi: 10.1016/S0165-232X(96)00017-1

Timmermann, R., Danilov, S., Schröter, J., Böning, C., Sidorenko, D., & Rollenhagen, K. (2009). Ocean circulation and sea ice distribution in a finite element global sea ice–ocean model. *Ocean Modelling*, *27*(3-4), 114–129. doi: 10.1016/j.ocemod.2008.10.009

Timmermans, M.-L., Toole, J., & Krishfield, R. (2018). Warming of the interior Arctic Ocean linked to sea ice losses at the basin margins. *Science Advances*, *4*(8), eaat6773. doi: 10.1126/sciadv.aat6773

Tsamados, M., Feltham, D. L., Schroeder, D., Flocco, D., Farrell, S. L., Kurtz, N., … Bacon, S. (2014). Impact of variable atmospheric and oceanic form drag on simulations of Arctic sea ice. *Journal of Physical Oceanography*, *44*(5), 1329–1353. doi: 10.1175/JPO-D-13-0215.1

Wadhams, P., & Davy, T. (1986). On the spacing and draft distributions for pressure ridge keels. *Journal of Geophysical Research*, *91*(C9), 10697. doi: 10.1029/JC091iC09p10697

Wadhams, P., & Horne, R. J. (1980). An Analysis Of Ice Profiles Obtained By Submarine Sonar In The Beaufort Sea. *Journal of Glaciology*, *25*(93), 401–424. doi: 10.3189/S0022143000015264

Weiss, J., & Marsan, D. (2004). Scale properties of sea ice deformation and fracturing. *Comptes Rendus Physique*, *5*(7), 735–751. doi: 10.1016/j.crhy.2004.09.005

Williams, E., Swithinbank, C., & Robin, G. d. Q. (1975). A submarine sonar study of Arctic pack ice. *Journal of Glaciology*, *15*(73), 349–362. doi: 10.3189/S002214300003447X

Zu, Y., Lu, P., Lepparanta, M., Cheng, B., & Li, Z. (2020). *On the form drag coefficient under ridged ice: Laboratory experiments and numerical simulations from ideal scaling to real ice conditions* [Preprint]. doi: 10.1002/essoar.10504763.1

Meltwater Advection Hastens Autumn Freeze Up

Laura Crews[1,2], Craig M. Lee[2], Luc Rainville[2], and Jim Thomson[2]

[1]School of Oceanography, University of Washington, Seattle, WA, USA [2]Applied Physics Laboratory, University of Washington, Seattle, WA, USA

Corresponding author: Laura Crews (lcrews@uw.edu)

Key Points:

- High spatial and temporal resolution observations in the ice-free Beaufort Sea show advected meltwater hastened freeze up by several days
- Meltwater advection caused nearly as much mixed layer heat loss as was caused by seasonally integrated heat loss to the atmosphere
- These results mean freeze up forecasting should consider the three-dimensional evolution of mixed layer temperature and depth

Abstract

In seasonally ice-free parts of the Arctic Ocean, autumn is characterized by heat loss from the upper ocean to the atmosphere and the onset of freeze up, in which first year sea ice begins to grow in open water areas. The timing of freeze up can be highly spatially variable, complicating efforts to provide accurate sea ice forecasting for marine operations. While melt season anomalies can be used to predict freeze up anomalies in some parts of the Arctic, this one-dimensional view merits further examination in light of recent work demonstrating the importance of three-dimensional flows in setting mixed layer properties in marginal ice zones. In this study we show that horizontal advection of sea ice meltwater hastens freeze up in areas distant from the ice edge. We use nearly 800 temperature and salinity profiles along with satellite imagery collected in the central Beaufort Sea in autumn 2018 to document the roughly 100 km advection of a cold and fresh surface meltwater layer over several weeks. This advected meltwater hastened freeze by cooling and shoaling the mixed layer relative to adjacent areas unaffected by the meltwater. A mixed layer heat budget showed that advection was nearly as important as one-dimensional heat loss to the atmosphere for seasonally integrated mixed layer heat loss within the meltwater-affected area.

Plain Language Summary

In large parts of the Arctic Ocean, sea ice melts completely in summer and reforms in autumn in a process known as “freeze up”. The timing of freeze up may affect energy exchanges between the ocean and atmosphere, such as occur during storms, as well as impact the sea ice ecosystem. Warming ocean temperatures mean freeze up is occurring later, lengthening the season in which non-ice-rated vessels can engage in operations like shipping, resource extraction, and supplying local communities with fuel and cargo. Accurate freeze up forecasting helps ensure these operations are conducted safely. This study uses ocean temperature and salinity data from autonomous vehicles as well as data from satellites to demonstrate how areas that were affected by recent sea ice melt can freeze up early. We observe a cold and fresh footprint of meltwater near sea ice in the Beaufort Sea that flowed away from its original location and altered the upper ocean in neighboring areas. A simple model that simulates the atmosphere’s influence on the ocean demonstrates that this meltwater caused the ocean to freeze

several days earlier than it otherwise would have by cooling the upper ocean and limiting the depth of ocean mixing.

1 Introduction

The autumn ice advance date, on which the sea ice area begins to expand in seasonally ice-free seas, is occurring later throughout the Arctic Ocean (Stroeve et al., 2014; Thomson et al., 2016), with the most pronounced shift in phenology found in the Chukchi and Beaufort Seas (Thomson et al., 2016). Later freeze up is due to warmer sea surface temperatures, which are caused by increased solar absorption throughout the summer (Stroeve et al., 2014). The autumn cooling period is characterized by net heat fluxes from the ocean to the atmosphere which cool the ocean mixed layer toward the freezing temperature, a prerequisite for ice formation. However, freeze up timing can be patchy on smaller spatial scales than those over which the atmospheric forcing is expected to vary, pointing to the importance of ocean processes in generating freeze up timing variability on these smaller scales (Figure 1).

The timing of freeze up is important for several reasons. First, ice inhibits heat exchange between the ocean and atmosphere once it develops sufficient thickness (e.g., Maykut, 1978), so earlier or later ice formation would be expected to limit or extend the period in which meaningful heat exchange can occur. In addition, the timing of freeze up matters because the presence of ice alters the efficiency of atmosphere-ocean momentum transfer (e.g., Brenner et al., 2021) and air-sea gas exchange (Islam et al., 2017). Furthermore, the abundance of protists incorporated into sea ice decreases with later freeze up, which in turn decreases ice protist abundance at the beginning of the spring bloom (Niemi et al., 2011). Finally, accurate freeze up forecasting at operational timescales is essential for vessels to safely navigate these waters.

The mixed layer of the Beaufort Sea at the end of summer is shallow, fresh and stratified primarily due to ice melt, and warm due to solar heating (Toole et al., 2010; Jackson et al., 2010). The continuous effect of cooling and freshening associated with summer ice melt competes with the solar heating, which can result in a temperature maximum below the mixed layer (NSTM, Steele et al., 2010; Jackson et al., 2010). Beneath the NSTM is a temperature minimum marking the remainder of the previous winter's mixed layer (Jackson et al., 2010). Below this minimum are the warm Pacific Summer Water layer, the cold Pacific Winter Water layer, and the warm Atlantic Water layer, all of which were advected from Arctic Ocean boundaries. These boundary-derived layers do not typically influence the surface in the Beaufort Sea on seasonal timescales because of the strong near-surface stratification (Toole et al., 2010).

Studies of upper ocean processes in the Arctic often emphasize one-dimensional mixed layer evolution forced by momentum and buoyancy exchanges with the overlying sea ice or atmosphere (e.g., Toole et al., 2010; Dewey et al., 2017). However, mixed layer instabilities at submesoscale fronts have been shown to play a significant role in setting ocean mixed layer properties (e.g., Boccaletti et al., 2007; Thomas et al., 2008). In the Beaufort Sea, restratification under sea ice was not replicated by a one-dimensional model (Toole et al., 2010), and Timmermans et al. (2012) argue that this restratification was likely caused by submesoscale processes on the basis of frontal structure observations and O(1) balanced Richardson number estimates.

Subsequent observations and modeling studies have shown that submesoscale fronts are found in marginal ice zones (MIZs) where surface freshening due to ice melt causes strong horizontal surface buoyancy gradients over length scales of 1–10 km (e.g., Brenner et al., 2020; Horvat el al., 2016; Lu et al., 2015; Manucharyan and Thompson, 2017). Fronts in the Arctic are also found at the confluence of different watermasses, for example in Fram Strait (von Appen et al., 2018), or river plumes (Macdonald et al., 1995; Alkire et al., 2019). Observations demonstrate an active submesoscale field in the Beaufort Sea (Mensa et al., 2018), in the neighboring Chukchi Sea (Timmermans and Windsor, 2013), as well as in Fram Strait (von Appen et al., 2018).

Basin-scale observations in the Beaufort Sea indicate that month-to-month changes in mixed layer temperature and salinity are largely due to one-dimensional processes (Dewey et al., 2017). Here we expand on this regionally one-dimensional view using mesoscale-resolving observations of ocean temperature and salinity in the weeks preceding freeze up. We find that the horizontal advection of a shallow meltwater front cooled and restratified the mixed layer. These lateral effects allowed freeze up to occur earlier in the meltwater than in adjacent waters, highlighting an important consequence of mixed layer heterogeneity and three-dimensional processes.

This study is organized as follows. Section 2 outlines the ocean observations and remote sensing products used in this study. Section 3 describes the meltwater and its advection. Section

4 develops a mixed layer heat budget to quantify the importance of meltwater advection to mixed layer heat loss. Section 5 describes an additional instance of freshwater advection and its effect on freeze up. Section 6 summarizes and discusses the results.

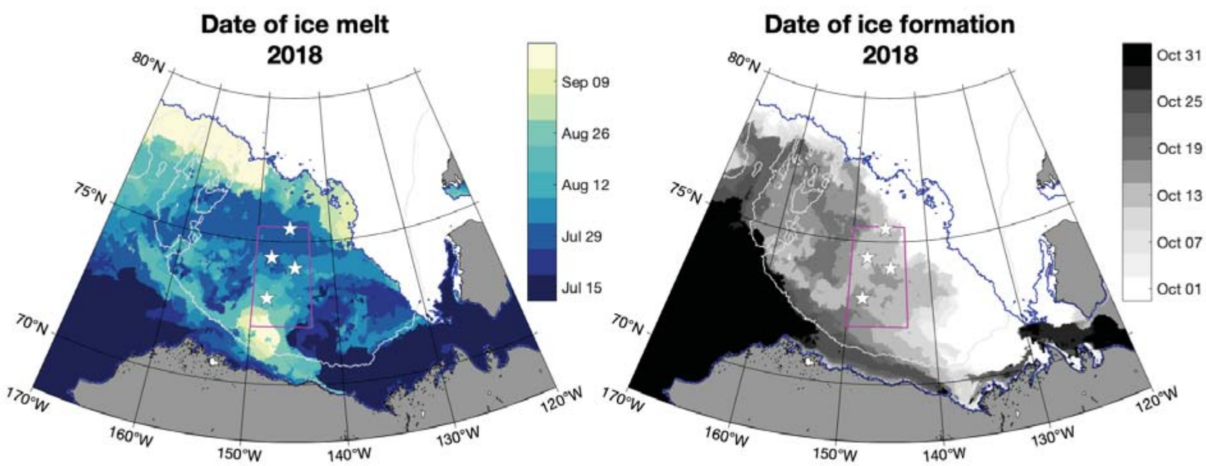

Figure 1 *Spatial variability of (left) melt out and (right) freeze up dates in the Beaufort Sea in 2018. Ice retreat was defined as the first day AMSR2 ice concentration fell below 0.15 for three consecutive days and freeze up was defined as the first day AMSR2 ice concentration exceeded 0.15 for three consecutive days. Ice never retreated in the area bounded by the blue contour. Solid gray regions delineate landmasses, light gray contours mark the 1000-m isobath, and white stars indicate mooring locations. The pink box marks the region depicted in Figure 2.*

2 Methods

2.1 Overview

This study uses observations collected in the Beaufort Sea in September to October 2018, as part of the Stratified Ocean Dynamics of the Arctic (SODA) experiment, to investigate mechanisms that drive freeze up heterogeneity. The SODA experiment, sponsored by the U.S. Office of Naval Research, aims at understanding stratification changes in the Arctic Ocean and includes many other components (Lee et al., 2016; Rainville et al., 2020). The upper ocean's evolution was documented by mesoscale-resolving upper ocean temperature and salinity profiles from four autonomous Seagliders. The persistent Seaglider sampling was supplemented by episodic sampling from four Wave Gliders and a ship-based profiler (Underway CTD). The locations of these measurements are shown in Figure 2. Additional context was provided by remote sensing products and a one-dimensional mixed layer model.

2.2 Upper ocean temperature and salinity observations

2.2.1 Seagliders

Seaglider autonomous vehicles sampled ocean temperature and salinity between the surface and 1000 m. Seagliders employ a saw-tooth dive pattern with approximately 5 km horizontal spacing between profiles at the surface. Temperature and salinity data were averaged into 1-m depth bins and profiles lacking data above 15 m were not used. If the remaining temperature or salinity profiles did not extend to the surface, the shallowest measured temperature or salinity was extrapolated as a constant value to the surface because we assume that these depths were well mixed.

Five Seagliders were deployed in open water on 21 September; two of these were recovered after a few days due to technical issues. The three remaining Seagliders sampled two quasi-parallel transects. Each transect was sampled by Seagliders operating in tandem, with one or two Seagliders traversing half a transect. This sampling strategy provided complete occupation of the transect at a timescale of a few days. Data used in this study span 21 September to 15 October, with the end of the study period characterized by active freeze up (Figure 1). Two Seagliders continued sampling intermittently after freeze up and were lost in the ice while trying to overwinter, returning data from as late as February 2019. During the study period, one of the Seagliders made a one-time excursion north of the sampling transect to assess conditions near the MIZ. Sampling by an additional Seaglider away from the main Seaglider transects occurred on 26 September.

2.2.2 Wave Gliders

Four Liquid Robotics SV-2 Wave Gliders sampled near 73°N 147°W from 19–23 September as part of the SODA Alaska North Slope process study (MacKinnon et al., 2021). The Wave Gliders sampled temperature, conductivity, and pressure at approximately 1-km horizontal resolution using Sea-Bird “Glider Payload” CTDs. The nominal measurement depths varied by vehicle; the most common configuration was temperature sampling at 0.2 m and 9 m as well as conductivity sampling at 9 m. One vehicle also measured conductivity at 0.2 m, using an

Aanderraa 4319B sensor. The exact depth varied slightly for each measurement as the vehicle moved.

2.2.3 Ship-based measurements

Temperature and salinity profiles were collected by an underway CTD (uCTD) at approximately 1 km horizontal spacing on 13 October. The uCTD recovery line was routed through the extended arm of USCGC *Healy*'s starboard crane to minimize sampling in the ship's wake. The uCTD was deployed in "tow-yo mode", meaning it was not recovered between casts, and data above 1 m were excluded to eliminate errors associated with identifying the start of the cast. Data from the down cast were used and sampling depths were determined by the probe's freefall time and the ship's speed; casts were typically to 130–160 m with maximum cast depths of about 180 m.

Near-surface ocean temperature and salinity were also collected by *Healy* while underway. The seawater intake was 2.7 m below the ship's waterline. Underway salinity data are known to drift over time due to biofouling of the conductivity cell (Alory et al., 2015) and temperature data are biased because seawater warms while traveling through the ship system before its temperature is measured (Alory et al., 2015). To correct the underway data, we computed the difference between uCTD temperature and salinity profiles averaged in the upper five meters and concurrent underway data. The underway data used in the comparison was the median value in one-hour windows centered on the times of the uCTD profiles. To correct underway salinity, a linear fit of the differences between the uCTD salinity and co-located underway salinity was used to compute a continuous correction time series that was added to the underway salinity (Alory et al., 2015). To correct underway temperature, the median difference between the uCTD temperature and co-located underway temperature (−1.3°C) was added to the underway temperature.

2.3 Mixing layer and mixed layer definitions

Using data collected from Ice-Tethered Profilers, Timmermans et al. (2012) distinguished between the Beaufort Sea surface layer, defined as a density change of 0.25 kg/m^3 relative to the shallowest measurement, and the actively mixing layer, defined as a density change of 0.01 kg/m^3 relative to the shallowest measurement. They found that mixing layers were common and attributed them to lateral restratification. Inspection of the density profiles in this study showed that mixing layers were common in open water as well, so we defined the mixing layer using a density change of 0.01 kg/m^3 and the mixed layer using a density change of 0.25 kg/m^3 (a scheme also used in Cole et al., 2014).

2.4 Ocean heat content

Ocean heat loss was quantified by calculating the change with time in ocean heat content. The ocean heat content was calculated from each temperature profile as

$$HC = \int_{h}^{0} c_p \, \rho \, (T(z) - T_{fr}(z)) \, dz$$

where ρ is the measured potential density, c_p is the heat capacity, and T_{fr} is the freezing temperature calculated from the in situ salinity and pressure. Section 2.2.1 stated that missing surface data in the measured temperature profile *T(z)* were filled with a constant value, but this interpolation is not expected to impact the results related to ocean heat content as it only affected two profiles used in the heat content analysis (Section 4; the shallowest available measurements were at 2 m and 3 m). Heat was integrated using the trapezoidal method from the surface to the depth *h*. In this paper we will discuss the mixed layer heat content, for which *h* is the depth at which density increased by 0.25 kg/m^3 relative to the surface, as well as the upper ocean heat including for which *h* is a specified constant depth.

2.5 Remote sensing

MODIS-Terra Nighttime sea surface temperature (SST) 8-day composite images were used to supplement in situ ocean temperature observations. Only data with quality flag values of 0 or 1 were used.

Dynamic ocean topography (DOT) collected by CryoSat-2 from early September to early October was used to calculate surface geostrophic velocity (Scharroo et al., 2013).

Daily sea-ice concentrations from AMSR2 (a passive microwave instrument) were used to map sea ice extent and assess the timing of freeze up (Spreen et al., 2008).

Synthetic Aperture Radar (SAR) satellite imagery provided occasional high resolution (~50m) representation of the ice conditions. Backscatter characteristics can be used to clearly distinguish open water, sea ice floes, sea ice ridges, leads, and ice type with a much higher level of detail than passive microwave sea ice products (e.g., Kwok et al., 1999).

2.6 Surface velocities

To calculate geostrophic velocity, DOT data were linearly interpolated to a regularly spaced latitude/longitude grid with approximately 15-km spacing and smoothed with a 2-D Gaussian kernel using the MATLAB imgaussfilt function with a standard deviation of 0.5. Geostrophic velocities were calculated from the smoothed DOT $=\eta$ as

$$u_g = -\frac{g}{f}\frac{\partial\eta}{\partial y}, v_g = \frac{g}{f}\frac{\partial\eta}{\partial x}$$

The average velocity in the Ekman layer was calculated from ERA5 horizontal turbulent surface stresses τ^x and τ^y as

$$v_{Ek} = -\frac{\tau^x}{f\,\rho_0\,D_{Ek}}, u_{Ek} = \frac{\tau^y}{f\,\rho_0\,D_{Ek}}$$

The reference density $\rho_0 = 1026$ kg/m^3 and the Coriolis parameter $f = 2\Omega\, sin(latitude)$.

2.7 Mixed layer modeling

The atmospheric influence on the ocean mixed layer was examined using the one-dimensional upper ocean mixing model of Price et al. (1986), hereafter called the Price–Weller–Pinkel (PWP) model. In each PWP timestep, heat and freshwater are added to (for ocean heating/precipitation) or subtracted from (for ocean cooling/evaporation) the water column. The water column overturns if these subtractions make the density structure unstable, entraining successively deeper depth bins until the stratification is stable. Momentum imparted by surface stress is then added to the mixed layer and additional depth bins are entrained into the mixed layer until the bulk and gradient Richardson numbers exceed critical values (0.65 and 0.3, respectively). The gradient Richardson number requirement simulates shear flow instabilities.

We forced the PWP model with net longwave, net shortwave, sensible, and latent heat fluxes, surface stresses, and evaporation and precipitation extracted from ERA5 reanalysis at 0.25° resolution at hourly intervals (Hersbach et al., 2018). The mean (not instantaneous) ERA5 data were used. The PWP model was used to explore the ocean's evolution as it cooled to freezing, so we assumed that the ocean was ice-free and did not include freshwater/salt additions due to ice melt/growth. For each observed temperature and salinity profile ERA5 atmospheric forcing was averaged in a 30-km box centered at the profile's location. The net shortwave heat flux was distributed throughout the water column according to the extinction coefficient while the sum of the net longwave, sensible, and latent heat fluxes was added to the shallowest depth bin. The PWP depth bin size was 1 m and the deepest bin was 50 m.

Surface forcing was interpolated to 10-minute temporal resolution to run the PWP model with a 10-minute timestep. Use of a short timestep was necessary because when ocean heat loss integrated over a longer timestep was extracted from the uppermost model cell, the water in that cell could momentarily fall below the freezing point. Distributing cooling over a larger number of short timesteps caused static overturn without the surface cell falling below freezing.

The momentum and scalar diffusivities were set to 10^{-6} m^2/s following Dewey et al. (2017). The mixing layer depth in the PWP experiments was the depth at which density was at least 0.01 kg/m^3 greater than the surface density, consistent with the Beaufort Sea PWP experiments of Toole et al. (2010).

3 Observations

3.1 Overview

The following sections show how horizontal advection of sea ice meltwater hastened freeze up. Melting sea ice that lingered in the southern Beaufort Sea created a cold, fresh, and shallow mixed layer and associated submesoscale meltwater front (section 3.2). In situ Seaglider and ship-based observations documented the northward advection of this feature during the three weeks preceding freeze up (section 3.3, Figure 2). The meltwater advection can be explained by the combination of Ekman and geostrophic velocities (section 3.4).

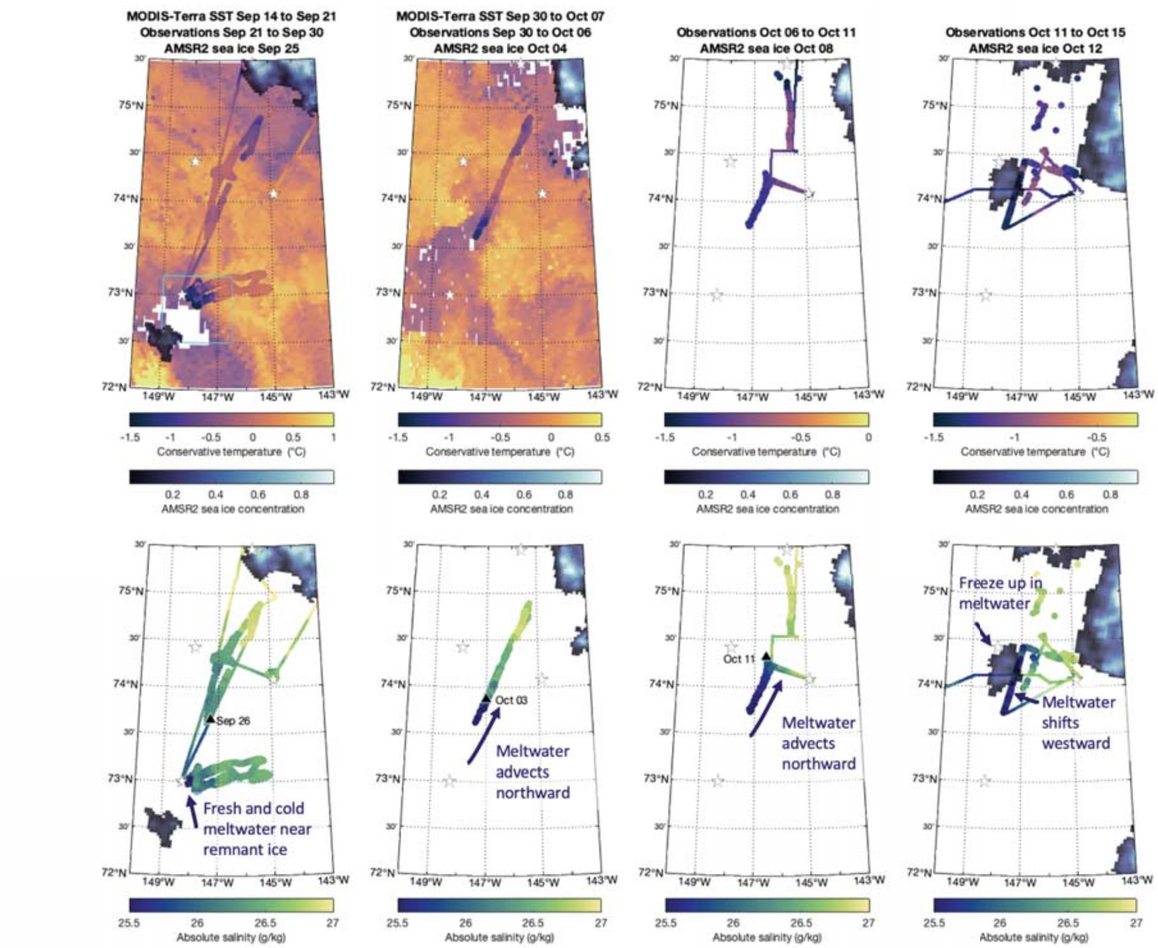

Figure 2 *Upper ocean observations and remote sensing show the meltwater's advection in the weeks preceding freeze up. Temperature (upper row) and salinity (lower row) observations, including Seaglider and uCTD data averaged in the upper 5 m as well as Wave Glider data at 5 m or 9 m (large scatter points) and Healy underway data at 2.7 m (thin line), at the time periods specified in the column titles. MODIS SST is included in the first two panels and the AMSR2 ice concentration is shown where it exceeded zero. The black triangles are the locations of the 26 g/kg isohaline outcrop, a proxy for the edge of the meltwater. The 26 g/kg isohaline did not*

outcrop in the third panel; the marked end of that transect indicates the meltwater extended at least to that location.

3.2 Ice and ocean conditions before meltwater advection

Ice retreated from the central Beaufort Sea in late July and early August 2018 (Figure 1). The study area was roughly delineated by four subsurface moorings installed as part of the SODA program; while data from those moorings are not used in this study, mooring locations are marked by star symbols on maps as "landmarks" to orient the reader. The primary ice edge was northeast of the study area, and an additional area of ice separate from the main ice pack persisted in the southern Beaufort Sea throughout August and into September (Figure 1). The remnant ice then shrank and moved northwestward, leaving the region ice-free after 28 September. The decrease in the remnant ice area (Figure 1) indicates most of it melted locally in the southern Beaufort Sea.

Initially, sea surface temperatures were relatively cold only near the ice edges. MODIS data from 14–21 September showed a band of cold water extending roughly 100 km from the northeastern MIZ as well as a localized cold patch surrounding the melting remnant ice (Figure 2). In situ observations agreed with this MODIS sea surface temperature pattern. Seagliders observed cooler mixed layer temperatures at the northward limit of their transect, aligning with the SST gradient seen in the satellite imagery adjacent to the northern MIZ. Wave Gliders observed a near-surface (9 m) temperature gradient that roughly aligns with that in the satellite imagery near the remnant ice. Some differences between the MODIS and in situ temperatures in Figure 2 could be because the observations were from later than the MODIS period (Wave Gliders 19–23 September, Seagliders 22–26 September; the concurrent MODIS data were too limited by clouds to discern SST gradients). However, a careful comparison of in situ SST and concurrent MODIS SST shows that MODIS temperatures were warmer than the in situ observations (Figure 3a, additional discussion in section 3.4).

Seaglider temperature-salinity profiles collected on 26 September in the cold footprint of the remnant ice show surface conditions consistent with modification by local ice melt (Figure 4e,f). In these profiles the mixed layer was relatively cold and fresh and was about 10 m deep. Salinity increased by about 1 g/kg between the surface and 20 m where a near surface temperature maximum was approximately 1–1.5°C warmer than the near-freezing sea surface.

This cold, fresh, and shallow surface layer will be called the meltwater, with the lateral transition from cold to warm surface temperatures called the meltwater front.

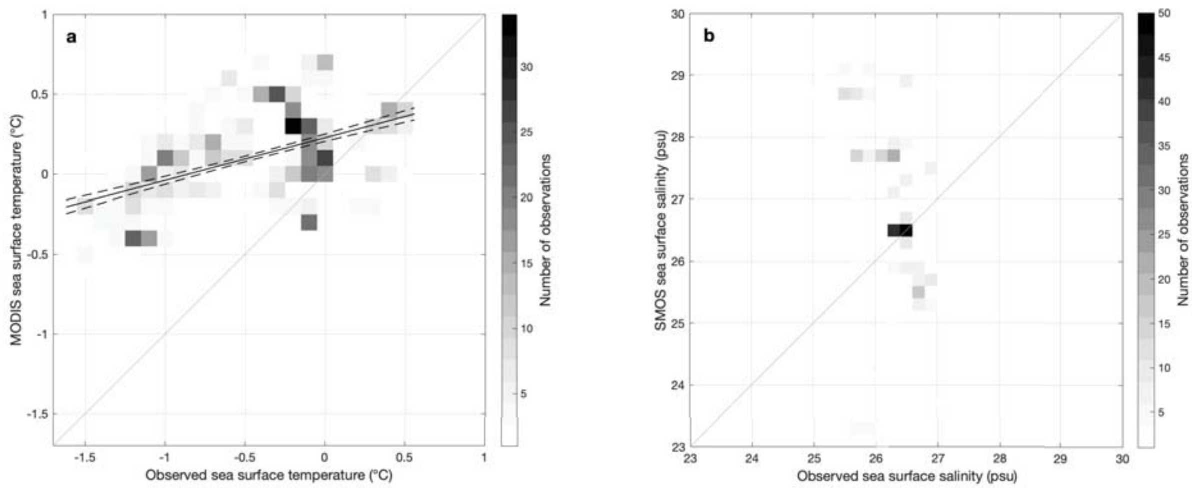

Figure 3 *Scatter plots comparing in situ (a) temperature and (b) salinity from Seagliders, Wave Gliders, uCTD, and the Healy underway system ("observed") to concurrent satellite data. Satellite data was from (a) daily MODIS-Terra and (b) weekly SMOS ARCTIC (Supply et al., 2020a). The solid line in (a) is the linear regression and the dashed lines are the 95% confidence bounds.*

Density measured at 0.25 m and 9 m by a Wave Glider that crossed the meltwater front increased by about 0.5 kg/m^3 over the 10-km transect (Figure 4b). The horizontal buoyancy gradient $M^2 = \frac{\partial b}{\partial x\prime}$ reached 10^{-6} s^{-2} (Figure 4c) where the buoyancy $b = -\frac{g\rho}{\rho_0}$ was calculated using the gravitational acceleration $g = 9.81$m s^2 and the reference density $\rho_0 = 1026$ kg/m^3. M^2 was calculated in the along-track direction x' between pairs of successive Wave Glider density measurements.

Geostrophic velocity associated with the meltwater front was estimated from the buoyancy gradient along the Wave Glider transect using thermal wind balance. The thermal wind velocity shear was vertically integrated from 15 m to calculate velocity relative to the larger scale circulation present below the meltwater. The meltwater front geostrophic jet reached speeds of more than 0.1 m/s at the surface with an associated Rossby number $\left|\frac{\varsigma}{f}\right| \sim 1$, where the vertical component of relative vorticity $\varsigma = \frac{\partial v}{\partial x} - \frac{\partial u}{\partial y}$.

The vertical density difference between the Wave Glider measurement depths exceeded 0.1 kg/m^3 throughout the transect and peaked around 0.25 kg/m^3 near where the lateral buoyancy gradient was greatest (Figure 4c). This density difference indicates that the deeper measurement was roughly aligned with the bottom of the mixed layer, so the mixed layer buoyancy frequency, N^2, was estimated using the difference in density between the measurements as $N^2 = -\frac{g}{\rho_0}\left(\rho_{deep\ CTD} - \rho_{surface\ CTD}\right)/\left(z_{deep\ CTD} - z_{surface\ CTD}\right)$. The Richardson number f^2N^2/M^4 was approximately 5 at the front.

The low Richardson number and high Rossby number point to the submesoscale character of the meltwater front in the Wave Glider transects. Consistent with an active submesoscale field, satellite-derived synthetic aperture radar imagery shows wave-like and filamentous structures at the ice edge that evolved substantially over several days (Figure 4a,d), suggesting mixed layer eddies were present.

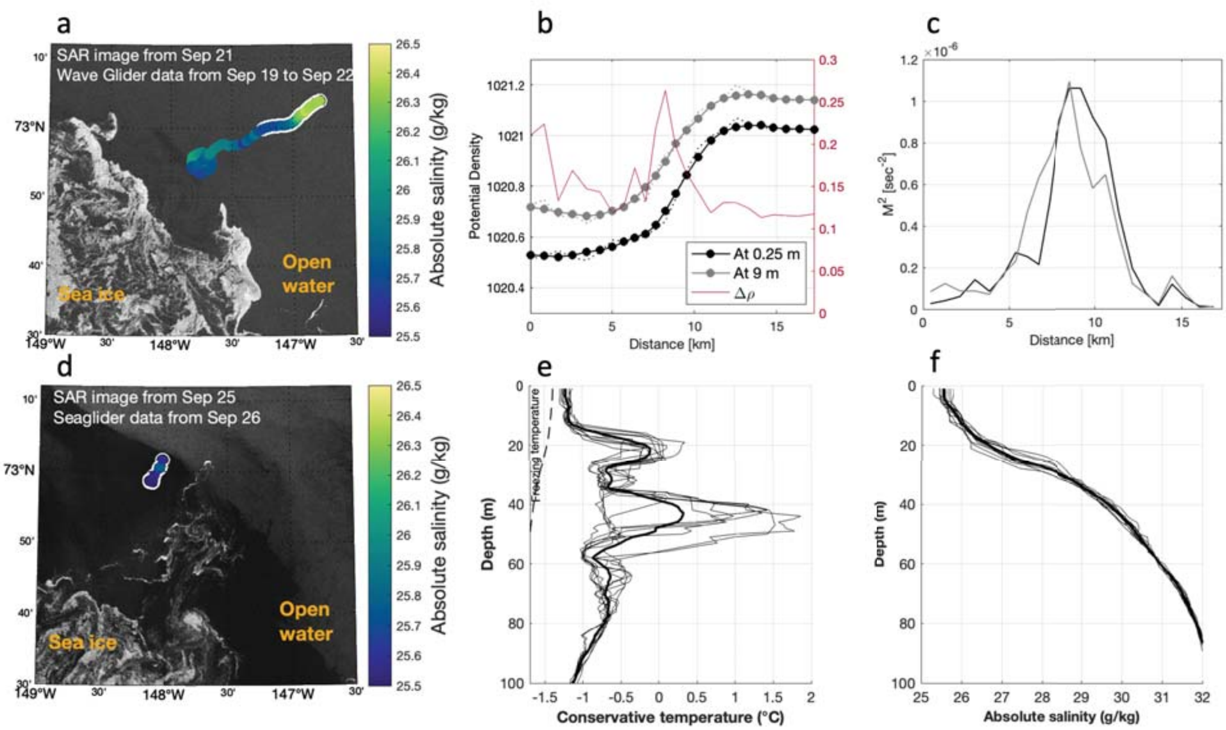

Figure 4 *Meltwater conditions near the remnant sea ice. (a) Wave Glider salinity at 0.25 m and sea ice from SAR on 21 September in the cyan box in Figure 2, with data from the white-outlined track shown in (b) and (c). (b) Wave Glider potential density at 0.25 m (black lines) and 9 m (gray lines) including the raw data (dotted lines) and data smoothed with a moving mean with a*

window width of approximately 4 km (solid lines). The density difference between the shallow and deep measurements is shown in red. (c) Along-track horizontal buoyancy gradient M^2 calculated from the smoothed density. (d) Seaglider salinity averaged in the upper 5 m and sea ice from SAR on 25 September. (e-f) Seaglider profiles, including the average profiles (bold lines) of (e) temperature and (f) salinity.

Away from the ice edges, the late summer mixed layer had relatively uniform properties. In the central part of a 22–26 September Seaglider transect the mixed layer was about 25 m with temperature of approximately 0°C and salinity of approximately 26.5 g/kg (Figure 5 top panels). Below the mixed layer isopycnals sloped downward with increasing latitude (Figure 5 top panels). The northern MIZ's influence was apparent at the northern end of the transect, where the mixed layer was somewhat colder, saltier, and deeper (depth about 30 m, conservative temperature of approximately –0.5 °C, absolute salinity of approximately 26.9 g/kg, not shown).

3.3 Meltwater advects northward over several weeks

In the 30 September to 7 October MODIS SST image a cold filament-like structure extended northward from the meltwater around the remnant ice (Figure 2). Consistent with the SST imagery, Seagliders observed a colder and fresher surface layer spreading northward along their transect from 3–10 October. This layer decreased mixed layer depth to about 15 m (Figure 5 bottom panels). Mixed layer temperature and salinity (conservative temperature around –1°C, absolute salinity around 25.7 g/kg) were similar to those observed earlier in the area of the remnant ice (Figure 6). Similarity in upper ocean temperature and salinity properties along with the apparent coherence of the cold filament in the SST imagery strongly suggest northward advection of the meltwater. The 3–10 October Seaglider data show that the meltwater front had weakened, with M^2 reduced to 20% of that measured earlier by the Wave Glider (roughly 80 km to the south).

Satellite SST imagery was too limited by cloud cover to fully visualize the meltwater after 7 October, but the in situ observations suggest it moved northward and westward in subsequent days. The meltwater occupied the entirety of the next Seaglider transect, sampled from 6–11 October, indicating continued northward meltwater advection (Figure 2). Observations by Seagliders, uCTD, and *Healy*'s underway system from 11–14 October show that warmer and saltier waters replaced those found in the meltwater's former location, but that cold and fresh surface conditions were present further west. These observations suggest westward advection of the meltwater along with a westward shift of meltwater-adjacent waters. An isolated ice patch formed on 12 October coincident with the meltwater location (Figure 2). Heterogeneity in surface temperature and salinity persisted until the onset of freeze up, and freeze up occurred earliest in the meltwater. The mechanisms by which the meltwater hastened freeze up are discussed in Section 4.

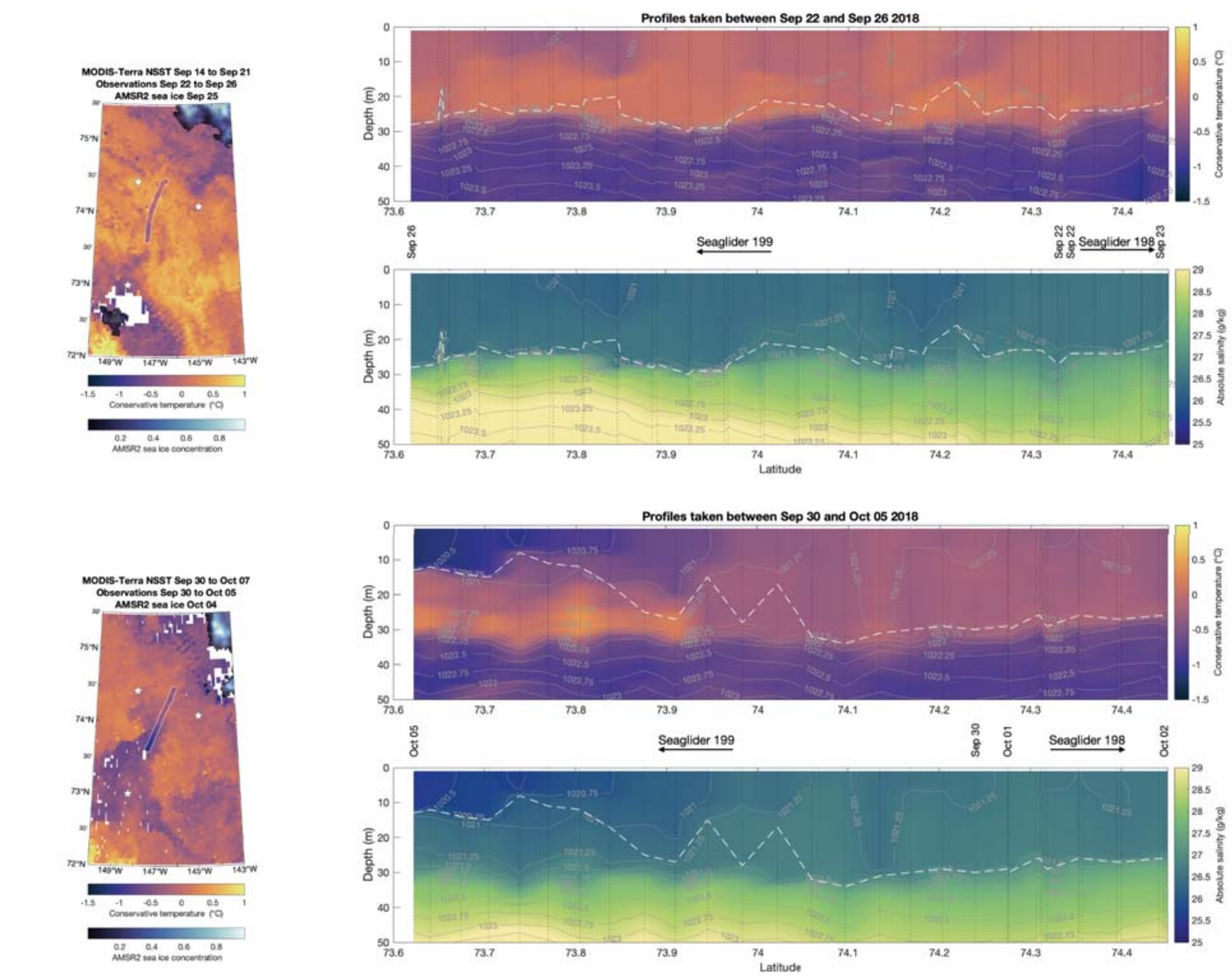

__Figure 5__ Conservative temperature and absolute salinity in latitude-depth sections measured by two Seagliders from 22–26 September (top) and from 30 September to 5 October (bottom). Sampling began partway through the transect with one Seaglider sampling outward in each direction, indicated by the dates and arrows. Gray lines mark potential density contours at 0.25 kg/m^3 intervals and the dashed white line marks mixed layer depth defined as a density

difference of 0.25 kg/m³ relative to the surface. Sections show only the upper 50 m of the 1000-m profiles, with vertical lines indicating individual profiles and profile locations shown in the maps to the left.

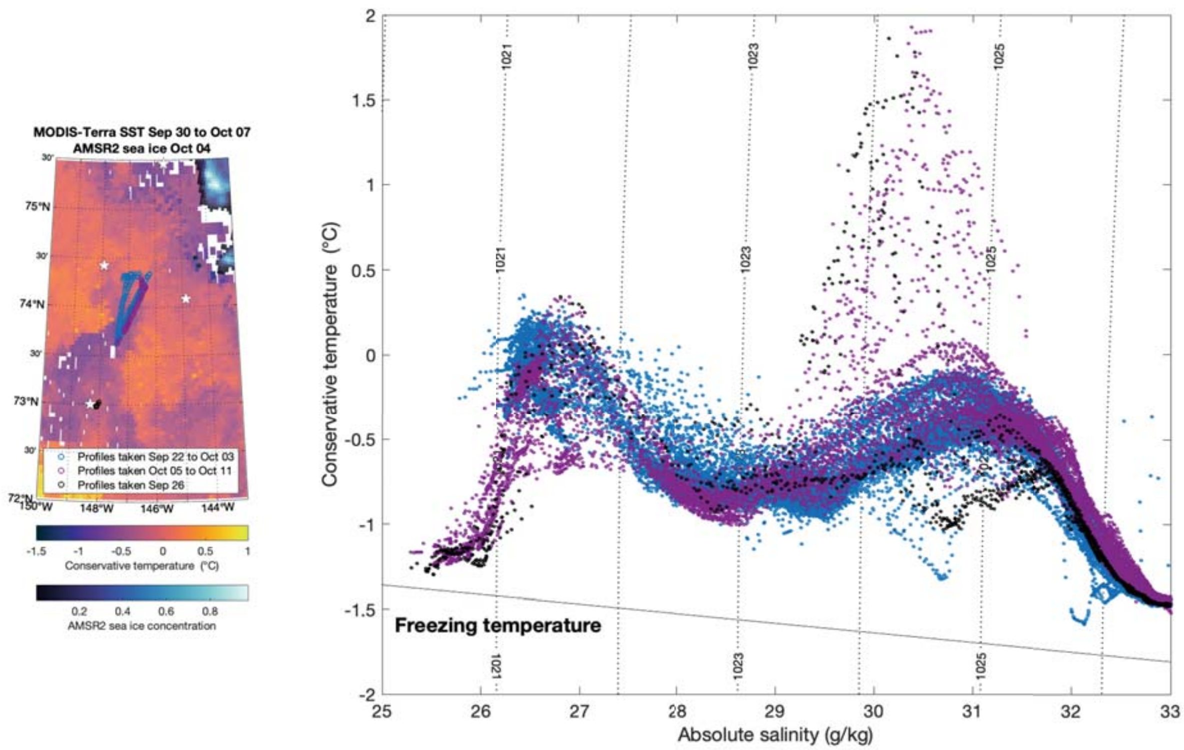

Figure 6 *Temperature and salinity profiles taken in the remnant ice area (black) and farther north before (blue) and after (purple) the meltwater arrived. (left) Profile locations. (right) Profiles along with potential density contours. The freezing temperature at the surface is indicated.*

3.4 A comparison of observed and remotely sensed sea surface temperature and salinity

The in situ observations presented in this paper provide an opportunity for comparison with concurrent remote sensing. In situ temperature observations were compared to MODIS-Terra nighttime sea surface temperature averaged within a 15 km box centered on the observation (Figure 3a). The closest daily MODIS image in time with any data in the spatial averaging box was used, with candidate MODIS images occurring up to three days before or three days after the observation. In situ salinity observations were compared to weekly SMOS

ARCTIC sea surface salinity (Supply et al., 2020). In situ temperature and salinity observations from the Seagliders (averaged in the upper 3 m), Wave Gliders (at 0.2 m), uCTD (averaged in the upper 3 m), and *Healy* underway system (at 2.7 m) were distributed unevenly in time, space, and by platform (i.e., all Wave Glider measurements were from a short period of time in a limited area and the *Healy* underway system's rapid sampling meant there were far more underway samples). To account for this, the *Healy* underway and Wave Glider datasets were subsampled to create a comparison dataset more representative of the entire region and time period. Plots of in situ data from individual platforms vs. satellite data showed the same general patterns as the multi-platform comparison.

The MODIS sea surface temperatures tended to be warmer than observations, with this difference exacerbated at in situ temperatures of less than 0°C (i.e., as the ocean approached freeze up, Figure 3a). The standard deviation of the differences between in situ sea surface salinity and concurrent SMOS sea surface salinity was 1.66 g/kg, with larger differences common at in situ salinities typical of the meltwater (Figure 3b). Note that the SMOS ARCTIC product used here (Supply et al., 2020a, 2020b) corrects for biases caused by cold water (Köhler et al., 2014) and the presence of sea ice (Tang et al., 2018). These comparisons demonstrate the importance of in situ observations, particularly for smaller scale features or conditions typical of cold and stratified meltwater. As a further consideration, this study will demonstrate the importance of mixed layer depth variability to freeze up timing variability (section 4), the characterization of which requires in situ observations. Despite these shortcomings, the MODIS data in particular provided useful regional-scale context in visualizing the extent of the meltwater (Figure 2).

3.5 Simulated advection by geostrophic and Ekman velocities

The observed northward advection of the meltwater can be explained by a combination of geostrophic and Ekman advection. Simulated trajectories were created using geostrophic velocity, Ekman velocity, and the combination of the two. For each trajectory, "tracking" was initialized on 21 September near where the Wave Gliders showed the edge of the meltwater (Figure 7), then the location was updated at hourly time steps (corresponding to the times at which ERA5 surface stress was available) using the appropriate velocity. Ekman velocities were calculated using the ERA5 surface stress that was closest in space at the given timestep and geostrophic velocity was taken as the spatially closest DOT geostrophic velocity. Trajectories were then advanced with each individually and with the sum of the two

Meltwater advection can be tracked in the observations using the 26 g/kg isohaline outcrop as a proxy for the meltwater edge (triangle symbols on Figures 2 and 7). Ongoing upper ocean cooling altered surface density slightly, motivating the use of an isohaline rather than an isopycnal. The simulated trajectories are evaluated by their ability to reproduce the observed advection.

The ocean geostrophic velocity calculated from DOT showed cyclonic circulation with a length scale of approximately 100 km located north of the remnant ice area (Figure 7). This geostrophic circulation agrees with the sloping isopycnals below the mixed layer seen in the southern half of the first Seaglider transect (Figure 5 top panels), which crossed the northern part of the cyclonic circulation seen in the DOT. This observed isopycnal slope also agrees qualitatively with the large-scale *anticyclonic* circulation of the Beaufort Gyre, but the substantial weakening of this subsurface meridional density gradient between Seaglider transects (compare top and bottom panels in Figure 5) suggests that it was attributable in part to transient circulation like the cyclonic circulation derived from the DOT.

Trajectories calculated from the geostrophic velocity alone followed the cyclonic circulation northward but fell short of the observed extent of northward advection (not shown). Although the full DOT survey of the study area took more than a month and consisted of a series of parallel, roughly meridional satellite tracks, the orientation of these tracks meant that the zonal DOT gradients were captured on timescales of only a few days, giving confidence in the calculated northward velocities.

Ekman transport advected the meltwater northward, but Ekman-only advection was also insufficient to match the observed northward advection (not shown). For Ekman depth D_{Ek} = 10 m, simulated Ekman trajectories from 21 September to 3 October went southwestward and then northeastward back to near their original locations. From 3–11 October, Ekman trajectories extended 50 km to the northeast (regionally averaged Ekman velocity shown in Figure 7).

Ekman depth was estimated as $\boldsymbol{D_{Ek} = 10}$ m to match the average mixed layer depth in the remnant ice area Seaglider profiles. Previous observations under sea ice in the Beaufort Sea from October to March indicate a median Ekman depth of 11 m, with most Ekman depths shallower than mixing depths (Cole et al., 2014). While our study is in ice-free waters so these results might not apply directly, they do indicate that it is reasonable to assume that the Ekman depth is comparable to the mixed layer depth. The mixed layer depth increased to 14 m in the 5–11 October Seaglider transect (Figure 8) so the sensitivity of the simulated trajectories to the choice of Ekman depth is discussed shortly.

Neither Ekman-only nor geostrophic-only advection was sufficient to explain the filament's northward advection, but the simulated trajectories driven by the combined velocities did transport surface water far enough to be in coarse agreement with the observations (Figure 7). Additionally, the more western simulated trajectories, initiated in the core of the meltwater, aligned well with the early ice formation patch.

When tracking was initiated in the same start positions as before and advected using the combined velocities calculated from Ekman depths of 15 m or 20 m, some trajectories terminated between 146°W to 148°W and 74°N to 75°N, in qualitative agreement with the observations and with the 10 m Ekman depth results. The main difference from the 10 m Ekman depth results was that some of the western trajectories were more strongly affected by the geostrophic circulation and were advected southward after 3 October.

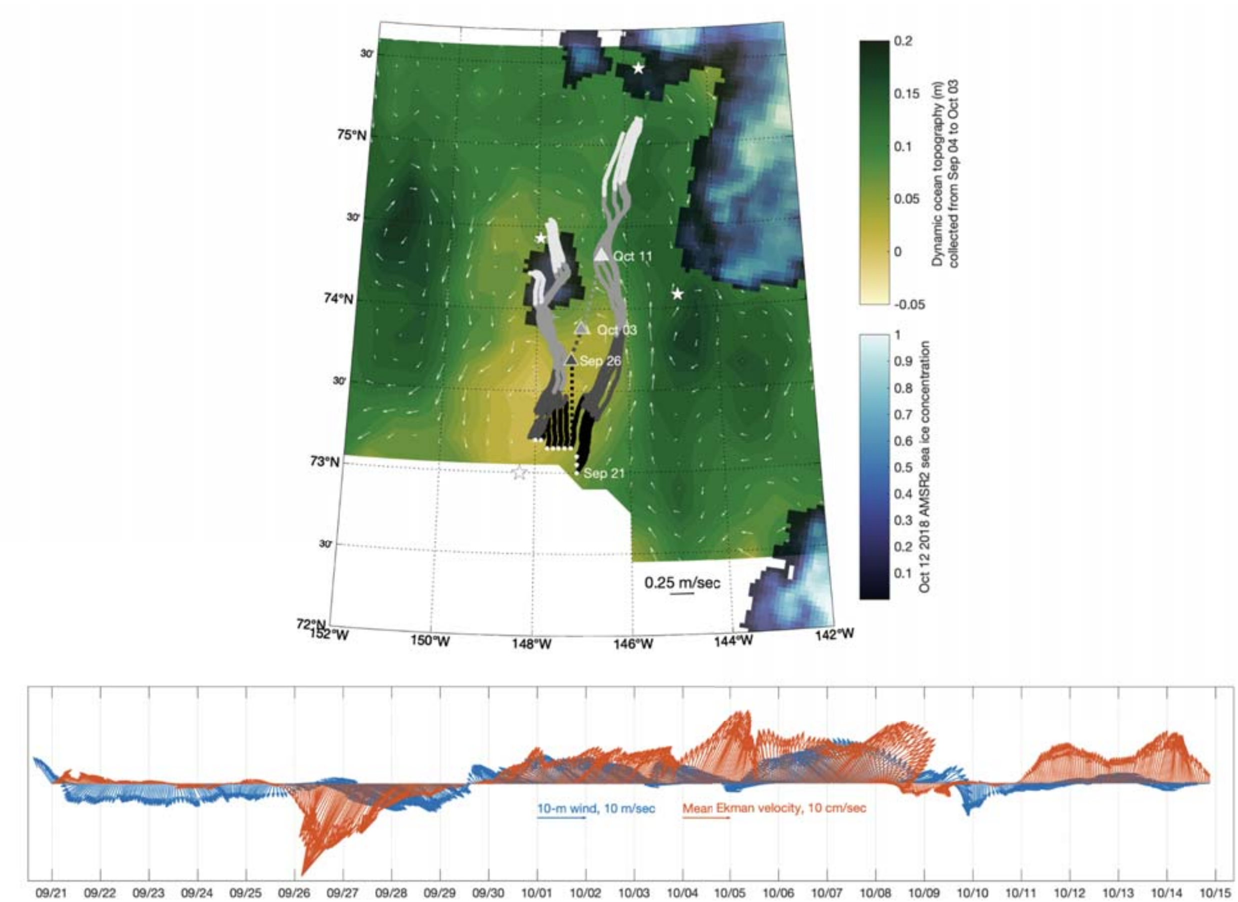

***Figure** 7 Simulated advection trajectories driven by geostrophic and Ekman velocities compared to the observed meltwater advection. (top) Dynamic ocean topography (background colors) and surface geostrophic velocity (white arrows) along with the simulated trajectories advected by the combined geostrophic and Ekman velocities from 21 September (white dots) to 15 October (ends of solid tracks). The locations of the advected tracks at key times (track color changes) correspond to the times of the observed locations of the 26 g/kg isohaline outcrop (colored triangles), which are connected to illustrate the inferred advection path (dotted line). (bottom)*

ERA5 10-m wind and associated Ekman velocities averaged in the region bounded by 145°W to 149°W, 73°N to 74.5°N.

4 Mixed layer heat budget

4.1 Overview

The ocean observations described in the previous section show a correlation between meltwater presence and early freeze up. This correlation suggests meltwater advection was an important mechanism for mixed layer heat loss. These links are quantified in this section, demonstrating that decreases in mixed layer temperature and mixed layer depth due to meltwater advection hastened freeze up by several days. Additionally, a mixed layer heat budget shows that, in the area affected by the meltwater, advection was a leading cause of mixed layer heat loss.

Sea ice starts forming after the mixed layer cools to the freezing temperature. The definition of mixed layer heat content (section 2.2) means the mixed layer heat content goes to zero as the mixed layer temperature approaches the freezing temperature. Changes in mixed layer heat content are due to horizontal and vertical processes. Prior to freezing, vertical (or one-dimensional) processes include net surface heat exchanges with the atmosphere as well as heat exchanges with the underlying pycnocline. Horizontal processes include horizontal advection of colder (or warmer) waters, directly bringing the mixed layer closer to (or further from) its freezing temperature, as well as horizontal advection of waters with different salinity, which impacts the mixed layer depth.

The contributions of each of these processes to the change in mixed layer heat content over our study period were quantified along a transect repeatedly sampled by the Seagliders (Figure 8). The first transect occupation was completed before the meltwater entered the study area; the mixed layer conditions observed on this first transect are the initial conditions against which subsequent observations are compared. The second transect crossed the meltwater front, with meltwater present at the southern end of the transect but absent from the northern end. The meltwater filled the third transect, while the fourth transect did not contain meltwater.

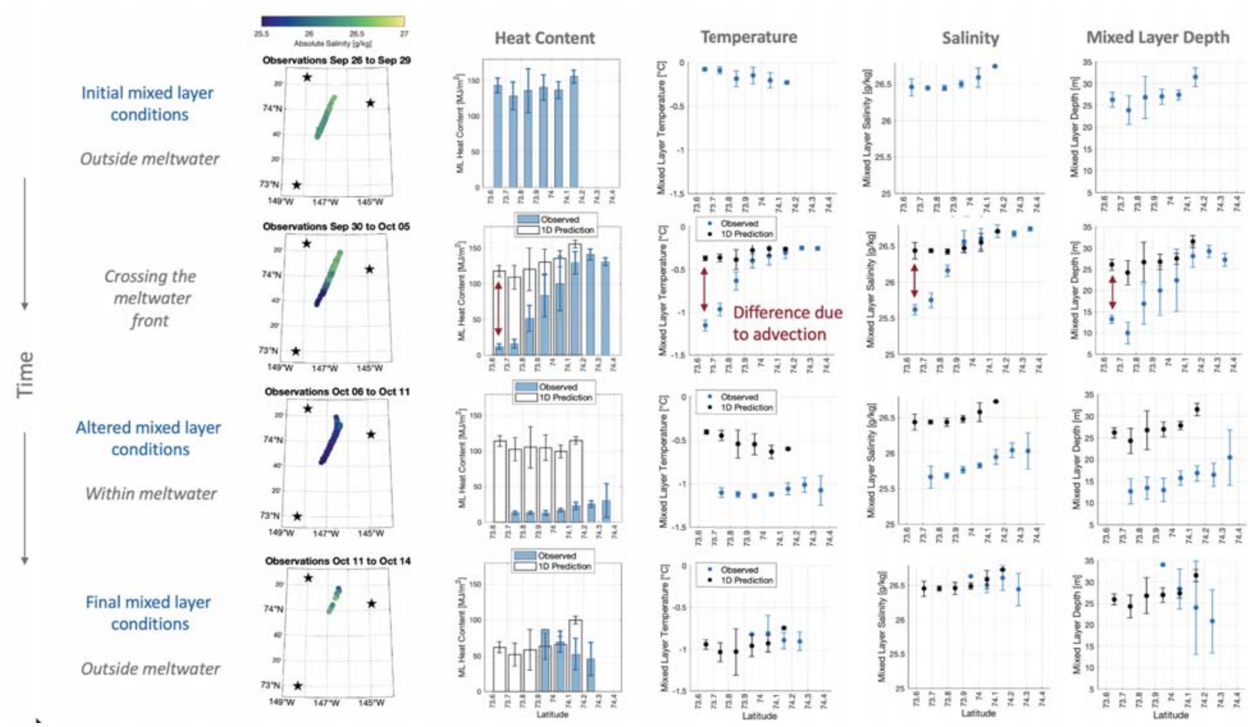

Figure 8 *Differences between observations and model predictions demonstrate that advection altered mixed layer properties. (first column) Locations of salinity observations averaged in the upper 5 m in the time periods specified in the titles, with low salinity indicating meltwater presence. (additional columns) Observed (blue) and concurrent PWP model-predicted (black) mixed layer properties binned by latitude and averaged. There are no model predictions for the first row as these profiles were used to initiate the model. The error bars show one standard deviation.*

4.2 Methods for calculating the heat budget components

The PWP model was used to quantify heat budget components in the presence and absence of meltwater advection. The model was initialized with observed temperature and salinity profiles and forced with ERA5 heat flux, surface stress, and surface freshwater flux until the ocean surface reached the freezing temperature (section 2.5). The net surface heat loss in the heat budget was the ERA5 heat flux time integrated until modeled freeze up.

The model allowed us to estimate one-dimensional heat exchanges between the pycnocline and the mixed layer via mixed layer deepening that entrains the pycnocline, or via turbulent diffusion, combined into a bulk pycnocline heat exchange here. The time integrated mixed layer heat exchange with the pycnocline was quantified as the change in pycnocline heat content between the initial observation and modeled freeze up. The pycnocline heat content was the depth integrated heat content between the base of the mixed layer and 50 m, the deepest depth simulated in the PWP model. The conclusions are not sensitive to the choice of deeper integration bound.

Differences between observations and concurrent modeled conditions initiated with earlier observations can be attributed to horizontal advection. Thus, the advective component of the mixed layer heat budget can be estimated as the difference between observed and concurrent modeled mixed layer heat content (see Figure 8 "Heat content" column).

The heat budget for the first Seaglider transect used the model results from the initial, meltwater-free observations run until modeled freeze up and assumed advection was negligible (later results support this assumption). We also used these first-transect model results to bridge the time gaps between the first-transect observations and observations on later transects. For transects other than the first transect, the vertical heat budget terms were the sum of the first-transect model results run until the later-transect observations and the later-transect model results run until modeled freeze up. When combining these model results profiles on the earlier and later transects were not matched directly in a one-to-one fashion. Instead the first-transect model results were averaged in latitude bins then added to the later-transect model results in the same latitude bins.

4.3 Heat budget results

Outside of the meltwater, the PWP model represented the mixed layer evolution well (Figure 8, bottom row). Mixed layer properties observed on the final 11–14 October transect outside of the meltwater agreed with properties predicted by the PWP model initiated by observations on the initial meltwater-free 26–29 September transect. This agreement between observations and concurrent model predictions demonstrates that advection was not important to the mixed layer heat budget outside of the meltwater. Mixed layer heat content changes outside the meltwater were almost entirely due to heat loss to the atmosphere, which totaled 128 MJ/m^2 between the initial observations and modeled freeze up on average (Figure 9). Heat gained by the mixed layer from the pycnocline averaged 1.4 MJ/m^2 (Figure 9), small compared to heat loss to the atmosphere.

Observations within the meltwater deviated substantially from concurrent PWP model predictions, indicating a strong role for advection in setting mixed layer properties. The observed meltwater mixed layer was about 0.55°C colder and 13 m shallower than concurrent PWP model predictions (Figure 8, middle two rows). The difference between observed and concurrent modeled mixed layer heat content indicated an advective mixed layer heat loss of about 90 MJ/m^2 (Figure 9). Heat loss to the atmosphere was about 50 MJ/m^2 between the initial meltwater-free observations on the first transect and the freeze up time for model runs initiated in the meltwater (Figure 9). Heat gained from the pycnocline between the initial meltwater-free observations on the first transect and the freeze up time for model runs initiated in the meltwater was variable, with maximum values of up to 44 MJ/m^2 (Figure 9). The larger pycnocline heat exchange within the meltwater relative to outside the meltwater was likely due increased shear-driven mixing at the base of the shallower meltwater mixed layer.

Average heat fluxes to the atmosphere throughout the study period were between −45 W/m^2 and −65 W/m^2, with higher values for later-freezing profiles. This pattern makes sense because atmospheric heat loss accelerated as autumn progressed, so later-freezing profiles were exposed to larger, late-season heat fluxes for longer. The largest heat flux from the ocean to the atmosphere during our study period was around −150 W/m and occurred on 7 October.

Our observations do not span the entire autumn cooling period. ERA5 showed that heat exchanges between the ocean and atmosphere became net negative around 10 September and about 50 MJ/m^2 of ocean heat was lost to the atmosphere before Seaglider sampling began (not shown). Lacking ocean observations, we cannot estimate the pycnocline and advective heat budget components during this intervening period. However, accounting for this earlier ocean cooling implies seasonally-integrated heat loss to the atmosphere (50 MJ/m^2 prior to the earliest observations + 50 MJ/m^2 between observations and freeze up in the meltwater) was comparable to the mixed layer heat loss associated with meltwater advection (90 MJ/m^2). This demonstrates that meltwater advection played a leading role in mixed layer heat loss integrated throughout the autumn. It also shows that, despite relatively higher values within the meltwater, heat exchanges with the pycnocline were of secondary importance to the mixed layer heat budget compared to heat loss to the atmosphere and advection.

For profiles on the initial, meltwater-free transect, modeled freeze up occurred on 21 October on average (Figure 9), while modeled freeze up for profiles on the final, meltwater-free transect occurred on 18 October on average (not shown), closer to the satellite-observed 16–18 October freeze up southwest of the meltwater (Figure 1). For profiles inside the meltwater, modeled freeze up occurred on 11 October on average (Figure 9). This agrees with the satellite-observed ice patch that formed on 12 October adjacent to the previously-observed meltwater (Figure 2). The agreement in satellite-observed and modeled freeze up timing in the meltwater implies that while the meltwater's presence was due to advection, the evolution within meltwater was one-dimensional.

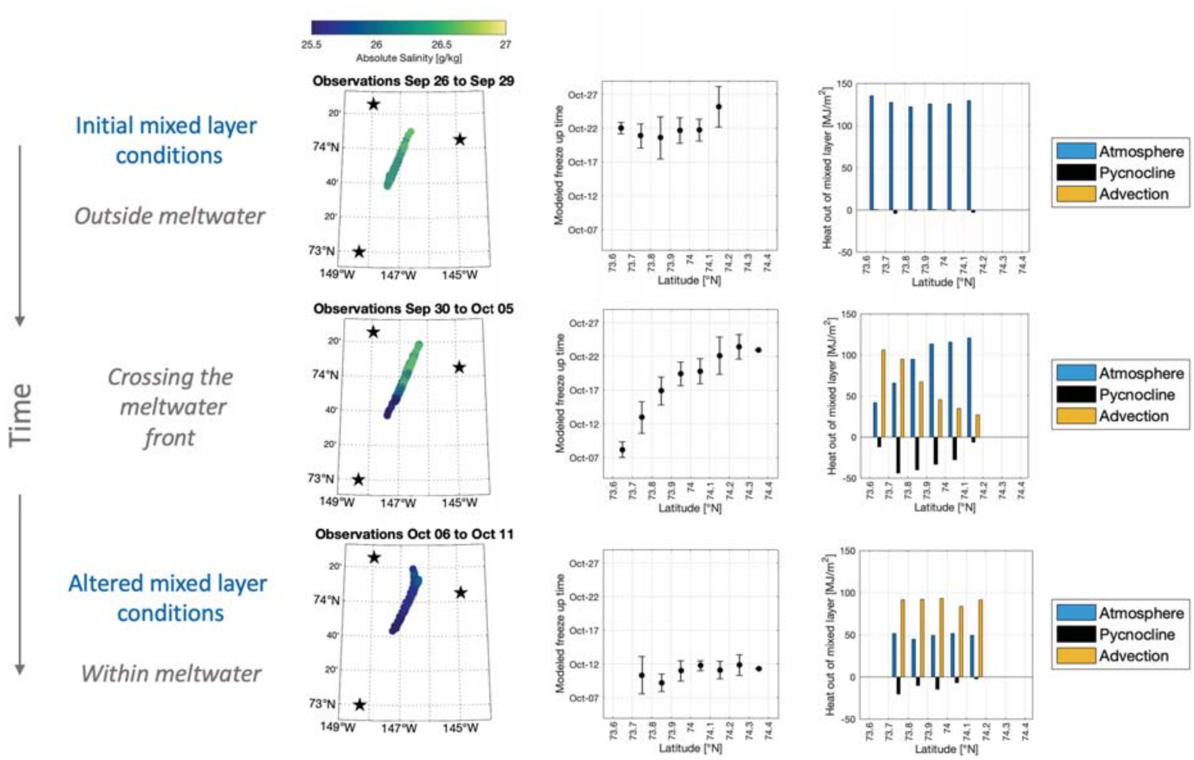

Figure 9 *Freeze up times and mixed layer heat budgets varied with the presence or absence of meltwater. (first column) Locations of salinity observations averaged in the upper 5 m in the time periods specified in the titles, with low salinity indicating meltwater presence. (second column)*

PWP model-predicted freeze up binned and averaged by latitude. The error bars are one standard deviation. (third column) Heat budget components for each latitude bin.

5 Additional advection: Restratification hastens freeze up in northern study area

This section shifts focus to the northern part of the study area and briefly discusses a freshwater advection event separate from the meltwater advection described previously. Freeze up swept across the northern study area on 14 October, which was several days earlier than predicted by PWP model runs initiated by observations in the area on or before 7 October. Though not recreated in PWP model runs, shoaling mixing depth, which would confine heat loss to a smaller portion of the water column, offers a possible explanation. Consistent with this mechanism, Seaglider observations from 12–15 October show that the upper 15 m of the water column freshened, decreasing the average surface density by 0.1 kg/m^3 compared to the earlier profiles (see the example profiles in Figure 10). PWP runs initiated with these later profiles had shallower cooling and an average PWP freeze up time of 15 October, agreeing with the satellite-derived freeze up timing.

The observed restratification was likely due to lateral processes. Between 7 to 15 October, ERA5 indicated that the time-integrated freshwater flux was out of the ocean, so precipitation cannot explain the decrease in surface salinity. The area was ice-free when restratification was observed (Figure 10), so local ice melt also cannot explain the surface freshening. Lateral processes could act to spread buoyant meltwater and thus create shallow stratification. The model results suggest that this restratification accelerated freeze up.

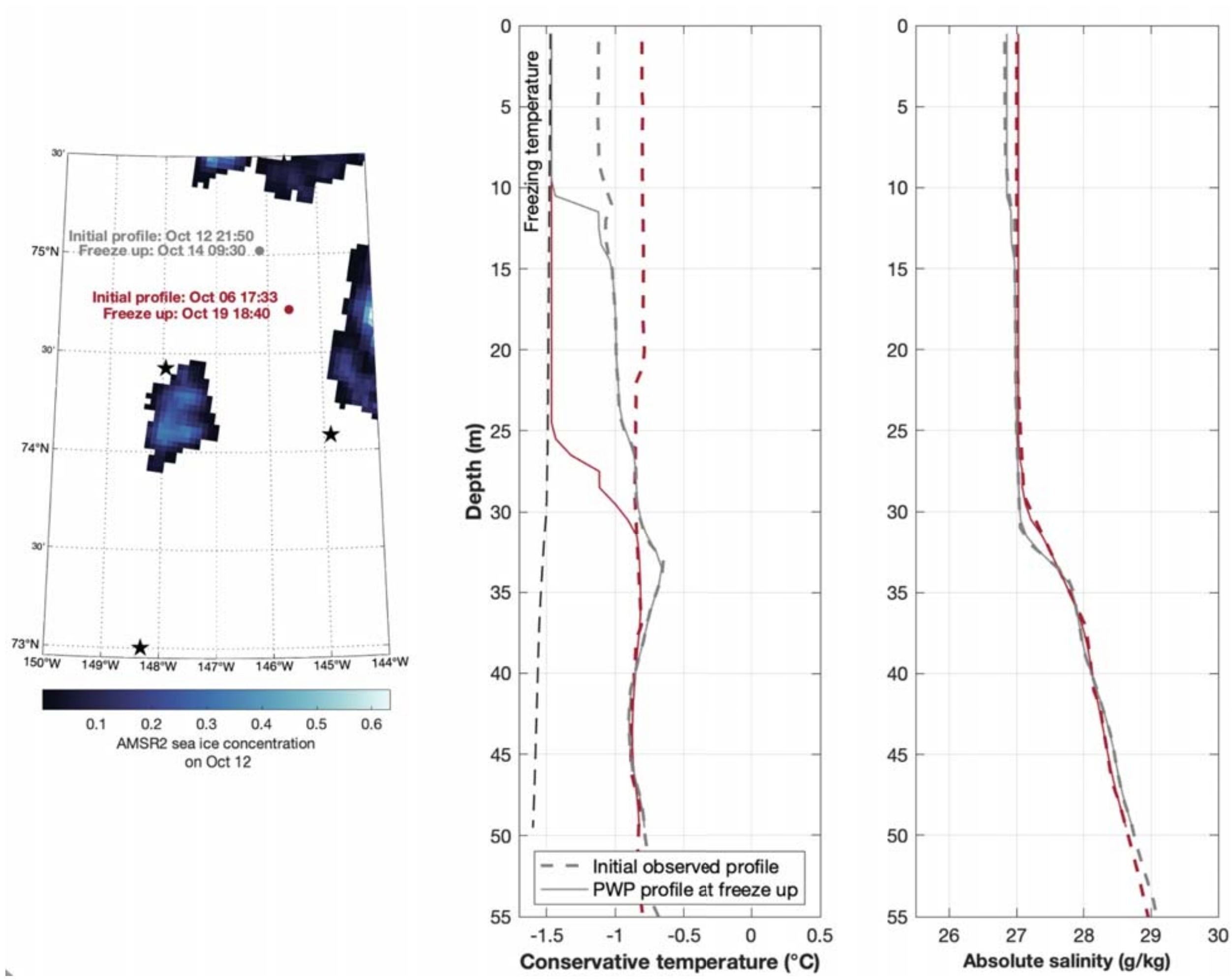

Figure 10 *Surface freshening near the northern MIZ restricted cooling to a shallower layer and resulted in earlier modeled freeze up. (left) Locations of example observed profiles used to initiate the PWP model along with AMSR2 ice concentration where it exceeded zero. (right) Observed temperature and salinity profiles (dashed lines) and modeled profiles at freeze up (solid lines).*

6 Summary and Discussion

This study demonstrates how freshwater advection alters upper ocean stratification and leads to spatial variability in freeze up timing. Nearly 800 ocean temperature and salinity profiles characterize the open water region in the central Beaufort Sea, immediately prior to freeze up in 2018, at high spatial and temporal resolution. Few previous studies capture ice-free Arctic Ocean conditions at these small scales during this critical time of year due to the risks to instrumentation when freeze up is imminent or in progress. The observed oceanic modulation of freeze up means forecasting efforts should consider the three-dimensional evolution of the mixed layer and its impacts on sea ice development.

In one case of freshwater advection, a cold and fresh surface meltwater layer caused by melting remnant ice in the southern Beaufort Sea advected roughly 100 km in several weeks. Meltwater hastened freeze up by cooling and shoaling the mixed layer, with the result that meltwater-affected areas froze several days in advance of surrounding regions where meltwater was not present. Mixed layer shoaling limited the volume of surface water that had to cool to the freezing temperature before ice could form. Outside of the meltwater the weaker stratification distributed cooling over a deeper mixed layer and delayed ice formation.

The mixed layer heat budget for the autumn cooling period showed that, outside of the meltwater, regional-scale heat loss to the atmosphere was the dominant means of mixed layer cooling. Within the area affected by meltwater, advection was nearly as important as heat loss to the atmosphere for seasonally-integrated mixed layer heat loss. Heat gained by the mixed layer from the pycnocline was of secondary importance.

While previous research concluded that advection plays a minor role in Beaufort Sea upper ocean freshening on seasonal timescales (Dewey et al., 2017), we note that the meltwater front documented in our study would be indiscernible in the SIZRS dataset used in Dewey et al. (2017) which has temporal resolution of one month and spatial resolution of 1° of latitude. While determining the frequency of such advective events is outside the scope of this work, we note that a second filament of cold surface water emanating from the remnant ice area, unsampled in our study, was visible in the satellite sea surface temperature imagery (Figure 2). To the extent that anomalously cold surface temperatures were a tracer for meltwater, this sea surface temperature pattern suggests that meltwater advection on O(100 km) scales may be an important source of upper ocean heterogeneity.

A separate freshwater advection event occurred near the MIZ when the mixing layer freshened by 0.1 g/kg in the days preceding freeze up. Our observations do not capture the origin of this freshwater or the exact timing of the restratification; however, ERA5 reanalysis shows that it was not due to precipitation, and satellite imagery shows that it was not due to local ice melt. We thus attribute the restratification to a lateral flow of freshwater. Timmermans et al.

(2012) found that lateral restratification was common in profiles beneath sea ice and noted that the slight density increase below actively mixing layers isolated the rest of the underlying mixed layer and prevented pycnocline entrainment (Timmermans et al., 2012). We add to their results by showing that diverging mixing and mixed layers precondition freeze up, demonstrating a mechanism by which three-dimensional ocean circulation allows freeze up to advance more quickly than one-dimensional ocean cooling would predict.

Submesoscale instability associated with the nearby ice edge is one possible explanation for the restratification observed near the northern MIZ, as modeling studies of submesoscale meltwater fronts show that mixed layer eddies can spread meltwater laterally (Manucharyan and Timmermans, 2013; Horvat el al., 2016; Manucharyan and Thompson, 2017). These modeling studies have emphasized the capacity of submesoscale flows to melt sea ice by laterally transporting heat beneath ice at the surface (Horvat el al., 2016; Manucharyan and Thompson, 2017) or within the pycnocline (Lu et al., 2015), and by trapping sea ice in cyclonic features and advecting it over warm, ice-free water (Manucharyan and Thompson, 2017). Here we shift focus from the importance of submesoscale flows during sea ice melt to the autumn sea ice formation period. Our measurements do not resolve the ocean structure associated with the northern MIZ well enough to determine the dynamics contributing to the observed restratification, but we believe that restratification caused by ice-edge instabilities may affect freeze up and is therefore an important topic for future research.

Using data collected as part of the Stratified Ocean Dynamics of the Arctic program of which this study is also part, MacKinnon et al. (2021) documented the subduction of a jet of very warm (up to 6°C) Pacific Summer Water (PSW). This PSW jet was impinging from the south on remnant sea ice (the same remnant sea ice discussed in this study) and breaking into intrathermocline eddies when observed from 14–17 September 2018. While our study focuses on the mixed layer, our observations document northward advection of warm (nearly 2°C), O(20 km) subsurface boluses of PSW which may represent the continued subduction and advection of the PSW observed by MacKinnon et al. (2021). The PSW warm features that we observed were present in profiles collected in the remnant ice area and then appeared on the Seaglider transect roughly in tandem with the meltwater (Figure 6). The top of the PSW was found at similar salinities in both locations but isopycnals deepened with latitude resulting in a roughly 20 m downward displacement of the PSW as it advected northward (not shown). The later northern profiles showed exceptionally warm PSW at deeper salinities as well (down to S_A=31 g/kg, Figure 6) suggesting downward mixing had occurred.

The stratification below the meltwater stored a relatively large amount of heat in a near surface temperature maximum (NSTM) when ice formed. The modeled depth-integrated heat content from 0 to 40 m (a typical winter mixed layer depth) at freeze up for profiles in the meltwater was 100 MJ/m^2 on average while the modeled heat content at freeze up for profiles outside the meltwater was 67 MJ/m^2 on average. The fate of heat entrained from the NSTM by convection or wind-driven mixing depends on the maturity of the overlying ice. Most heat reaching the base of thick, insulating ice is expected to slow the growth of that ice (Timmermans, 2015), whereas Smith et al. (2018) show that a substantial fraction on of the heat released by a storm early in the freeze up process escaped directly to the atmosphere with only 30-40% going toward melting the thin pancake ice. In addition, downwelling due to Ekman pumping can cause the NSTM to deepen throughout the autumn and winter (Jackson et al., 2010). If surface mixing is relatively weak, this downwelling may be strong enough to sequester the NSTM below the mixed layer such that it persists through the winter (Steele et al., 2011).

While it is not possible with our dataset to differentiate among these outcomes for the additional heat stored in the meltwater-present NSTM relative to the meltwater-absent NSTM, the larger NSTM heat content at freeze up below the meltwater is nonetheless an important result. At first glance, earlier ice formation in the meltwater might be expected to result in thicker ice at the end of winter due to a longer ice growth season. However, entrainment of the stronger (warmer and shallower) NSTM below the meltwater could counteract the “head-start” of earlier ice formation and inhibit seasonally-integrated ice growth. Ice that thins during winter due to NSTM entrainment retreats earlier the following year, allowing the ocean to absorb more solar radiation the following summer (Jackson et al., 2012). The onset of the spring ice algal bloom is light limited (Leu et al., 2015), so earlier ice retreat also impacts the ice-based ecosystem.

Arctic sea ice forecasting is an area of substantial ongoing research (e.g., Guemas et al., 2016 and references therein), and the importance to stakeholders of predicting freeze up on regional spatial scales has recently been highlighted (Bushuk et al., 2017; Day et al., 2014; Stroeve et al., 2016). Positive sea ice area anomalies during the melt season result in cold sea surface temperature anomalies which can persist throughout the summer, meaning the ocean retains a "memory" of previous ice conditions which preconditions the re-emergence of positive ice area anomalies during freeze up (Blanchard-Wrigglesworth et al., 2011; Day et al., 2014). This re-emergence mechanism means that the timing of ice retreat can be used to statistically predict the timing of ice advance in some parts of the Arctic, with moderate predictive skill in the Beaufort Sea (Stroeve et al., 2016). Modeling studies also show that the inclusion of sea surface temperature information contributes to skillful freeze up forecasting at socioeconomically relevant spatial scales (Sigmond et al., 2016; Bushuk et al., 2019). Our results advance this forecasting paradigm by demonstrating that 1) sea surface temperature anomalies associated with late ice retreat advect and precondition freeze up in neighboring areas that did not themselves experience anomalously late ice melt and 2) late ice melt can create persistent, anomalously shallow mixed layer depths that also promote early freeze up.

Data Availability

The ocean observations presented in this paper are available on the University of Washington ResearchWorks archive at http://hdl.handle.net/1773/47135

ERA5 hourly data on single levels were downloaded from the C3S climate data store (https://cds.climate.copernicus.eu/#!/home). The link to the reanalysis on surface/single levels is https://cds.climate.copernicus.eu/cdsapp#!/dataset/reanalysis-era5-single-levels?tab=overview

Sea ice concentration from AMSR2 was downloaded from the University of Bremen data archive at https://seaice.uni-bremen.de/data/amsr2/asi_daygrid_swath/n3125/2018/

Level 3 Daily and 8-Day average MODIS-Terra sea surface temperature data were downloaded from the Physical Oceanography Distributed Active Archive Center at NASA/JPL from https://podaac-tools.jpl.nasa.gov/drive/files/allData/modis/L3/terra/11um/v2019.0/4km

Dynamic ocean topography (DOT) from CryoSat-2 was downloaded from http://rads.tudelft.nl/rads/data/authentication.cgi

Level 3 v1.1 weekly SMOS Arctic sea surface salinity data were downloaded from SEANOE at https://www.seanoe.org/data/00607/71909/

Satellite ice images and analysis were provided via special support from the U.S National Ice Center. RADARSAT-2 Data and Products are under a copyright of MDA Geospatial Services Inc. 2018 – All Rights Reserved, obtained via the U.S. National Ice Center. RADARSAT is an official mark of the Canadian Space Agency. Sentinel-1 data was obtained from the Copernicus Data Hub, supported by the European Space Agency.

Acknowledgments

The authors thank the crews of the USGCG *Healy* and the RV *Sikuliaq* for their expert support in deploying the Seagliders, Wave Gliders, and uCTD. Discussions with members of the SODA team helped develop the ideas presented here.

This work contributes to the Stratified Ocean Dynamics of the Arctic (SODA) research program, funded by the Office of Naval Research under grant numbers N000141612377 (LC, CML, LR) and N000141612349 (JT). This material is based upon work supported by the National Science Foundation Graduate Research Fellowship Program under Grant No. DGE-1762114 (LC). Any opinions, findings, and conclusions or recommendations expressed in this material are those of the author(s) and do not necessarily reflect the views of the National Science Foundation.

The authors declare no conflicts of interest.

References

Alkire, M.B., Jacobson, A., Macdonald, R.W., & Lehn, G. (2019). Assessing the contributions of atmospheric/meteoric water and sea ice meltwater and their influences on geochemical properties in estuaries of the Canadian Arctic Archipelago. *Estuaries and Coasts*, 42, 1226–1248. doi:10.1007/s12237-019-00562-w

Biddle, L. C., & Swart, S. (2020). The observed seasonal cycle of submesoscale processes in the Antarctic marginal ice zone. *Journal of Geophysical Research: Oceans,* 125, e2019JC015587. doi:10.1029/2019JC015587

Blanchard-Wrigglesworth, E., Armour K. C., Bitz C. M., & DeWeaver, E. (2011). Persistence and inherent predictability of Arctic sea ice in a GCM ensemble and observations. *Journal of Climate,* 24(1), 231–250. doi:10.1175/2010JCLI3775.1

Boccaletti, G., Ferrari, R., & Fox-Kemper, B. (2007). Mixed layer instabilities and restratification. *Journal of Physical Oceanography*, 37-9, 2228–2250. doi:10.1175/JPO3101.1

Brenner, S., Rainville, L., Thomson, J., Cole, S., & Lee, C. (2021). Comparing observations and parameterizations of ice-ocean drag through an annual cycle across the Beaufort Sea. *Journal of Geophysical Research: Oceans*, 126, e2020JC016977. doi:10.1029/2020JC016977

Brenner, S., Rainville, L., Thomson, J., & Lee, C. (2020). The evolution of a shallow front in the Arctic marginal ice zone. *Elementa: Science of the Anthropocene*, 8–17. doi:10.1525/elementa.413

Bushuk, M., Msadek, R., Winton, M., Vecchi, G., Yang, X., Rosati, A., & Gudgel, R. (2018). Regional Arctic sea-ice prediction: Potential versus operational seasonal forecast skill. *Climate Dynamics*, 1– 23. https://doi.org/10.1007/s00382-018-4288-y

Bushuk, M., Yang, X., Winton, M., Msadek, R., Harrison, M., Rosati, A., & Gudgel, R. (2019). The value of sustained ocean observations for sea ice predictions in the Barents sea. *Journal of Climate*, 32(20), 7017–7035. doi:10.1175/JCLI-D-19-0179.1

Cole, S. T., Timmermans, M.-L., Toole, J. M., Krishfield, R. A., & Thwaites, F. T. (2014). Ekman veering, internal waves, and turbulence observed under arctic sea ice. *Journal of Physical Oceanography*, 44-5, 1306–1328. doi:10.1175/JPO-D-12-0191.1.t

Day, J. J., Tietsche, S., & Hawkins, E. (2014). Pan-Arctic and regional sea ice prediction: Initialisation month dependence. *Journal of Climate*, 27, 4371– 4390. doi:10.1175/JCLI-D-13-00614.1

Dewey, S. R., Morison, J. H., & Zhang, J. (2017). An edge-referenced surface fresh layer in the Beaufort Sea seasonal ice zone. *Journal of Physical Oceanography*, 47-5, 1125–1144, doi:10.1175/JPO-D-16-0158.1

Guemas, V., Blanchard-Wrigglesworth, E., Chevallier, M., Day, J.J., Déqué, M., Doblas-Reyes, et al. (2016). A review on Arctic sea-ice predictability and prediction on seasonal to decadal time-scales. *Quarterly Journal of the Royal Meteorological Society*, 142: 546-561. doi:10.1002/qj.2401

Hersbach, H., Bell, B., Berrisford, P., Biavati, G., Horányi, A., Muñoz Sabater, J., Nicolas, J., Peubey, C., Radu, R., Rozum, I., Schepers, D., Simmons, A., Soci, C., Dee, D., & Thépaut, J-N. (2018). ERA5 hourly data on single levels from 1979 to present. Copernicus Climate Change Service (C3S) Climate Data Store (CDS). (Accessed on 13 Jan 2021), doi:10.24381/cds.adbb2d47

Horvat, C., Tziperman, E., & Campin, J.-M. (2016). Interaction of sea ice floe size, ocean eddies, and sea ice melting. *Geophysical Research Letters*, 43, 8083–8090. doi:10.1002/2016GL069742

Islam, F., DeGrandpre, M. D., Beatty, C. M., Timmermans, M.-L., Krishfield, R. A., Toole, J. M., & Laney, S. R. (2017). Sea surface pCO_2 and O_2 dynamics in the partially ice-covered Arctic Ocean. *Journal of Geophysical Research: Oceans*, 122, 1425–1438. doi:10.1002/2016JC012162

Jackson, J. M., Carmack, E. C., McLaughlin, F. A., Allen, S. E., & Ingram, R. G. (2010). Identification, characterization, and change of the near-surface temperature maximum in the Canada Basin, 1993–2008. *Journal of Geophysical Research*, 115, C05021. doi:10.1029/2009JC005265

Jackson, J. M., Williams, W. J., & Carmack, E. C. (2012). Winter sea-ice melt in the Canada Basin, Arctic Ocean. *Geophysical Research Letters*, 39, L03603. doi:10.1029/2011GL050219

Köhler, J., Sena Martins, M., Serra, N., & Stammer, D. (2015). Quality assessment of spaceborne sea surface salinity observations over the northern North Atlantic, *Journal of Geophysical Research: Oceans*, 120, 94– 112. doi:10.1002/2014JC010067

Lee, C. M., Sylvia, C., Martin, D., James, M., Ruth, M., & Tom, P. (2016). Stratified Ocean Dynamics in the Arctic: Science and Experiment Plan. Technical Report APL-UW TR 1601. Seattle, WC: Applied Physical Laboratory, University of Washington, 46.

Leu, E., Mundy, C. J., Assmy, P., Campbell, K., Gabrielsen, T. M., Gosselin, M., Juul-Pedersen, T., & Gradinger, R. (2015). Arctic spring awakening—Steering principles behind the phenology of vernal ice algal blooms. *Progress in Oceanography*, 139, 151– 170. doi:10.1016/j.pocean.2015.07.012

Lu, K., Weingartner, T., Danielson, S., Winsor, P., Dobbins, E., Martini, K., & Statscewich, H. (2015). Lateral mixing across ice meltwater fronts of the Chukchi Sea shelf. *Geophysical Research Letters*, 42, 6754–6761. doi:10.1002/2015GL064967

Macdonald, R. W., Paton, D. W., Carmack, E. C., & Omstedt, A. (1995). The freshwater budget and under-ice spreading of Mackenzie River water in the Canadian Beaufort Sea based on salinity and 18O/16O measurements in water and ice. *Journal of Geophysical Research*, 100(C1), 895–919, doi:10.1029/94JC02700

MacKinnon, J.A., Simmons, H.L., Hargrove, J., Thomson, J., Peacock, T., Alford, et al. (2021). A warm jet in a cold ocean. *Nature Communications* 12, 2418. doi:10.1038/s41467-021-22505-5

Manucharyan, G. E, & Thompson, A. F. (2017). Submesoscale sea ice-ocean interactions in marginal ice zones. *Journal of Geophysical Research: Oceans*, 122, 9455–9475. doi:10.1002/2017JC012895

Manucharyan, G. E., & Timmermans, M. L. (2013). Generation and separation of mesoscale eddies from surface ocean fronts. *Journal of Physical Oceanography*, 43–12, 2545–2562. doi:10.1175/JPO-D-13-094.1

Maykut, G. A. (1978). Energy exchange over young sea ice in the central Arctic. *Journal of Geophysical Research*, 83(C7), 3646– 3658, doi:10.1029/JC083iC07p03646

Mensa, J. A., Timmermans, M.-L., Kozlov, I. E., Williams, W. J., & Özgökmen, T. M. (2018). Surface drifter observations from the Arctic Ocean's Beaufort Sea: Evidence for submesoscale dynamics. *Journal of Geophysical Research: Oceans*, 123, 2635–2645. doi:10.1002/2017JC013728

Rainville, L., Wilkinson, J., Durley, M. E., Harper, S., DiLeo, J., Doble, M., et al. (2020). Improving Situational Awareness in the Arctic Ocean. *Frontiers of Marine Sciences*. doi:10.3389/fmars.2020.581139

Scharroo, R., Leuliette, E. W., Lillibridge, J. L., Byrne, D., Naeije, M. C., & G. T. Mitchum (2013). RADS: Consistent multi-mission products, in *Proceedings of the Symposium on 20 Years of Progress in Radar Altimetry*, Venice, 20-28 September 2012, European Space Agency Special Publication, ESA SP-710, p. 4 pp.

Sigmond, M., Reader, M. C., Flato, G. M.,. Merryfield, W. J, & Tivy, A. (2016). Skillful seasonal forecasts of Arctic sea ice retreat and advance dates in a dynamical forecast system. *Geophysical Research Letters*, 43, 12,457–12,465. doi:10.1002/2016GL071396

Smith, M., Stammerjohn, S., Persson, O., Rainville, L., Liu, G., Perrie, W., et al (2018). Episodic reversal of autumn ice advance caused by release of ocean heat in the Beaufort Sea. *Journal of Geophysical Research: Oceans*, 123, 3164– 3185. https://doi.org/10.1002/2018JC013764

Spreen, G., Kaleschke, L., & Heygster, G. (2008). Sea ice remote sensing using AMSR-E 89 GHz channels. *Journal of Geophysical Research*, vol. 113, C02S03. doi:10.1029/2005JC003384

Stroeve, J. C., Crawford, A. D., & Stammerjohn, S. (2016). Using timing of ice retreat to predict timing of fall freeze-up in the Arctic. *Geophysical Research Letters*, 43, 6332–6340. doi:10.1002/2016GL069314

Stroeve, J. C., Markus, T., Boisvert, L., Miller, J., & Barrett, A. (2014). Changes in Arctic melt season and implications for sea ice loss. *Geophysical Research Letters*, 41,1216–1225. doi:10.1002/2013GL058951

Supply, A., Boutin, J., Vergely, J.-L., Kolodziejczyk, N., Reverdin, G., Reul, N., & Tarasenko, A. (2020a). SMOS ARCTIC SSS L3 maps produced by CATDS CEC LOCEAN. SEANOE. doi:10.17882/71909

Supply, A., Boutin, J., Vergely, J.-L., Kolodziejczyk, N., Reverdin, G., Reul, N., & Tarasenko, A. (2020b). New insights into SMOS sea surface salinity retrievals in the Arctic Ocean. *Remote Sensing of Environment*, 249, 112027 (24p.). doi:10.1016/j.rse.2020.112027

Swart, S., du Plessis, M. D., Thompson, A. F., Biddle, L. C., Giddy, I., Linders, T., et al. (2020). Submesoscale fronts in the Antarctic marginal ice zone and their response to wind forcing. *Geophysical Research Letters*, 47, e2019GL086649. doi:10.1029/2019GL086649

Tang, W., Yueh, S., Yang, D., Fore, A., Hayashi, A., Lee, T., et al. (2018). The Potential and Challenges of Using Soil Moisture Active Passive (SMAP) Sea Surface Salinity to Monitor Arctic Ocean Freshwater Changes. *Remote Sensing*.; 10(6):869. doi:10.3390/rs10060869

Thomson, J., Fan, Y., Stammerjohn, S., Stopa, J., Rogers, W. E., Girard-Ardhuin, F., et al. (2016), Emerging trends in the sea state of the Beaufort and Chukchi seas, *Ocean Modelling*, 105, 1–12. doi:10.1016/j.ocemod.2016.02.009

Thomas, L. N., Tandon, A., & Mahadevan, M. (2008). Submesoscale processes and dynamics. *Geophysical Monograph Series*, 177, 17–38. doi:10.1029/177GM04

Timmermans, M.-L. (2015). The impact of stored solar heat on Arctic sea ice growth. *Geophysical Research Letters*, 42, 6399–6406. doi:10.1002/2015GL064541

Timmermans, M.-L., Cole, S., & Toole, J. (2012). Horizontal density structure and restratification of the Arctic Ocean surface layer. *Journal of Physical Oceanography*, 42-4, 659–668. doi:10.1175/JPO-D-11-0125.1

Timmermans, M.-L., & Windsor, P. (2013). Scales of horizontal density structure in the Chukchi Sea surface layer. *Continental Shelf Research*, 52, 39–45. doi:10.1016/j.csr.2012.10.015

Toole, J. M., Timmermans, M.-L., Perovich, D. K., Krishfield, R. A., Proshutinsky, A., & Richter-Menge, J. A. (2010). Influences of the ocean surface mixed layer and thermohaline stratification on Arctic Sea ice in the central Canada Basin. *Journal of Geophysical Research*, 115, C10018. doi:10.1029/2009JC005660

von Appen W.-J., Wekerle, C., Hehemann, L., Schourup-Kristensen, V., Konrad, C., & Iversen, M. H. (2018). Observations of a submesoscale cyclonic filament in the marginal ice zone. *Geophysical Research Letters*, 45, 6141–6149. doi:10.1029/2018GL077897